Universidade de São Paulo
Instituto de Astronomia, Geofísica e Ciências Atmosféricas
Departamento de Astronomia

Maria Luísa Gomes Buzzo

Detailed Studies of Lenticular Galaxies in the Local Universe

São Paulo
2020

Maria Luísa Gomes Buzzo

Detailed Studies of Lenticular Galaxies in the Local Universe

Master dissertation presented to the Department of Astronomy of the Instituto de Astronomia, Geofísica e Ciências Atmosféricas of the Universidade de São Paulo as a partial requisit to obtain the title of Master of Science.

Corrected Version. The original can be found at IAG/USP.

Supervisor(a): Prof.(ª) Dr.(ª) Claudia Lucia Mendes de Oliveira

São Paulo

2020

Aos meus irmãos

Acknowledgements

Meus agradecimentos começam por uma das pessoas mais incríveis que eu tive a chance de conhecer e trabalhar nos últimos cinco anos; que me ensinou a maioria do que sei em Astronomia e a gostar e lidar com a ciência e a Academia, mesmo quando os momentos foram difíceis. À minha co-orientadora, Arianna Cortesi, o meu maior obrigado e admiração.

Ao Baldi, meu companheiro, melhor amigo e suporte por todos os últimos anos, muito obrigada por toda a ajuda e dedicação com a vida, com a física, com essa dissertação, com tudo. Você foi essencial para tudo o que lutei e conquistei. Muito obrigada por me permitir aprender e compartilhar tanto da vida com você.

Aos meus pais, Aderval e Elena, por todo o suporte, apoio e amor que me dedicaram sempre. Por entenderem minha ausência quando o trabalho se impôs, por sempre acreditarem em mim e por serem minha base todos os dias.

Às pessoas que mais amo nessa vida, minhas sobrinhas Natalia e Mariana, agradeço por fazerem minha vida mais feliz e divertida todos os dias.

Aos meus irmãos, Camila, Marco e Ana e aos irmãos que a vida me deu, Aureo e Ana Flávia, dedico essa dissertação. Vocês sempre foram e continuam sendo minha grande inspiração e força. Sou muito realizada e privilegiada de ter na minha própria família, meus melhores amigos e confidentes para tudo. Amo vocês.

Aos amigos do IAG que fizeram dessa jornada a melhor que poderia ser: Thayse, Natalia, Erik, Lilianne, Geeh, Stela e tantos mais. Obrigada por todos os rolês, cafés, cervejas, procrastinações, risadas e confidências. E que venha o doutorado!

Às irmãs que a física me deu: Bruna, Renata, Mariana, Barbra, Dimy e Morgana, obrigada por serem as mulheres incríveis e amigas maravilhosas que são. Obrigada pelos anos de dedicação e diversão e por sempre estarem presentes nos melhores e piores momentos

da vida. Vocês são uma inspiração todos os dias e eu não canso de admirar e me alegrar pelas suas conquistas. Eu amo vocês e essa amizade é para a vida toda.

À Maria Cristina Campiglia, por todo o apoio, torcida, ajuda e dedicação. Por ter me aceitado e acolhido com tanto amor na sua família, muito obrigada.

À minha orientadora Claudia, por sempre estar presente, ser uma inspiração e um exemplo de pessoa e cientista todos os dias. Obrigada pelos ensinamentos, ajudas com burocracias e conselhos para a vida. Sou muito feliz e realizada de ter sido sua orientanda pelos últimos 5 anos.

Ao meu co-orientador, Roderik Overzier, pela ajuda incessante no desenvolvimento desse mestrado e por todas as ideias e ajudas com o futuro doutorado. Pelas dicas, tanto relacionadas ao trabalho, quanto à Academia e à vida. Pela confiança e por todos os ensinamentos no último ano, muito obrigada!

Ao Prof. Jorge Meléndez, pela ajuda e confiança que teve em mim nos últimos anos. Te agradeço profundamente e mantenho Astrofísica Observacional como uma das melhores matérias que tive a oportunidade de fazer na minha carreira.

To Lodovico Coccato, Victor Debattista, Eric Emsellem, Duncan Forbes, Michael Merrifield, Steven Bamford, Marina Vika, Marco Grossi, Fabricio Ferrari, Gefferson Lucatelli, Eduardo Cypriano, Karín Menéndez-Delmestre, Raul Abramo, Carolina Queiroz, the whole S-PLUS collaboration and all other collaborators that were essential for the development of this dissertation. Thank you so much.

To my supervisor in Vienna and everyone in the group, Bodo Ziegler, Bianca Ciocan, Miguel Verdugo, Polichronis Paraderos, and all others, thank you for accepting me and for the help throughout the last months. My stay in Vienna was the best I could ask for and I am extremely thankful for the chance to know and work with such amazing people.

Ao IAG e à USP pelo apoio institucional, e à CAPES e FAPESP, pelo auxílio financeiro de número 2018/09165-6 e 2019/01639-1.

Aos contribuintes e ao Brasil por terem tornado possível a realização desse mestrado.

À presidenta Dilma Rousseff e ao presidente Luís Inácio Lula da Silva, pelo empenho em tornar o Brasil um país mais igualitário e melhor para todas as classes.

E, por fim, agradeço à Marielle Franco, Mestre Moa do Catendê e tantos outros que tiveram suas vidas sacrificadas na luta por direitos iguais e por um Brasil melhor. Continuaremos na luta!

"isso de querer ser exatamente aquilo que a gente é
ainda vai nos levar além."

– *Incenso fosse música*, Paulo Leminski.

Resumo

Galáxias S0 são supostamente uma fase de transição na vida de uma galáxia, na qual partilha propriedades tanto de galáxias elípticas como de galáxias espirais. Assim, a compreensão deste tipo de objeto pode trazer informações importantes sobre todo o campo de evolução de galáxias. As galáxias lenticulares representam quase metade da população de galáxias gigantes no universo próximo, no entanto, a sua história de formação, e se são uma classe de objetos única ou composta, continuam a ser questões em aberto na astronomia moderna.

Neste trabalho, estudamos esta classe de galáxias em três frentes usando diferentes conjuntos de dados: primeiro, olhamos para uma galáxia lenticular totalmente formada, NGC 3115, usando dados em variados comprimentos de onda em busca de recuperar a sua história de formação e evolução; em segundo lugar, olhamos para um evento que poderia gerar uma galáxia S0, a fusão massiva NGC 1487, usando dados em espectroscopia de campo integrado (IFS) do MUSE/VLT. Finalmente, estudamos a distribuição de galáxias S0 no universo local usando dados fotométricos do mapeamento S-PLUS. Reunindo estes três trabalhos, pretendemos proporcionar uma melhor compreensão das galáxias lenticulares no universo local e identificar quais são os progenitores e os cenários de formação mais prováveis em diferentes ambientes.

No esquema de classificação de Hubble, galáxias lenticulares são definidas como tendo um disco, sem braços espirais. No entanto, um estudo mais detalhado revela que estas apresentam várias subcomponentes, como um disco, um bojo, e em alguns casos também uma barra e lentes. A decomposição de uma galáxia nas suas componentes permite recuperar os gradientes de cor presentes no sistema, a sua história de formação estelar e, finalmente, a sua história de formação. Utilizamos GALFITM para realizar esta decom-

posição em variados comprimentos de onda simultaneamente da galáxia lenticular mais próxima da Via Láctea, NGC 3115, resultando na descrição de suas populações estelares em três componentes principais, incluindo um bojo, um disco fino e um disco espesso. Recuperamos diagramas cor-magnitude pixelizados e a distribuição espectral de energia das componentes. Os resultados mostram que a maioria da massa da galáxia se encontra na região do bojo e que esta é a componente mais azul, sugerindo tanto atividade de núcleos ativos de galáxias (AGN) como eventos recentes de formação estelar. Mostramos que esta galáxia possui uma barra e características semelhantes à espirais, provavelmente criadas durante uma interação recente. Finalmente, propomos um cenário para a formação de NGC 3115 com base numa fusão inicial rica em gás, seguida por uma sequência de acréscimos e feedback de AGN, responsável pela cessão da formação estelar na galáxia, até que um encontro recente reacendeu a formação estelar no bojo e gerou as características em espiral observadas.

É bem conhecido que galáxias S0 podem ser formadas por diferentes processos, e por isso aqui estudamos a eficácia de fusões massivas como um dos mecanismos de formação das galáxias S0. Usando dados em IFS do MUSE/VLT da galáxia em interação NGC 1487, estudamos as propriedades físicas e cinemáticas do sistema. Encontramos uma inversão no gradiente de metalicidade do sistema NGC 1487, explicada por processos de mistura de metais. O campo de velocidade revelou um padrão de rotação numa das subcomponentes de NGC 1487, mostrando que a galáxia pode estar em processo de recriação de um disco. Concluímos que se a evolução do sistema levar à formação de um disco, então este evento de fusão poderia evoluir passivamente para se tornar uma galáxia S0 em vários giga-anos.

Finalmente, para compreender a distribuição das galáxias lenticulares no universo local, e o papel dos ambientes na sua formação, determinamos redshifts fotométricos e tipos espectrais de galáxias no mapeamento S-PLUS. Identificamos os objetos melhor ajustados pelo espectro teórico de galáxias lenticulares e encontramos a sua distribuição em todo o universo local. Os resultados mostram que as S0s se encontram, na sua maioria, em regiões aglomeradas e estão dificilmente isoladas. Além disso, mostramos que entre as galáxias identificadas como lenticulares de acordo com o seu tipo espectral, as que apresentam baixas taxas de formação estelar também apresentam uma morfologia visual típica das galáxias lenticulares, enquanto as que apresentam altas taxas de formação estelar são provavelmente lenticulares com atividade nuclear ou galáxias espirais classificadas incorretamente.

Abstract

S0 galaxies are supposedly a transitional stage in the life of a galaxy, in which it shares properties of both elliptical and spiral galaxies. Thus, understanding this type of object can bring important information on the whole field of galaxy evolution. Lenticular galaxies account for almost half of the giant galaxy population in the nearby universe, yet their formation history and whether they are a unique or a composite class of objects remain an open question of modern astronomy.

In this work, we study this class of galaxies in three fronts using different datasets: firstly, we look at a fully formed lenticular galaxy, NGC 3115, using multi-wavelength data to recover its formation history and evolution; secondly, we look at an event that could generate an S0, the major merger NGC 1487, using MUSE/VLT integral field spectroscopy (IFS) data. Finally, we study the distribution of S0 galaxies in the local universe using photometric data from the S-PLUS survey. Putting together these three works, we aim at providing a better understanding of lenticular galaxies in the local universe and at identifying what are the progenitors and the most likely formation scenarios in different environments.

In the Hubble classification scheme, lenticular galaxies are defined to have a disk, without spiral arms. Yet a more detailed study reveals that lenticulars present several subcomponents, as a disk, a bulge, and in some cases also a bar and lenses. Decomposing a galaxy in its components allows recovering the colour gradients present in the system, its star formation history and, finally, its assembly history. We used GALFITM to perform a multi-wavelength structural decomposition of the closest lenticular galaxy to the Milky Way, NGC 3115, resulting in the description of its stellar populations into three main components, including a bulge, a thin disk and a thick disk. We recovered pixelized color-

magnitude diagrams and the spectral energy distribution of the components. The results show that the majority of the mass of the galaxy is in the bulge region and that this is the bluest component, suggesting both active galactic nuclei (AGN) activity and recent star formation events. We show that this galaxy holds a bar and central spiral-like features, probably created during a recent interaction. Finally, we propose a scenario for the formation of NGC 3115 based on an initial gas-rich merger, followed by a sequence of accretions and AGN feedback, responsible for quenching the galaxy, until a recent encounter reignited the star formation in the bulge and generated the observed spiral features.

It is well known that S0 galaxies can be formed by different processes, here we study the effectiveness of major mergers as one of the formation mechanisms of S0 galaxies. Using MUSE/VLT IFU data of the major merger NGC 1487, we study the physical and kinematical properties of the system. We find an inversion in the metallicity gradient of the system NGC1487, explained by metal mixing processes. The velocity field revealed a rotating pattern in one of the sub-components of NGC1487, showing that the galaxy may be in the process of recreating a disc. We conclude that if the evolution of the system would lead to the formation of a disc, then this merger event could evolve passively to become an S0 galaxy in several Gyr from now.

Finally, to understand the distribution of lenticular galaxies in the local universe, and the role of environments in their formation, we determined photometric redshifts and spectral types for galaxies in the S-PLUS survey. We identified the objects best-fitted by the lenticular galaxies' template and found their distribution across the local universe. The results show that S0s mostly lie in clustered regions and are hardly isolated. Moreover, we show that among galaxies identified as lenticular according to their spectral-type, the ones with low star formation rates also present a visual morphology typical of lenticular galaxies, while those with high star formation rates are probably lenticular galaxies with nuclear activity or incorrectly classified spiral galaxies.

List of Figures

List of Tables

Contents

Chapter 1

Introduction

Astronomy, in all of its different manifestations, has been important for most societies in human history. It has been used since ancient times, even before the concepts and methods of modern science were born, as a guide to understand the universe that surrounds us. With theories evolving with the necessity and culture, Astronomy has accompanied human kind during most of its evolution. Its impact in the way people see and portray life can be seen in several allusions to celestial events in the literary and artistic production throughout time (*Starry Night*, **Vincent Van Gogh**, *Macbeth, King Lear, Romeo and Juliet*, **William Shakespeare**, and many others).

Sometimes driven by fear of the unknown, other times with the curiosity and eagerness to understand our origins and where we are going to, the field of Astronomy became wide and diverse. However, despite its long history, one of the main pillars onto which western Astronomy is constructed is still in its infancy: the field of galaxy formation and evolution, the guiding principle of this dissertation.

Our knowledge of galaxies in the universe is vast and it evolves fast. In fact, galaxies were first introduced only a century ago, when they were classified as nebulae and believed to belong to the Milky Way. Only in 1925, Edwin Hubble using Henrietta Leavitt's measurements of variable objects, the Cepheids, realized that their distances were much larger than the scale of our own Galaxy. The subject was largely debated years before, in particular by Harlow Shapley and Heber Curtis, in an event later entitled The Great Debate (Curtis, 1921), in which each supported his own idea that these nebulae either belonged to the Galaxy or were beyond it, respectively. This question was only settled with Hubble's observations years later.

Since this debate, astronomers have found out that galaxies are very intriguing objects.

They are mostly composed of dark matter, gas, dust and billions of stars. When together, galaxies form the largest virialized structures in the universe: the galaxy clusters. When in smaller numbers, they can form groups or they can even be isolated. They can be interacting, they can have large or small sizes, be fast-rotating or pressure-supported, close or very far away, round or flat, have discs or not, and so on.

Another important contribution of Edwin Hubble, in 1936 (Hubble, 1936), was the Hubble tuning fork (Fig. 1.1), a classification scheme for galaxies in the universe. This scheme was largely revised over the last decades, with several additions and rearrangements. One example of a modern classification scheme, proposed by the Atlas 3D survey (Cappellari et al., 2011), using a kinematic perspective, is shown in Fig. 1.1, together with the original scheme from Hubble.

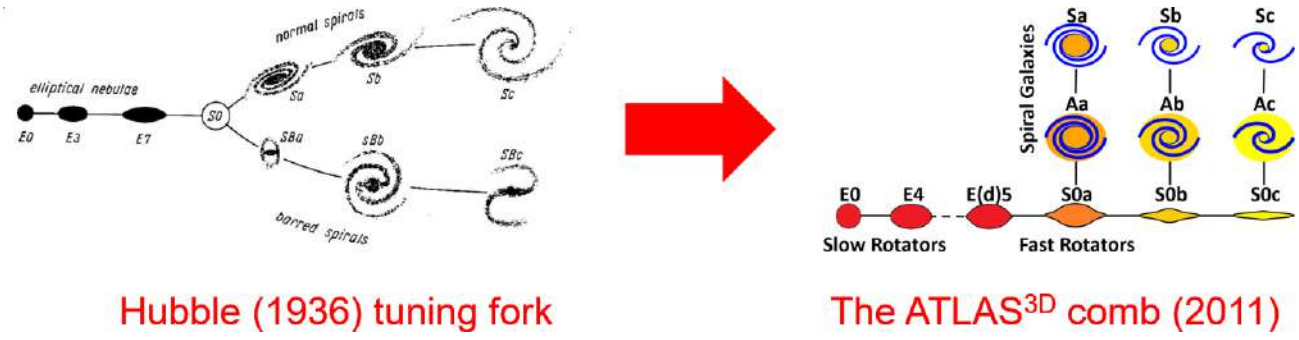

Figure 1.1: Hubble Tuning Fork (Hubble, 1936), left. The Atlas 3D classification scheme (Cappellari et al., 2011), right.

Yet another classification scheme for galaxies, proposed by Kormendy and Bender (1996), using a photometric perspective similar to Hubble (1936), is shown in Fig. 1.2

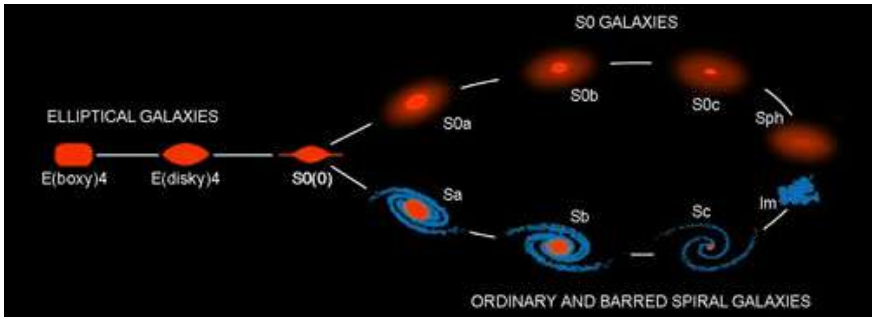

Figure 1.2: Parallel sequence galaxy classification including spheroidal (Sph) galaxies as bulgeless S0 galaxies together with irregular (Im) galaxies. Figure from Kormendy and Bender (1996)

In these classification schemes, galaxies span three main types. The spiral galaxies are characterized by very blue and young populations in their discs. They can be classified

according to the compactness of their spiral arms and the size of their central region. A second type of galaxies are the ellipticals: showing old and red stellar populations. They can be represented by a single ellipsoid with a variety of ellipticities. The last type of galaxies bridge the elliptical and the spiral galaxies, perhaps as a transitional phase in galaxies evolution: these are the lenticular or S0 galaxies and they are the main object of study of this thesis. Even though we learned a lot about this recent field of astronomy, there are still important questions about S0 galaxies that need to be answered. Particularly, are they indeed a transitional phase? What processes are able to form such objects? Regardless of the answers to these questions, it is clear that this class of galaxies holds important information about the whole field of galaxy formation and evolution, since they outnumber each of the other two types of galaxies in the Local Universe (van den Bergh, 2009).

Before going into the main topic of our work, it is worth mentioning that some types of galaxies were not taken into account in these early classification schemes. Those include irregular galaxies which have odd shapes, dwarf galaxies which have low surface brightness, and a special type of giant elliptical galaxy (cDs) that live in the centers of clusters. Some works propose that many irregular galaxies are, in fact, interacting systems (Gallagher and Hunter, 1984), which is a topic we will touch on when discussing major mergers as possible formation scenarios for S0 galaxies (Sec. 1.2.2).

1.1 An introduction to S0 galaxies

Lenticular galaxies, first introduced as a class of galaxies in 1936 (Hubble, 1936), have been studied ever since, in a range of environments, redshifts and masses; recently, it has been shown that they account for most of the galaxies in the local universe (Bernardi et al., 2010). The number of lenticular galaxies increases towards the center of clusters, opposite to the spiral galaxies. This is known as the "Morphology-Density Relation" (Dressler, 1980) and it is shown in Fig. 1.3. At the same time, studying high mass galaxies, van den Bergh (2009) has shown that the number density of all galaxies that are of types S0 or SB0 is 8% in the field, 13% in groups, 15% in typical clusters, and 28% in the Virgo cluster', The number of lenticular galaxies varies also with redshift, i.e. S0s are more common at lower redshifts, while the number of spiral and star-forming galaxies increases with increasing

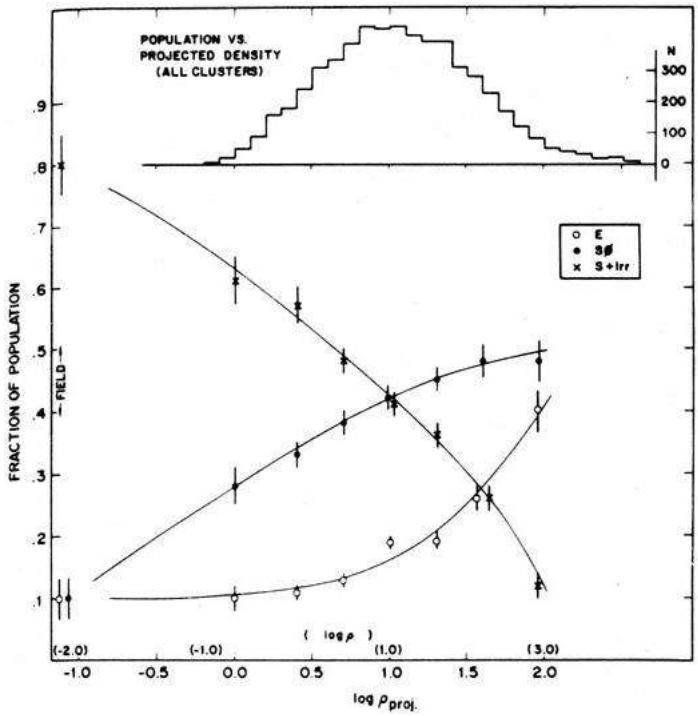

Figure 1.3: Morphology-Density relation proposed by Dressler (1980). This relation shows that late-type galaxies are more common in low-density environments (groups and the field), while early-type galaxies (ellipticals and S0s) prefer high-density environments (clusters). The upper histogram shows the number distribution of galaxies.

redshit (Dressler et al., 1997; Wilman et al., 2009; Barro et al., 2017).

Lenticular galaxies are a puzzle because they present features that can be related both to late- (spiral) and early-type (elliptical) galaxies. They have a disc, like spiral galaxies, but those discs have already quenched their star formation and do not present spiral arms. They may also show, in their centers, prominent bulges similar to those found in elliptical galaxies. Since these objects can be related to both main types of galaxies, a natural question arises: where did they come from and what evolutionary path will they follow?

Studies have shown that lenticular galaxies can be formed in different ways, depending on the environment they live in and the internal processes taking place within them. It is natural to assume that different formation scenarios would leave different imprints on the galaxy spectrum. With this in mind, one goal of this work is to find the distribution of S0 galaxies in the local universe and to investigate a possible correlation between their environments and spectral types, revealing what formation processes are more likely in different environments. But first, let us take a step back and understand what are the known possible ways to form lenticular galaxies in the universe.

1.2 S0 galaxies formation scenarios

A recent work of Fraser-McKelvie et al. (2018) has proposed that low mass S0s are quenched spiral galaxies, while high mass S0s result from minor mergers (Bekki, 1998; Bournaud et al., 2005), or major mergers (Eliche-Moral et al., 2018; Querejeta et al., 2015; Tapia et al., 2017; Borlaff et al., 2014). However, major mergers can only create S0 galaxies under some very specific initial conditions, such as similar angular momentum, velocity dispersions and so on. These specifities are expected because numerical simulations in the 1990s showed that major mergers are so catastrophic that they could hardly result in a system with an ordered disc, such as those of local S0s. Moreover, the remnants are expected to exhibit significant traces of their past merger origin for several billion years after the merger (Tapia et al., 2017), instead of the relaxed appearances that most present-day S0s have. Nevertheless, recent simulations (Eliche-Moral et al., 2018; Querejeta et al., 2015; Tapia et al., 2017; Borlaff et al., 2014) show examples of S0 galaxies that are the result of major merger events.

Coccato et al. (2019) showed that the kinematics at, $1R_e$, of lenticular galaxies living in low and high density environments are different at a 1.5σ confidence level, suggesting that both mass and environment may play a role in shaping the fate of the progenitor(s) of lenticular galaxies. This result needs, nevertheless, to be confirmed at a higher level of significance.

Different formation scenarios should lead to different kinematics and stellar populations, therefore to different imprints in the galaxy spectrum, as discussed above. The mechanisms that form field lenticular galaxies would not be the same as those creating their high-density counterparts, since mergers are more probable in low density environments, where the velocity of the stars in a galaxy is of the same order of magnitude as the velocity of the galaxy in the group environment. Tidal interactions are also typical of galaxy groups, while hot gas and deep gravitational wells are necessary to harass or strip a galaxy falling into a cluster of galaxies.

In the following subsections we discuss in more detail the previously cited formation scenarios of lenticular galaxies and we identify the main observable differences that we will use to perform our analysis.

1.2.1 Quenched spirals

Lenticular galaxies are very common in clusters, as shown previously in the morphology-density relation (Fig. 1.3). Their presence can be explained as the transformation of spiral galaxies falling into clusters and losing their star-forming gas through ram-pressure stripping (Gunn and Gott, 1972; Durret et al., 2011; Schindler and Diaferio, 2008). The loss of the gas from the spiral arms is given by many factors, which appear in combination: (1) tidal stripping, i.e. repeated galaxy-galaxy encounters; (2) ram pressure stripping and gas evaporation, according to which galaxies passing near the center of a cluster are swept by the denser intracluster gas, quenching star formation; (3) harassment, characterized by high-speed encounters between galaxies capable of extracting gas from their discs.

If lenticular galaxies are spiral galaxies whose gas has been stripped during the infall into a cluster, we might expect that the disc stellar population is older than the one of the spheroid (Johnston et al., 2014), either because the gas truncation leads to an outside-in quenching of the star formation (Finn et al., 2018), or because the bulge stellar population could be rejuvenated by a last star-forming episode (Bekki and Couch, 2011), caused by the collapse of the stripped material into the central region.

1.2.2 Galaxy-Galaxy Interactions

Mergers can be classified as major or minor. If major, they usually involve two galaxies of similar masses (mass ratios of 1:3 or smaller); if minor (mass ratios of 1:3 or 1:4), they can include galaxies of different masses. A complex sequence of minor mergers or accretion is the most probable way to form S0 galaxies in the field and groups, since they can explain the quenching of star formation of the disc and the enhancement of the bulge size.

Tapia et al. (2017) show that major mergers generate S0-like galaxies that deviate from the Tully-Fisher Relation for S0s at $z \sim 0.8$, because the merger is capable of creating large discrepancies in the kinematics of the systems, while minor mergers generate S0-like remnants that only contribute to increasing the dispersion in this relation. The work also suggests that the S0 remnants, when they are the result of major mergers, should come from progenitors with high gas content and be over-luminous at their early stages as S0 galaxies, hosting young stellar populations at their centres (e.g. Christlein and Zabludoff (2004); Hammer et al. (2009)) that are the result of merger-induced starbursts. This supports a

merger-origin scenario (Poggianti et al., 2001; Kaviraj et al., 2007) because cluster-related environmental processes can hardly explain the existence of these starbursts.

In this work, we study a major-merger event at an early stage to identify some of the characteristics proposed to form S0-like galaxies. We study the impact of the merger in the progenitor galaxies: the metal content and metal mixing, stellar populations, gas flows, supernovae and AGN mechanical feedbacks and star formation rates to help us understand if and how these events create S0 galaxies. This work is shown in Chapter 3 for the interacting galaxy NGC 1487.

1.2.3 Violent Disc-Instability

Lenticular galaxies could also be relics of high-redshift galaxies (Saha and Cortesi, 2018). If so, they would be the result of violent disc instability and fragmentation. This phenomenon is capable of explaining S0-like galaxies that are found in the field environment, where environmental effects and interactions are generally absent. If the lenticular galaxies are formed this way, they will never pass through a spiral phase, as primordial galaxies, and their bulge and disc would have the same stellar population, as they are formed by the same material. The process of morphological evolution of lenticular galaxies formed this way is shown in Fig. 1.4, for four simulated galaxies with different Toomre Q parameter, i.e. different measures of the stability of the discs, taking into account different velocity dispersions of the stars, as shown in Eq. 1.1 (Toomre, 1964).

$$Q(R) = \frac{\sigma_r(R)\kappa(R)}{3.36G\sum(R)}, \tag{1.1}$$

where κ is the epyciclic frequency and $\sum$ is the surface density.

1.2.4 Disc accretion around high-redshift compact ellipticals

Another mechanism to form S0s consists of a massive compact elliptical galaxy acquiring a disc after merging with a gas-rich satellite, transforming itself into an S0 (Diaz et al., 2018). In this model, the compact elliptical evolves to become the bulge of the S0, and the satellite feeds the build-up of a young disc. Some remarkable features of this formation history are: (1) the main progenitor is not a spiral in contrast with other S0 formation scenarios in the literature, but a "red nugget", i.e. relics of the first massive galaxies that

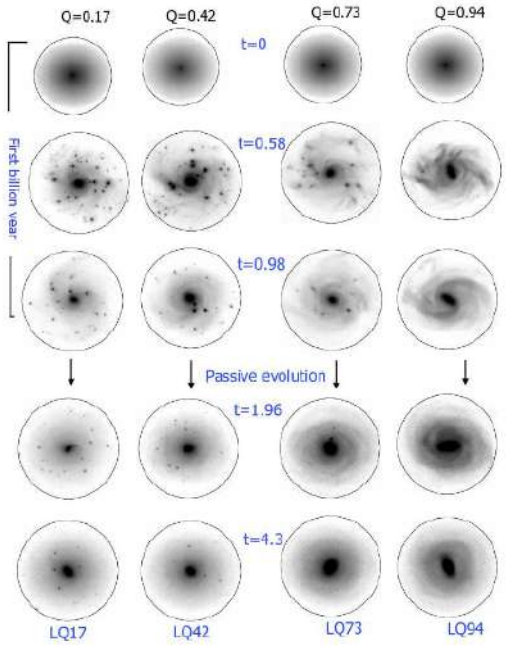

Figure 1.4: Morphological evolution of four simulated galaxies with different initial velocity dispersions of the stars (Saha and Cortesi, 2018).

formed after the Big Bang, (2) the bulge of the remnant galaxy is older than the disc, (3) This transformation is likely to occur in the field. Fig. 1.5 shows a snapshot of the simulation of the formation process, highlighting the accretion path of the satellite into the elliptical. In this figure, the left panels represent the stellar components, while the right panels show the behaviour of the gas component in the interaction (Diaz et al., 2018).

1.3 Summary of objectives

The ultimate goal of this master dissertation is to provide a guide to understand lenticular galaxies in the nearby universe. This will be pursued on three fronts:

- (Chapter 2) The formation history of an S0 galaxy in the field: NGC 3115. We use multiwavelength data to understand the origin and evolution of the closest lenticular galaxy to the Milky Way. We compare its physical properties with the ones from the literature to uncover the most probable formation scenario for this galaxy.

- (Chapter 3) Major mergers as possible scenarios to create S0 galaxies: the interacting system NGC 1487. We show how a merger event impacts the metal distribution of the galaxies, the stellar populations, star-formation rates, gas flows and kinematics of

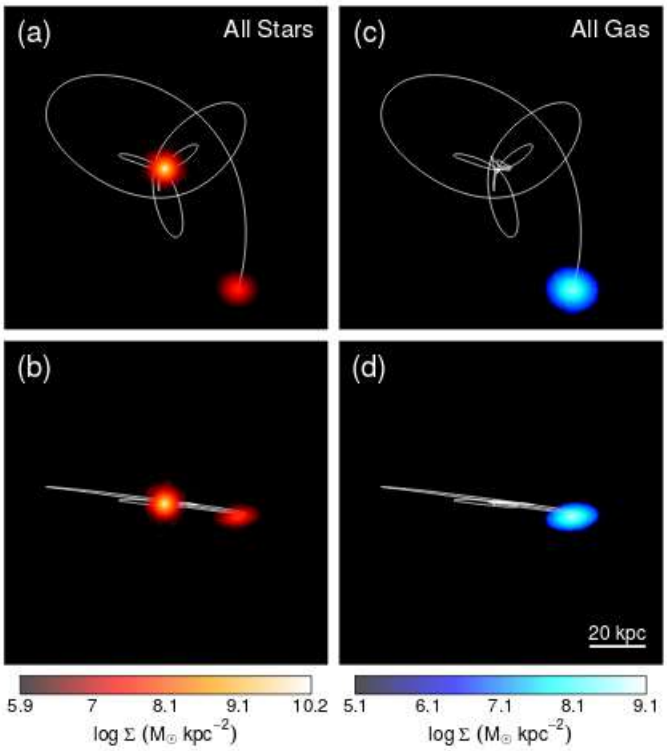

Figure 1.5: Left column, stellar component of the merger seen face and edge-on, respectively. *Right column*, gas component of the accretion face and edge-on. (Diaz et al., 2018)

the system and, finally, we discuss if events like this can generate lenticular galaxies.

- (Chapter 4) The distribution of S0 galaxies in the local universe. We derive photometric redshifts for the S-PLUS survey to recover the properties and distribution of galaxies in the local universe and select a large, statistical sample of S0 galaxies.

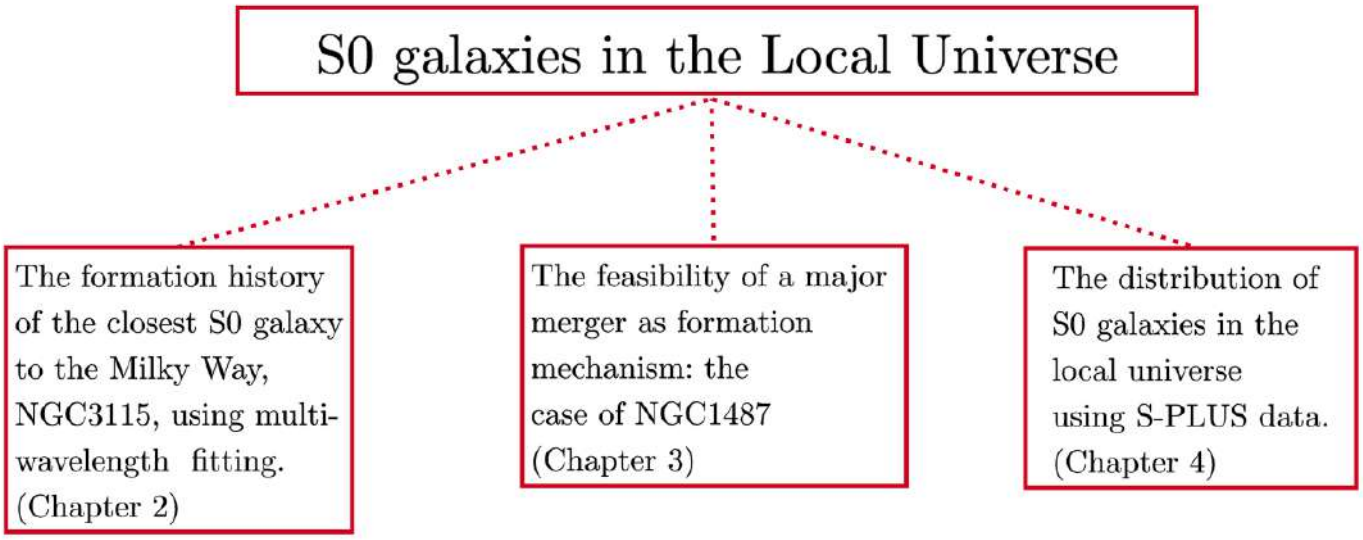

Figure 1.6: Dissertation Objectives.

Chapter 2

The formation history of the S0 galaxy NGC 3115

As discussed in Chapter 1, S0 galaxies were first introduced in 1936 by Edwin Hubble. However, this classification was done based on the apparent visual morphology, which is highly dependent on the inclination of the galaxy. For example, face-on S0s are commonly misclassified as elliptical galaxies.

One way to solve this issue is to use the bulge-to-disc (B/D) flux ratio to minimize the confusion caused by the unknown galaxy inclination on its morphological classification. In fact, ellipticals hardly have discs, resulting in high bulge-to-disc ratios. Spiral galaxies and S0 galaxies have similar B/D ratios, forming a parallel sequence in the Kormendy and Bender (2012) classification. In this latter case, the presence of gas, spiral arms and clumps of star formations allows to differentiate S0s from spiral galaxies.

The colour and components of a galaxy can also be used as proxies for morphology to differentiate between early- and late-type galaxies. The most commom colour cut is defined as $u - r = 2.22$, regardless of magnitude (e.g. Strateva et al. (2001)), where the bluest galaxies lie below this cut and the reddest ones are above. The $NUV - r$ versus r colour-magnitude diagram has also been found to be an effective way for classifying galaxies as either early- or late-type (Wyder et al., 2007). The location of a galaxy in this colour-space also reflects the degree of star-formation activity (Park and Choi, 2005), and correlates well with the age of the stellar population. In this diagnostic diagram, passively evolving galaxies form the red sequence, star forming galaxies lie in the blue cloud, and S0 galaxies may be found in the green valley (Gonçalves et al., 2012; Salvato et al., 2018).

Therefore, it is important to have both the information on the identification of each sub-component of a galaxy and the colour of that component, to be able to fully understand the morphology and formation history of these galaxies. Several methods to perform bulge-disc

decomposition have been developed in the past years. These codes model the galaxies as the sum of their components, using parametric and non-parametric models to reproduce the observations until the residuals (the difference between the image and the best fit model) are as close to zero as possible. The better the structural properties of the galaxies are defined, the better the model will be.

2.0.1 Structural Properties of Galaxies

Galaxies are commonly described by a radial luminosity profile that gives the light distribution inside the galaxy, from its center to its outskirts. A general formula for the light profile of a galaxy was proposed by Sérsic (1963):

$$I(r) = I_e \left\{ -b_n \left[\left(\frac{r}{R_e} \right)^{\frac{1}{n}} - 1 \right] \right\}, \tag{2.1}$$

where n is the Sérsic index, responsible for controlling the shape of the profile. I(r) is the surface brightness at a given radius, R_e the effective radius (the radius containing half of the model light), I_e is the intensity at the effective radius, and b_n is a function of the Sérsic index such that $\Gamma(2n) = 2\gamma(2n, b_n)$, where Γ and γ stand for the complete and incomplete gamma functions, respectively (Ciotti, 1991) (see Fig. 2.1). An approximation of b_n in terms of n is $b_n = 2n - 1/3$.

Elliptical galaxies are generally well described by a single sérsic profile, i.e. they can be modeled with one single component and, usually, with a sérsic index ≥ 2.5 (Simard et al., 2011).

Their spiral counterparts, on the other hand, generally have two or more components, and, therefore, cannot be fitted by single Sérsic profiles. In fact, they will be the superposition of different profiles, with different Sérsic indices for each of their components. Usually spiral galaxies can be fitted by an exponential disc and a bulge, although recent studies also take into account possible bars. Exponential discs are analytically equal to a Sérsic profile with $n = 1$, $R_e = 1.67R_d$, where R_d is the disc-scale length and $\Sigma_e = \Sigma_d/b_n(1)$ (Kormendy (1977)), while bars can be described by Sérsic profiles with $n < 1$ (gaussian function for $n = 1/2$).

Bulges can be "classical", $n = 4$, or pseudo-bulges, $n \leq 2.5$. Classical bulges are not star-forming and they were probably created in the first moments of the galaxy formation.

Pseudo-bulges generally contain younger populations than classical bulges, they are likely formed by secular evolution (Carollo (1999); Andredakis and Sanders (1994)) and are rotationally supported. Their profiles can vary from $n \sim 1$ to $n \sim 2.5$ (Simard et al., 2011), so the usual approach is not fixing n, when attempting to find the best model using an initial input inside these boundaries. Fig. 2.1 shows the Sérsic profiles derived by Peng et al. (2002), using different Sérsic indices and, therefore, these may be appropriate for different components of galaxies.

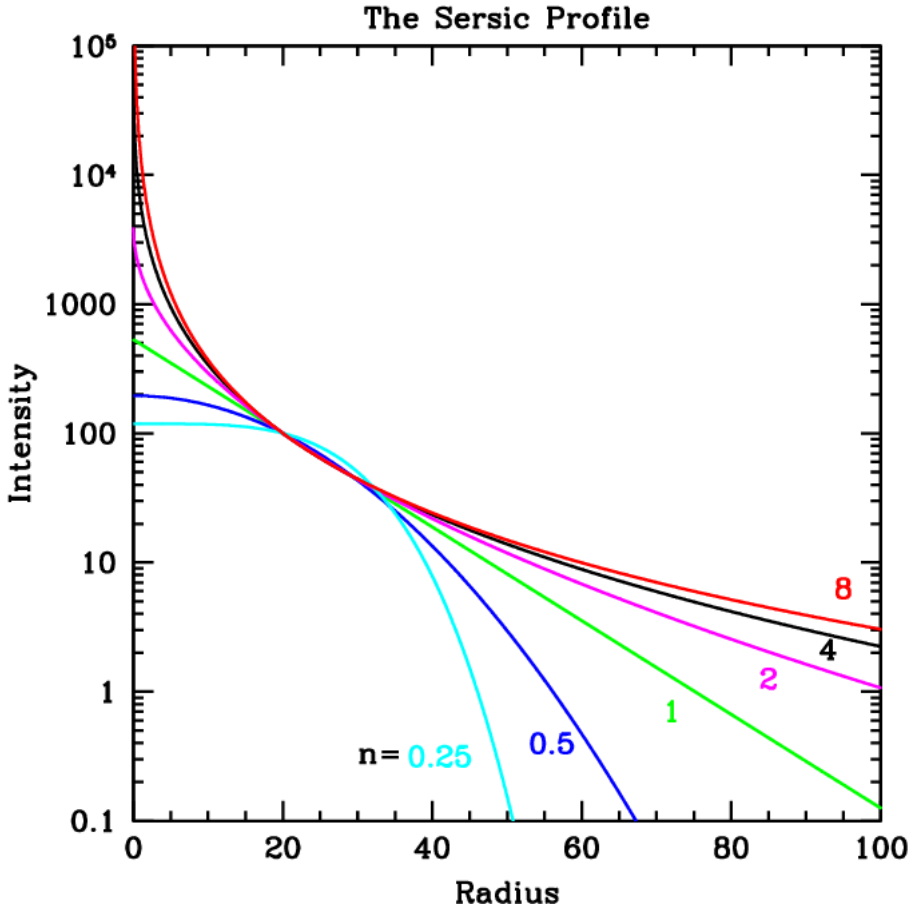

Figure 2.1: The radial light distribution for different Sérsic profiles. Image from Peng et al. (2002).

Other structural measurements are the galaxy ellipticity (b/a), position angle (PA) and diskyness/ boxyness (C0).

2.0.2 Wavelength dependence of structural parameters

Previous studies have shown a strong relation between measured sizes of galaxies and wavelength. For example, the effective radii of galaxies of all morphologies were found to be smaller in redder bands (McDonald et al. (2011); Kelvin et al. (2012); Vulcani et al. (2014)).

The variation of the Sérsic index with wavelength is also noticeable: n measured in the near infrared is generally significantly larger than in the optical (Kelvin et al. (2012); Vika et al. (2015)). These variations in the structural properties of galaxies directly imply that the colour of a galaxy must change with distance from its centre. This can be measured as a colour gradient across the main axis of a galaxy and it can be used as a non-parametric way of characterising the stellar populations within a galaxy. These colour gradients will be further studied in Section 2.4.1.

Although the radius and Sérsic index display great differences when comparing different wavelengths, parameters such as position angle, inclination and ellipticity, in turn, have small variations across wavebands, when fitting more than one component.

Since galaxies can change much when varying wavelengths, studying objects in different parts of their spectra should give important information on the different populations present across the galaxy. More than that, decomposing the galaxy in its main components at different wavelengths should lead us to a greater understanding of the gradients present in the galaxies. Comparing the stellar population of the disc and the spheroid we can understand where the last star-formation episode occurred, from where the quenching started, and we can recover the formation history of the galaxy. A method to decompose galaxies in multi-wavelength bands has thus emerged as a great way to perform these types of studies.

2.0.3 Galaxy properties and their spectral signatures

A galaxy spectrum allows the determination of many physical properties of galaxies, such as how far away it is, its chemical composition, age, formation history and so on. While the shape of the spectrum of passive, star-forming, AGN and other types of galaxies are very different and unique in their own ways, some general properties of spectra are universal.

As previously discussed in the introduction of this dissertation, galaxies are mostly composed of dark matter, gas, dust and billions of stars. Apart from the dark matter component, all the other are classified as "baryonic", i.e. composed of baryons. These baryons leave different imprints on a galaxy spectrum, that can be measured by the spectral energy distribution (SED), the measurement of the galaxy flux as a function of wavelength.

In general, young stars are responsible for the hydrogen ionizing flux ($\lambda < 912$ Å) and

the UV emission in galaxies. This short-wavelength emission is strongly affected by dust, as UV is absorbed and then re-emitted in the mid- and far-infrared. The older stars, in turn, are more relevant in the near-infrared (NIR). The molecular gas emission is detected at radio wavelengths, while the ionized gas is mainly detected by emission lines in the optical region (Schmidt, 1963; Khachikian and Weedman, 1974).

For star-forming galaxies, for example, the radiation of young stars is absorbed by the dust present in the galaxy. Star-formation is, thus, detectable in several parts of the spectrum: by the radio emission of molecular gas, by the UV emission of young stars, by the optical emission of the ionized gas and by the dust emission in the far-infrared. Fig. 2.2 shows the comparison of a spiral galaxy spectrum with a non-star forming one, which clearly shows the main spectral differences of these types of galaxies.

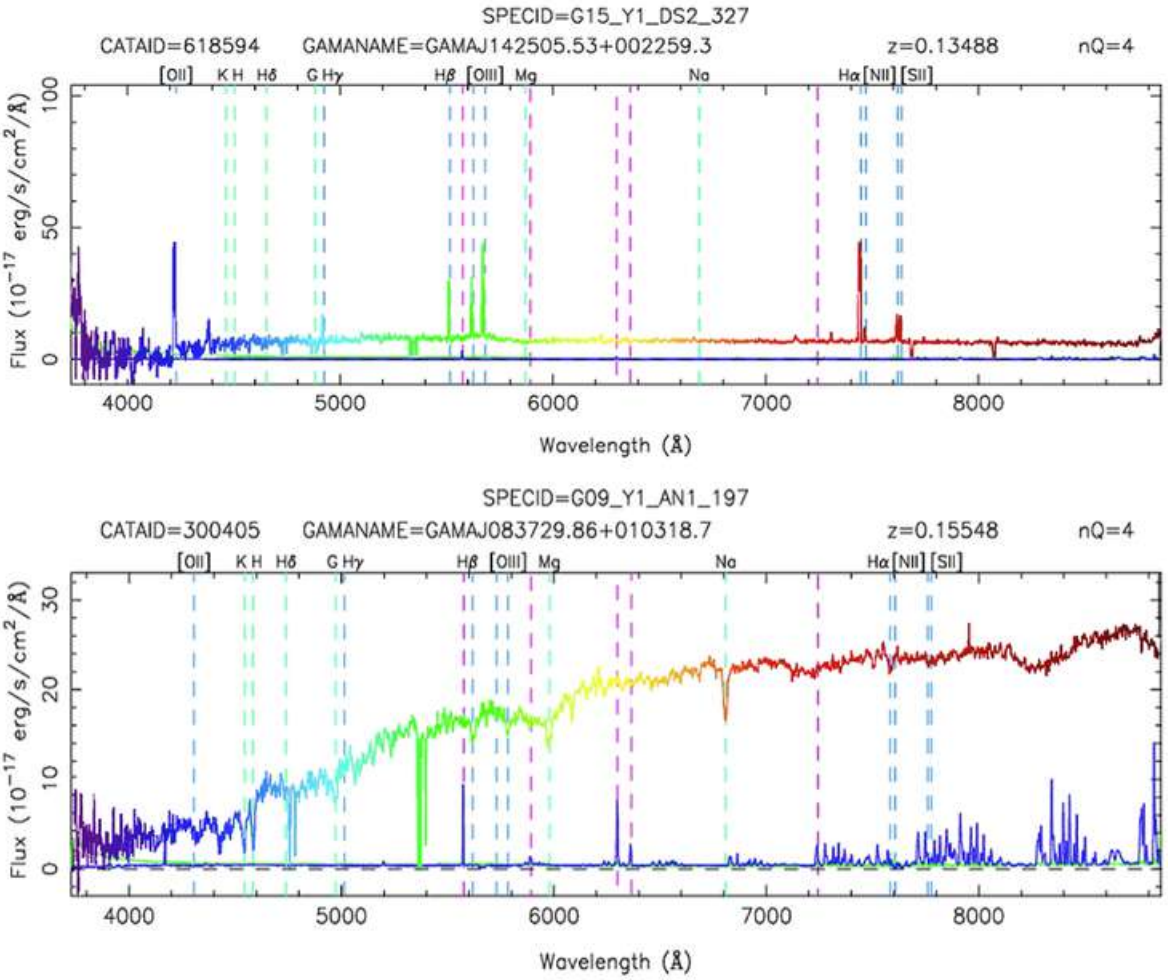

Figure 2.2: Top panel shows the spectrum of a spiral galaxy and bottom shows the spectral of a non-star forming galaxy. The blue parts of the spectra show the ionizing and UV regions, green stands for the optical, while red is the near and far-infrared. Image created by the American Astronomical Society (Bauer and the American Astronomical Society (2015))

Active Galactic Nuclei (AGN) are galaxies that host super-massive black holes that are accreting material onto their centers and therefore have yet another type of emission. AGNs emit radiation across a wide wavelength range and produce strong emission lines in the optical. These lines can be narrow or broad, depending on the velocity dispersion of the ionized material that is detected.

As galaxies can be so different and these discrepancies reflect in distinctive parts of their spectra, it is important to have information over a wide wavelength range to be able to fully understand each object. This is one of the great advantages of using multi-wavelength data to find the SED of a galaxy and its components. In the upcoming sections, we will utilize information from ultraviolet to infrared wavelengths, contrary to spectroscopic studies, which are normally focused on a single part of the spectrum.

2.0.4 Multi-wavelength fit

Historically images in various ranges of wavelength were fitted independently and then convolved to the same pixel scale and point spread function (PSF) for realistic comparison. This can lead to problems, fully discussed in Vika et al. (2014), such as unreliable colours. MegaMorph, described thoroughly in Häußler et al. (2013) and Vika et al. (2013), was developed to perform multi-wavelength fitting of images. A multi-wavelength fit brings lots of advantages; one of the most important being the capability of fitting bands with low signal-to-noise ratio (SNR), like those in the UV and infrared. MegaMorph is a code based on the GALFIT (Peng et al., 2002) and GALAPAGOS (Barden et al., 2012) routines, and it has two sub-divisions: GALFITM and GALAPAGOS-2 (see Section 2.2.1).

2.0.5 Objectives

A cluster lenticular galaxy may have been pre-processed in a group or in the field environment, which makes it harder to isolate the mechanism responsible for its formation. On the contrary, an isolated lenticular galaxy, such as NGC 3115, provides an ideal laboratory for studying the formation of this intriguing class of galaxies.

The main goal of this project is to understand how the closest lenticular galaxy to the Milky Way, NGC 3115, was formed. NGC 3115 is isolated and has been studied by a large number of authors (Guérou et al. (2016); Poci et al. (2019a); Usher et al. (2019); Poci et al. (2019b); Cortesi et al. 2013b).

We use GALFITM to perform multi-band fitting of imaging data from ultraviolet (GALEX, Bianchi and GALEX Team, 1999) to infrared (WISE, Wright et al., 2010) to decompose the light of the galaxy into its main components, and to study in detail each component and its properties, over a large wavelength range (see Section 2.2.1).

2.1 Data

For this work, we used multi-wavelength images of NGC 3115 to recover the age and metallicity of its components. There is a large amount of data available for NGC 3115, i.e spectra, integral field spectroscopy (IFS) and photometry. However, although the IFS and spectroscopic data provide precise measurements of stellar ages and metallicities, they only cover a narrow range of wavelength and generally a small field-of-view, covering only the central luminous part of the galaxy. On the other hand, full SED data, from ultraviolet to infrared, allow us to recover the galaxy stellar populations out to very large radii, as discussed in Sec. 2.0.3.

Moreover, multi-band surveys and fitting techniques have seen an increasing use in the last years since they offer the best combination between large number statistics and precision of the recovered parameters (Szalay, 1999, SDSS), (Mendes de Oliveira et al., 2019, S-PLUS), (Cenarro et al., 2019, J-PLUS), (Dupke et al., 2019, J-PAS)).

2.1.1 Obtaining the data

To perform the fitting, we used 11 images of the galaxy NGC 3115 obtained with different telescopes, in an attempt to cover a wide wavelength range. We collect data from the Galaxy Evolution Explorer (Bianchi and GALEX Team, 1999, GALEX), SUBARU Suprime Cam (Miyazaki et al., 2002), Dark Energy Cam (Valdes et al., 2014, DECAM), 2MASS (Skrutskie et al., 2006) and Wide-Field Infrared Survey Explorer (Wright et al., 2010, WISE). In Table 2.1 we show the details of each image used in this work.

The images were all set to have the same pixel scale, world coordinate system (WCS), dimension and center as the 2MASS H band image (1”/px). This was done using Montage (Jacob et al., 2010), a tool for gathering fits images into custom mosaics.

Below we give details of the treatments made on the data, in order to prepare them for the analysis.

Table 2.1 - Data used in this work

Instrument	Band	Wavelength (Å)
GALEX	Far-UV (FUV)	1520
GALEX	Near-UV (FUV)	2270
SUBARU Suprime Cam	g	4770
SUBARU Suprime Cam	r	6800
SUBARU Suprime Cam	i	7630
DECAM	z	9260
2MASS	J	12500
2MASS	H	16500
2MASS	Ks	21700
WISE	3.4	34000
WISE	4.6	46000

2.1.2 Point Spread Function (PSF)

We create a synthetic PSF of each image using the Moffat distribution (Moffat, 1969). The PSF can be created using 2D Gaussian functions, but the Gaussian profile is much sharper than the images taken from stars on CCDs. The Moffat distribution, in other hand, uses an exponential profile, defined by:

$$f(r) = a\left[1 + \left(\frac{r}{\alpha}\right)^2\right]^{-\beta}, \tag{2.2}$$

where α is a normalization parameter, and together with β defines the shape of the Moffat function. The radial parameter α is related to the full width at half maximum (FWHM) by:

$$FWHM = 2\alpha\sqrt{2^{1/\beta} - 1}. \tag{2.3}$$

Using this definition, for a fixed FWHM, as β increases, the Moffat function becomes sharper, and as limiting case when $\beta \to$ inf, the Moffat function becomes the regular Gaussian function.

To create the PSFs of our images, we recover the FWHM and β parameter using the IMEXAMINE function in IRAF.

2.1.3 Sky

To measure the sky background, we used a recently developed routine from Hernandez et al. (in prep). This code is based on an estimation of the background using the median value of small regions of the images, with little contamination from stars, followed by a sigma clipping, until convergence to the best value is reached. The best sky value for each wavelength band is defined in the configuration file of GALFITM to be considered by the routine when creating the best fit model.

2.1.4 Zero points

The zero points of these images were retrieved from each respective telescope, using AB magnitudes. However, for the Subaru Prime Cam these values were not available. To retrieve such information, we used the detailed study of the globular cluster system around NGC 3115, which made use of the same images analysed in this work, presented in the paper of Jennings et al. (2014). Comparing the magnitudes of each object in the paper and our own determinations of the instrumental magnitudes, we have estimated the offset, which corresponds to the zero points of these images. They are 30.470, 30.5 mag, 31.5 for g, r and i, respectively. We also compared these zero-points with the zero-points of DECAM for the sloan g, r and i bands, finding a good agreement. An example of this estimation is shown in Fig. 2.3 for the g band image.

2.2 Methods

2.2.1 GALFITM

The original GALFIT (Peng et al. (2002)) code fits a variety of 2D analytic functions to galaxy images. Multiple components may be added, for example a bulge, disc and bar. The purpose of GALFIT is to minimise the χ^2 between a galaxy image and the PSF-convolved model by modifying the free parameters of the chosen functions.

GALFITM, in turn, can accept a set of images at different wavelengths. To these images, GALFITM fits a single, wavelength-dependent, model. As for GALFIT, this model includes one or more components, each with a number of parameters, i.e. center (x,y), magnitude (mag), effective radius (R_e), Sérsic index (n), axis ratio (b/a) and position

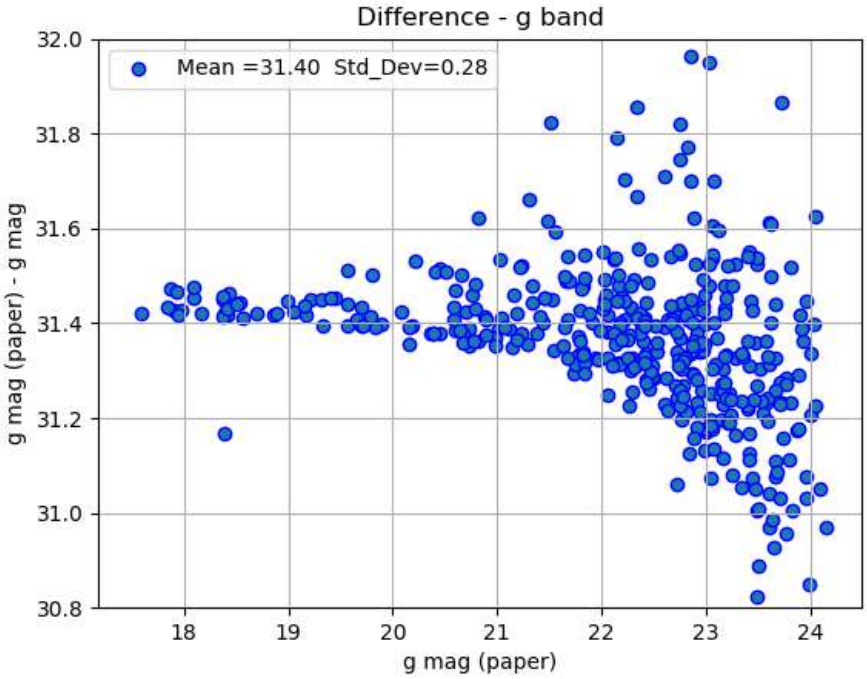

Figure 2.3: Zero-point value found for the Subaru g data of NGC 3115 using magnitudes of globular clusters around NGC 3115 in Jennings et al. (2014). The mean zero-point and standard deviation are 31.4 and 0.28 mag, respectively.

angle (PA). To extend these components to a simultaneous multi-wavelength fit, their free parameters are replaced with wavelength-dependent functions. These functions, denoted $\tilde{p}_i$, are written as linear combinations of Chebyshev polynomials (Abramowitz and Stegun, 1965), $T_j(z)$:

$$\tilde{p}_i(\lambda; \{q_{i,j}\}) = \sum_{j=0}^{m_i} q_{i,j} T_j[z(\lambda)]. \tag{2.4}$$

Here, $\{q_{i,j}\}$ are the coefficients of such combination, while m_i sets the higher degree of the polynomial in the expansion and may be chosen by the user, giving more or less freedom to the color-dependence of each of the model parameters. The function $z(\lambda)$ maps the wavelength interval to the range $[-1, +1]$, which is the domain of the polynomials. Whereas standard GALFIT fits the p_i, in GALFITM the parameters of the fit are the set $\{q_{i,j}\}$, which in turn define the function $\tilde{p}_i$. The Chebyshev polynomial $T_j(z)$ is of order j, i.e. $T_2(z)$ is a quadratic function of z. This function does not need to be considered as representative of the actual physical dependence of the model parameter with wavelengths; this does not, however, prevent one from considering it as a smooth approximation in some cases (Häußler et al. (2013)).

For an example of how this works, if the user would select $m_0 = 2$ to model an exponential disc component, the variation of the parameter with λ would be linear. The parameters may be set to a constant and not vary with wavelength at all ($m_0 = 0$) or the fit can return the parameter that best fit all λ ($m_0 = 1$). This approach is particularly used when fitting multi-components. The colour of a galaxy can be the result of the superposition of several components (red bulge + blue disc). When we separate the components, it is reasonable to assume that there is not a strong colour gradient, and we can assume that the fitted parameters do not vary with λ. Also, the parameters may vary with wavelength as quadratic, or higher-order functions. The higher the order of variation of the coefficients, the more flexible the function becomes, such that when the number of free coefficients is the same as the number of input images, that parameter can vary independently between bands. If, on one hand, this would seem to extract all information of the chosen λ range, on the other hand, it may return unphysical parameters, since the S/N between bands varies drastically and the power of GALFITM consists exactly in fitting all bands simultaneously to increase the S/N of faint images. Concluding, one should compromise between the degrees of freedom of the fit and the physical reliability of each fitted component.

In Appendix B we show a comparison of GALFIT and GALFITM performed simultaneously and individually, respectvely in our datasets, where the discuss the advantages of using GALFITM.

2.2.2 Degrees of Freedom and Initial Conditions

The degrees of freedom (hereafter DoF) of GALFITM are the ones which dictate how each parameter will vary within wavelengths.

Therefore, to maximize the fit performance, we need to find the best combination of degrees of freedom that each parameter can vary with.

To do so, we created a set of 32 thousand models using different combinations of degrees of freedom for the parameters and number of fitted components (from Single Sérsic, to bulge-disc decomposition, to bulge-disc-disc decomposition). We used the Bayesian Information Criteria (BIC) and the Akaike Information Criteria (AIC) to recover the best model, which consists of three components (a bulge, a thick disc and a thin disc).

The process of creation and analysis of these 32 thousand models is described in Ap-

pendix (A). This analysis allowed us to understand the morphology of the galaxy and mean value of each parameter.

After knowing the morphology and average value of each parameter, we started the process of fitting again. This process aimed to start our fit with reliable initial conditions, to prevent the code to fall on a local minimum, instead of the global one.

Using at first only the three SUBARU images (the deepest and with highest SNR images), we used as inputs the mean parameters recovered in the previous analysis and for the magnitudes, we got the values from the Nasa Extragalactic Database (NED). This fitting started again with a single Sérsic model, then a bulge-disc model, and finally a bulge-disc-disc model.

Once we were happy with our model in the three deep images of SUBARU, we expanded the model to the 11 bands, leaving the parameters to vary with 1 DoF (same value in all bands), except for the magnitude and disc-scale length, that could vary with 9 and 2 degrees of freedom, respectively, for all components.

Keeping in mind that one should compromise between the degrees of freedom of the fit and the physical reliability of each fitted component, we decided to use a more conservative approach and constraint the majority of the degrees of freedom.

The parameters found for this best model, as well as the allowed degrees of freedom for each parameters are summarized in the Table 2.2, in the results section (2.3)

A summary of the steps taken to create the model that best describes NGC 3115 in all 11 bands is shown in Fig. 2.4

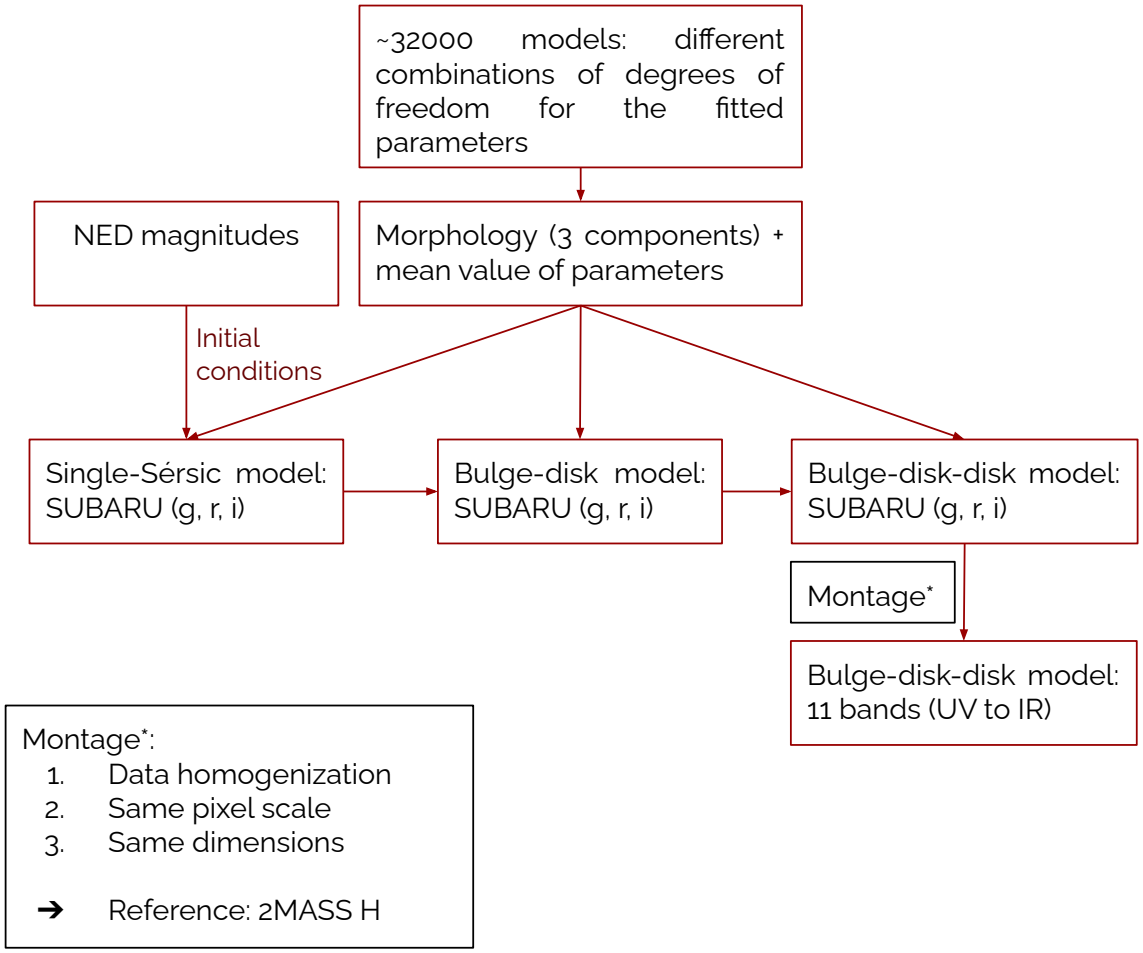

Figure 2.4: Steps taken for the creation of the best fit model of NGC 3115 with GALFITM, using three components (one bulge and two discs) in 11 bands, from GALEX to WISE.

2.3 *Results from* GALFITM

2.3.1 *Best Model: Bulge, Thick disc and Thin disc (BDD) decomposition*

As explained in the previous section, to find the best model, we passed from a single Sérsic (SS) model, to a bulge-disc decomposition (BD), to finally a bulge-disc-disc decomposition (BDD), which provided the smallest residuals, while maintaining the physical reliability of the model.

The evolution of the residuals from the simplest model with one components to the one with three components is shown in Fig. 2.5 for the r band.

The DoF of each parameter, as well as the best found value for them in each band is shown in Table 2.2.

The model with 11 bands and 3 components is shown in Fig. 2.6. This is the best

Table 2.2 - Results from best fit model of NGC 3115. The table shows the parameters that define the best fit of each component of the galaxy: bulge, thick disc and thin disc. The degrees of freedom of each parameter are shown in the third line of the table and describe how each parameter can vary with wavelength. See section 2.2.2

	Bulge					Thick disc					Thin disc				
	mag	n	Re	b/a	PA	mag	n	Rs	b/a	PA	mag	n	Rs	b/a	PA
DoF	9	1	1	1	1	9	0	2	1	1	9	0	2	1	1
FUV	15.07 ± 1.49	3.50 ± 0.01	21.68 ± 0.02	0.44 ± 0.01	44.19 ± 0.01	14.55 ± 0.15	1	61.17 ± 0.10	0.45 ± 0.01	43.42 ± 0.02	13.18 ± 0.11	1	23.13 ± 0.02	0.22 ± 0.01	44.83 ± 0.02
NUV	14.73 ± 0.72	3.50 ± 0.01	21.68 ± 0.02	0.44 ± 0.01	44.19 ± 0.01	14.25 ± 0.07	1	61.60 ± 0.12	0.45 ± 0.01	43.42 ± 0.02	14.45 ± 0.06	1	23.50 ± 0.02	0.22 ± 0.01	44.83 ± 0.02
g	12.33 ± 0.02	3.50 ± 0.01	21.68 ± 0.02	0.44 ± 0.01	44.19 ± 0.01	10.56 ± 0.02	1	63.05 ± 0.09	0.45 ± 0.01	43.42 ± 0.02	11.47 ± 0.01	1	24.74 ± 0.02	0.22 ± 0.01	44.83 ± 0.02
r	11.38 ± 0.02	3.50 ± 0.01	21.68 ± 0.02	0.44 ± 0.01	44.19 ± 0.01	9.61 ± 0.01	1	64.22 ± 0.08	0.45 ± 0.01	43.42 ± 0.02	10.36 ± 0.01	1	25.75 ± 0.02	0.22 ± 0.01	44.83 ± 0.02
i	11.30 ± 0.03	3.50 ± 0.01	21.68 ± 0.02	0.44 ± 0.01	44.19 ± 0.01	9.56 ± 0.01	1	64.70 ± 0.08	0.45 ± 0.01	43.42 ± 0.02	10.30 ± 0.02	1	26.16 ± 0.02	0.22 ± 0.01	44.83 ± 0.02
z	11.35 ± 0.02	3.50 ± 0.01	21.68 ± 0.02	0.44 ± 0.01	44.19 ± 0.01	9.30 ± 0.04	1	65.64 ± 0.08	0.45 ± 0.01	43.42 ± 0.02	9.97 ± 0.02	1	26.96 ± 0.02	0.22 ± 0.01	44.83 ± 0.02
J	10.74 ± 0.14	3.50 ± 0.01	21.68 ± 0.02	0.44 ± 0.01	44.19 ± 0.01	7.45 ± 0.01	1	67.51 ± 0.06	0.45 ± 0.01	43.42 ± 0.02	7.56 ± 0.01	1	28.57 ± 0.02	0.22 ± 0.01	44.83 ± 0.02
H	8.14 ± 0.01	3.50 ± 0.01	21.68 ± 0.02	0.44 ± 0.01	44.19 ± 0.01	8.62 ± 0.01	1	69.82 ± 0.05	0.45 ± 0.01	43.42 ± 0.02	9.37 ± 0.02	1	30.55 ± 0.02	0.22 ± 0.01	44.83 ± 0.02
Ks	8.23 ± 0.02	3.50 ± 0.01	21.68 ± 0.02	0.44 ± 0.01	44.19 ± 0.01	8.82 ± 0.01	1	72.83 ± 0.04	0.45 ± 0.01	43.42 ± 0.02	9.93 ± 0.03	1	33.12 ± 0.02	0.22 ± 0.01	44.83 ± 0.02
3.4	8.33 ± 0.02	3.50 ± 0.01	21.68 ± 0.02	0.44 ± 0.01	44.19 ± 0.01	8.73 ± 0.01	1	79.93 ± 0.04	0.45 ± 0.01	43.42 ± 0.02	9.82 ± 0.01	1	39.21 ± 0.03	0.22 ± 0.01	44.83 ± 0.02
4.6	9.06 ± 0.03	3.50 ± 0.01	21.68 ± 0.02	0.44 ± 0.01	44.19 ± 0.01	9.39 ± 0.01	1	86.86 ± 0.08	0.45 ± 0.01	43.42 ± 0.02	10.22 ± 0.01	1	45.16 ± 0.04	0.22 ± 0.01	44.83 ± 0.02

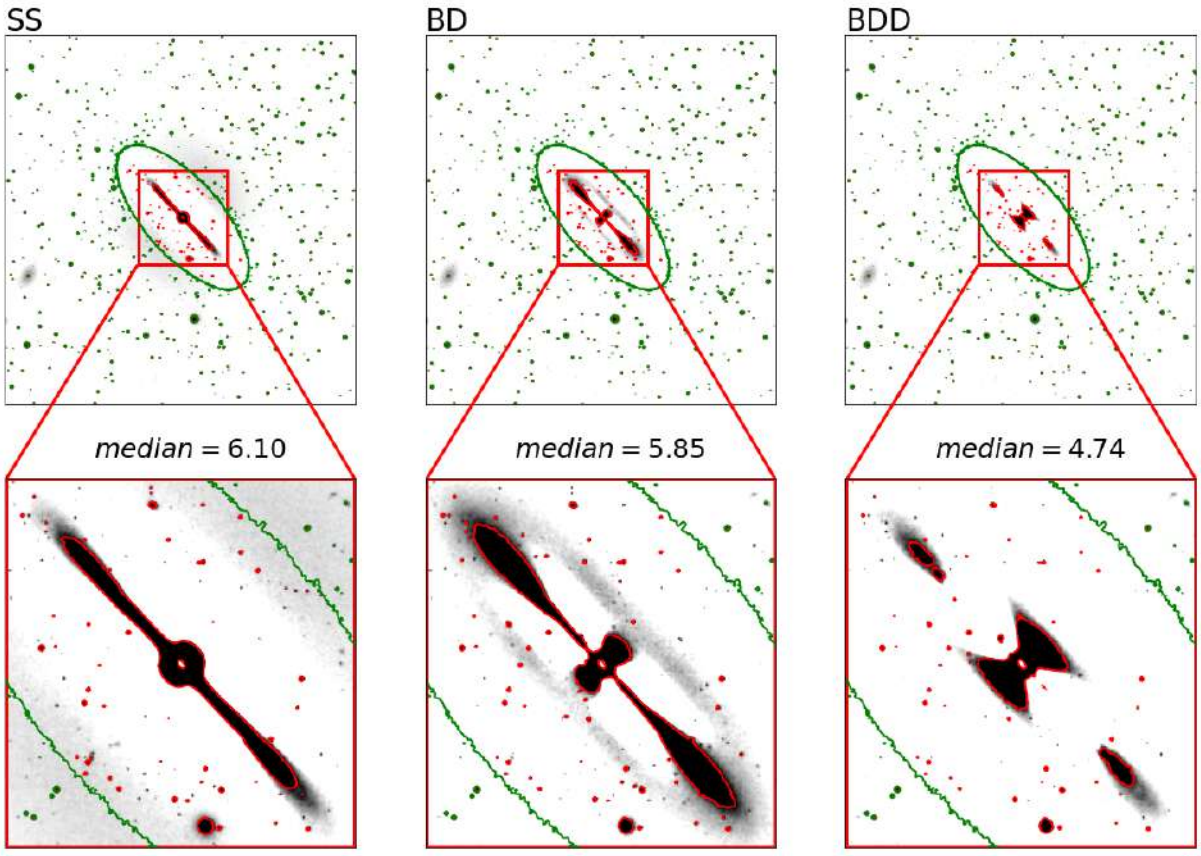

Figure 2.5: Evolution of the residuals (model - image) of the fit when using only one component: SS, two components (BD) and three components (BDD), from left to right. The top line shows the full image, while the bottom line shows the zoomed in rectangles highlighted on the full images. The green contours show the outermost isophote of the galaxy. The red contours highlight the position of the thin disc and subsequent fit of this thin disc in the final panel. The median of the residuals of each fit is shown between the zoomed out and zoomed in images.

model for NGC 3115 and the one that will be used to derive the SED of this galaxy and its components. Fig. 2.6 also shows each component that together form the total model, containing a bulge and two discs (BDD).

This model of NGC 3115 is a good representation of the galaxy. From Fig. 2.5 alone, we can already see how the bulge-disc decomposition and afterwards, the addition of the second disc substantially improved the fit. This in seen in the panels of Fig. 2.5 where we see the outer residuals diminishing with the addition of the disc, and then both outer and inner residuals practically vanishing with the inclusion of another disc. We provide the median of these residuals to give a quantification of the improvement that the addition of components brings. When we extrapolate this model to the one with 11 bands, seen in Fig. 2.6, we see that the model is capable of adjusting to the bands, providing a great representation of the galaxy, which is observable from the very low residuals in all bands.

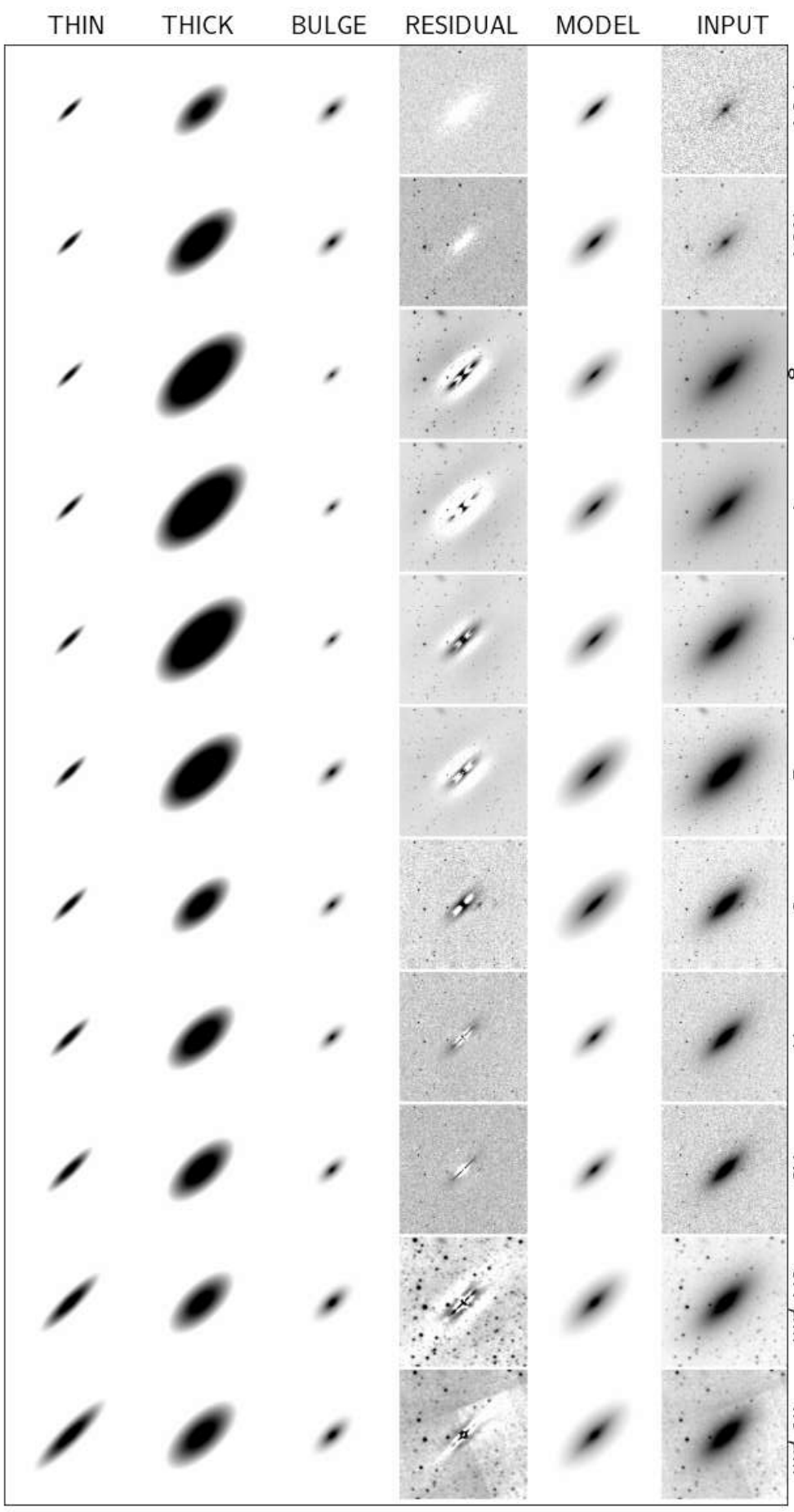

Figure 2.6: Model with a bulge, thick and thin disc for NGC 3115 created using GALFITM. Columns correspond to the input, model, residual, bulge, thick disc and thin disc models, respectively. The lines represent each wavelength band.

One can think that this model is not real for all bands, since we are simply extlapolating the best model found for the optical bands to all wavelengths, but this is not true. Actually, this is where the power of GALFITM relies. Assuming that the structural parameters that define each component, such as Sérsic index, position angle and axis ratio, do not vary substantially among bands, when we provide reliable initial conditions for these parameters (recovered from the model in the optical bands), these components will nicely adjust for bands where, without these conditions, it would have been really hard -if not impossible- to fit this well. Parameters that do change significantly with wavelength, such as magnitude and radius, are allowed to vary with a defined degree of freedom to be able to adjust to the differences between bands, providing an overall great fit of the galaxy in all bands studied.

From this model, we retrieved the variation of the disc scale-length of the thick and thin discs. For the bulge model, as explained before, the Sérsic index and effective radius were fixed at $n = 3.5$ and $R_e = 21.685$ pixels. The variation of the radius is shown in Fig. 2.7.

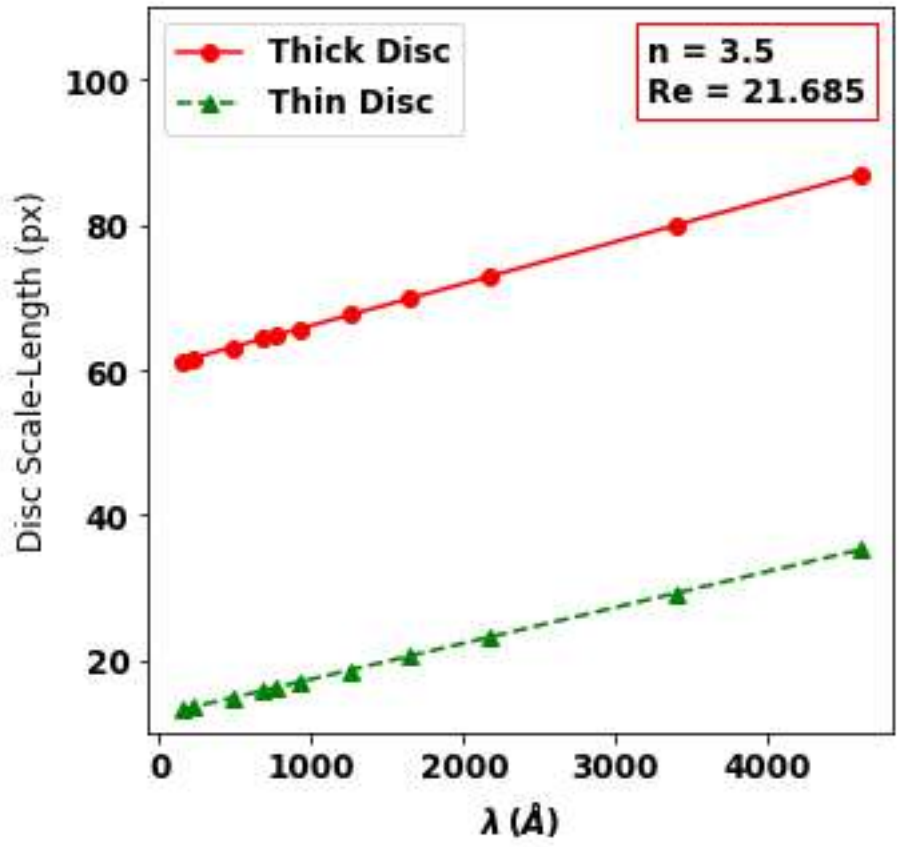

Figure 2.7: Radius variation of the thick and thin discs in the BDD model, with Sérsic index of the bulge fixed at 3.5 and effective radius fixed at 21.685.

As expected, the disc-scale length varies linearly across wavelengths, since we allowed the DoF of these parameters to vary with $m_0 = 2$ and this variation is very small, as expected when analysing the components separately.

In Fig. 2.8 we show the 1D profile of NGC 3115, showing where each component dominates the galaxy in three wavelength regimes: UV (NUV), optical (r) and IR (3.4 μm), and showing, therefore, the accuracy of our model in representing the galaxy in all wavelength-regimes.

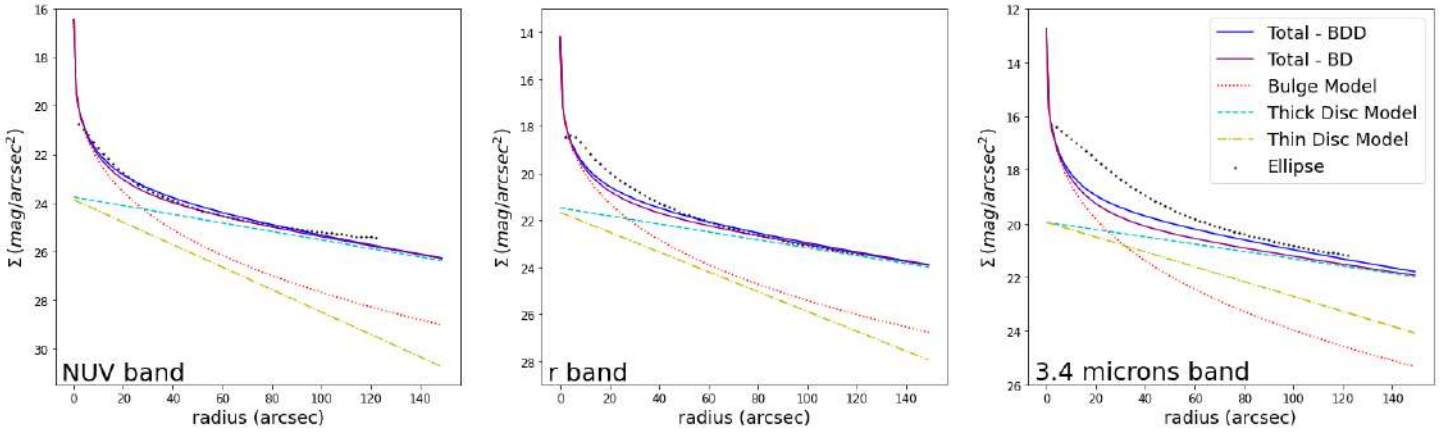

Figure 2.8: Surface density profiles of NGC 3115 and its components for three wavelength regimes: ultraviolet (NUV), optical (r) and infrared (3.4 μ m). Dotted red, cyan and yellow lines lines represent the extrapolation of the bulge (Sérsic), thick disc (exponential disc), and thin disc (exponential disc) fit performed with GALFITM to the stellar surface brightness data. The surface brightness profile as recovered with ellipse fitting (black dotted line) and with GALFITM models with two (BD) and three (BDD) components (blue and magenta lines, respectively) overlap until the faint outskirts in NUV, from 60 arcsec in the optical and from 80 arcsec in the infrared.

2.4 Analysis

2.4.1 Colours

To understand the stellar population of the galaxy' components, we used newly developed pixelized color-magnitude diagrams. This type of diagram was previously studied in Cook et al. (2019); Lee et al. (2018, 2017); Conroy and van Dokkum (2016) and present a new way to understand the stellar populations of galaxies using the magnitudes and colors of each pixel of the models at the different wavelengths. For this work, we have studied the pixelized color-magnitude diagram using the NUV-r colour. To create the images presented in Fig. 2.9 we have calculated the color (NUV-r) of each pixel present in the model images. To color the points, we use the fraction of light of each pixel that belongs to the

bulge component, the thick disc and the thin disc. These fractions of light were retrieved dividing each component by the total model created for the galaxy, therefore:

$$\frac{\text{bulge}}{\text{total}}\ (B/T) = \text{fraction of light of pixels that belong to the bulge.}$$

$$\frac{\text{thin disc}}{\text{total}}\ (d/T) = \text{fraction of light of pixels that belong to the thin disc.}$$

$$\frac{\text{thick disc}}{\text{total}}\ (D/T) = \text{fraction of light of pixels that belong to the thick disc.}$$

The points were constrained to be plotted only if the fraction of light belonging to the respective component was greater than 0.2 for each panel presented in Fig. 2.9.

Using these results and the models created with GALFITM, we have:

$$B/T = 0.12,\ D/T = 0.59 \text{ and } d/T = 0.29$$

To analyse the colour gradients in the galaxy, we have derived the colours using different wavelength regimes and looking at their distribution across the galaxy, as shown in Fig. 2.10 in 2D and in Fig. 2.11 in 1D.

With Figs. 2.9,2.10 and 2.11 we can see that this galaxy has a positive age gradient, when analysing the NUV-r colour, i.e. has a bulge bluer than the outskirts of the galaxy. We can see that, according to the definition of Salvato et al. (2018), all the components are mainly in the green valley, as it is expected for most lenticular galaxies. Moreover, Nogueira-Cavalcante et al. (2018) showed that barred galaxies, as NGC 3115, have the slowest transition time-scales through the green valley. The $NUV - r$ color of the bulge could be attributed to a young stellar population, the presence of AGN (Wong et al., 2011) activity or the emission of white dwarf stars (Lisker et al., 2008). Interestingly this galaxy present extended strong emission in the Spitzer 8 and 24 micron bands, covering especially the central part of the galaxy. Again, the presence of the mid-infrared emission in passive early-type galaxies (ETGs) might be of stellar origin, coming from the dusty envelopes around evolved asymptotic giant branch (AGB) stars (Clemens et al., 2011).

These results are important since they reinforce the effect of including ultraviolet data in the analysis. By looking at Figs. 2.10 and 2.11, we can see that, in the optical range, we

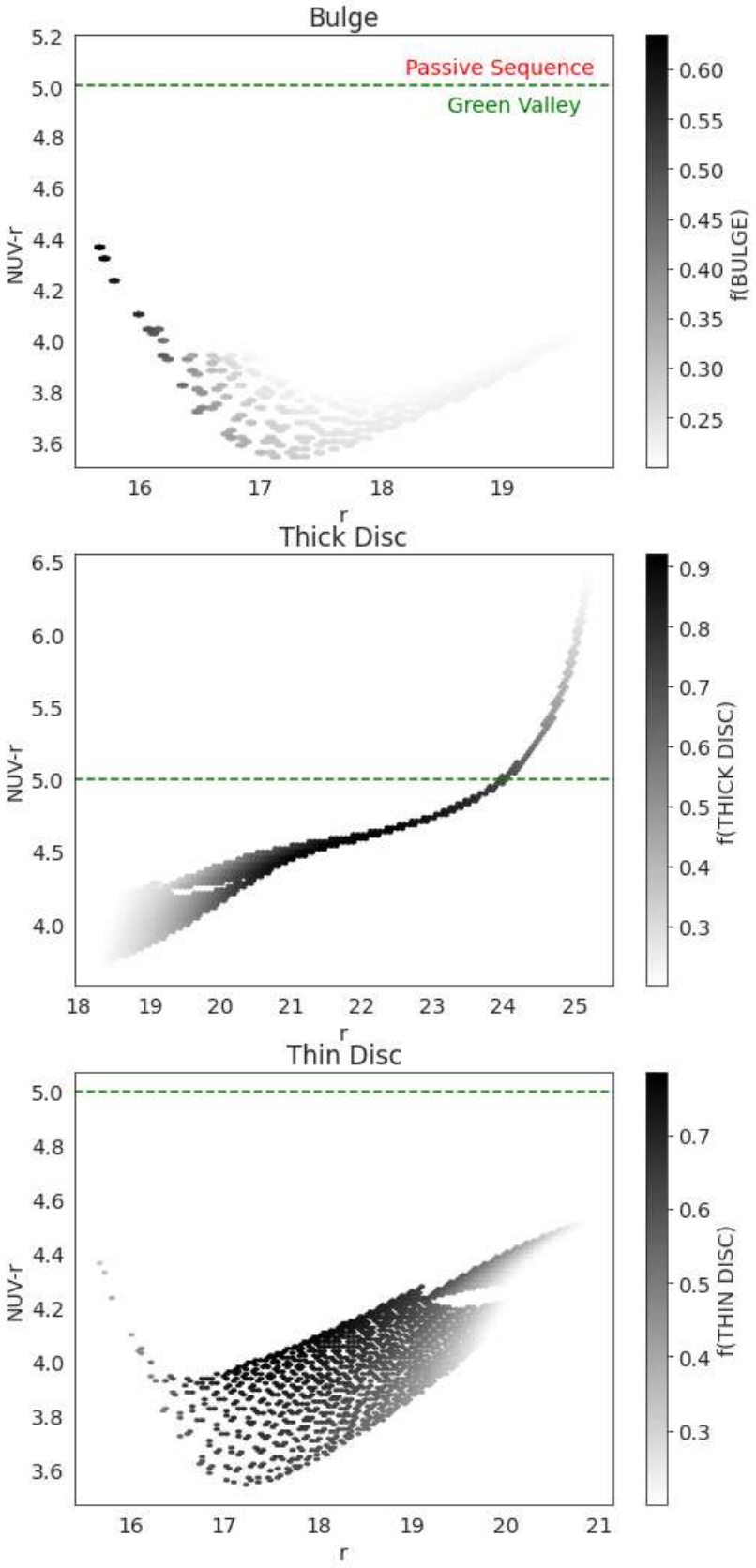

Figure 2.9: Pixelized Color Magnitude Diagrams color coded with the probability to belong to the bulge, thick disc and thin disc, respectively. Purple and red contours show the 2 and 3 σ confidence regions. The green dashed line defines the separation between green valley and passive sequence defined in Salim (2014).

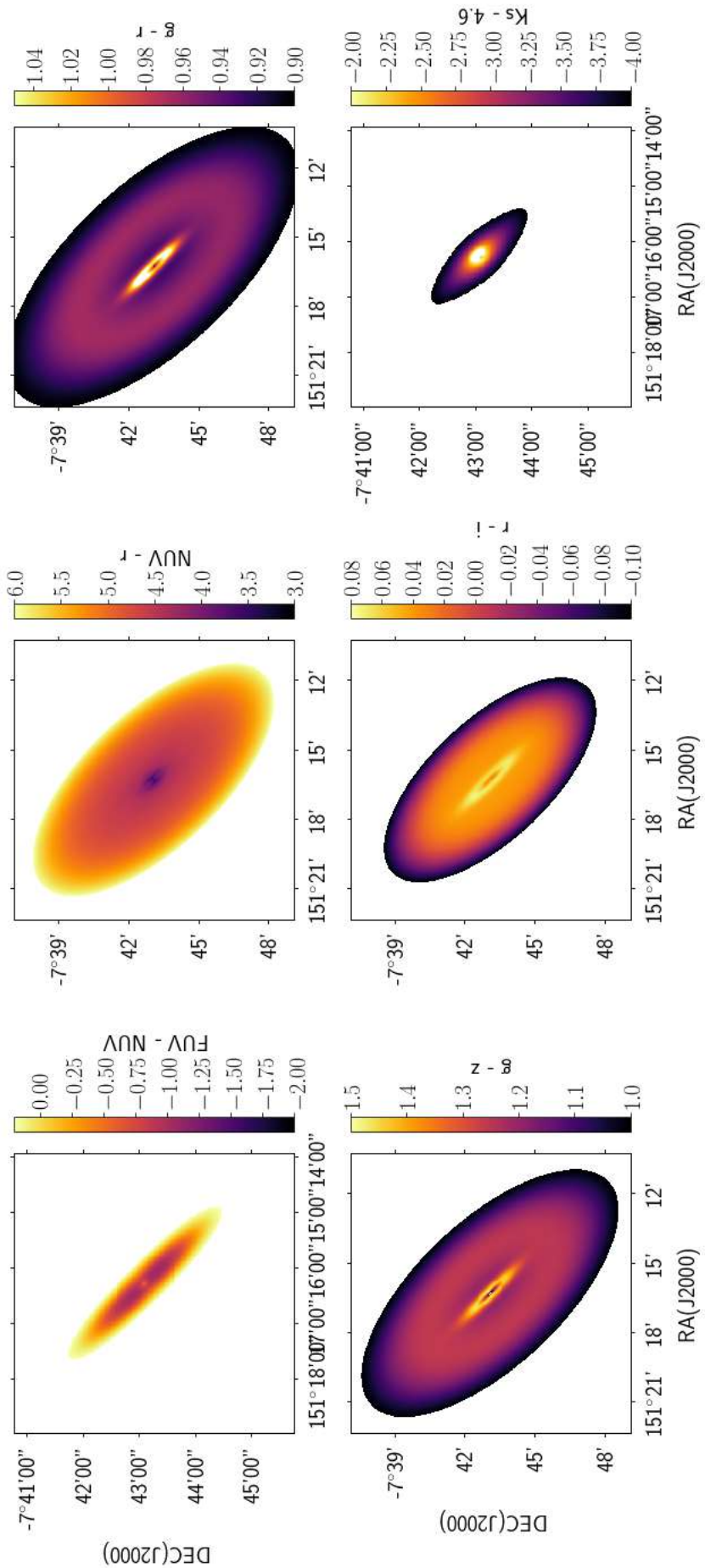

Figure 2.10: Gradient of the colors across NGC 3115. The bluest colors show the youngest populations, whereas the high values highlight older populations. According to Salvato et al. (2018), the color $NUV - r = 5$ separates the red sequence from the green valley galaxies.

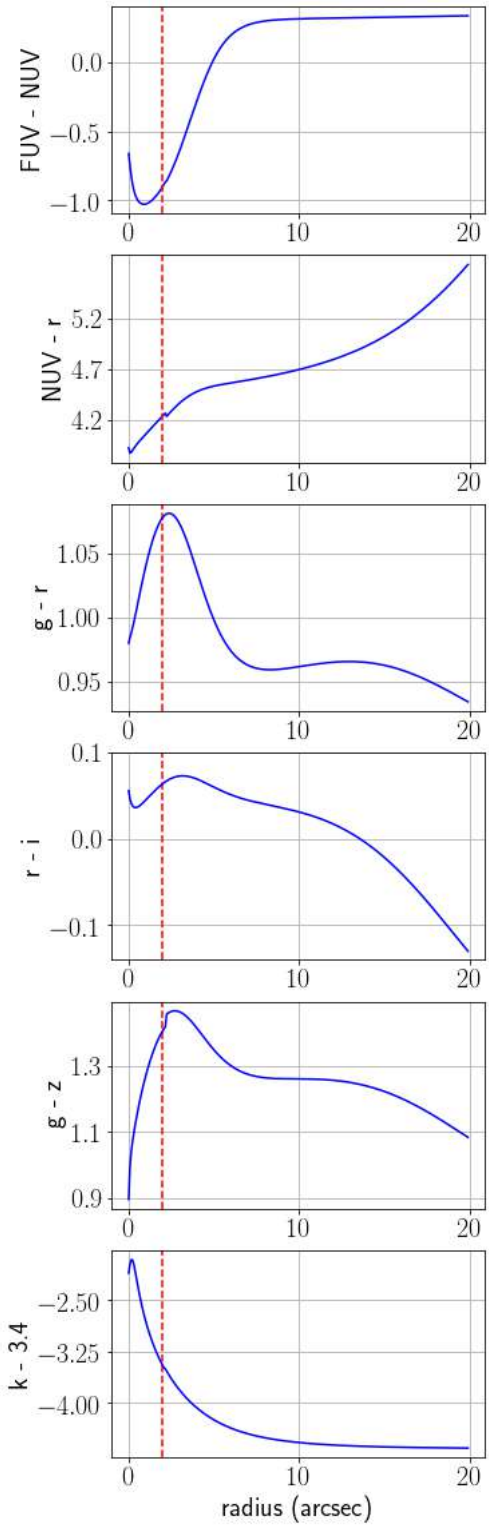

Figure 2.11: Gradient of the colors across NGC 3115. The bluest colors show the youngest populations, whereas the high values highlight older populations.

cannot detect bluer populations in the central region of the galaxy, in comparison to the discs. On the other hand, looking at the gradients including ultraviolet bands, these blue populations start to appear. With these images, we show that our work is consistent with

the literature (Guérou et al., 2016; Poci et al., 2019a; Usher et al., 2019) that propose that the galaxy has a bulge older than the outskirts when using optical data. The inclusion of UV and IR data highlights, though, the presence of blue stellar populations in the center, with high dust content. To see if this blue population observed is due to AGN activity or a recent star formation event, we study below the spectral energy distribution of the galaxy and its components.

2.4.2 SED fitting

In this section we describe the SED fitting process that allowed us to derive stellar masses and star formation rates for the galaxy and its components.

For the SED fitting process, we used two codes: LePHARE (Ilbert et al., 2006) and CIGALE (Burgarella et al., 2005; Noll et al., 2009). Each of the codes has their pros and cons. With LePHARE, using the templates from Bruzual and Charlot (2003), we are able to recover ages for the galaxy and its components that are consistent with the literature (provided in the sixth column of Table 2.3), however, LePHARE does not provide accurate errors in the estimates of the physical parameters and makes use only of simple stellar populations to derive the SEDs. CIGALE, on the other hand, allows for more realistic SEDs, creating the fit including the contribution of dust emission and attenuation models, AGN models, as well as the SSPs from BC03, providing great estimates of the galaxy properties. In CIGALE, however, a star formation history is chosen, and although this provides better estimates of the stellar mass ($M_\star$) and star formation rate of the galaxies, it does this in expense of unrealistic galaxy ages. In this work, we use the delayed star formation history (SFH) model.

- LePHARE, (Ilbert et al., 2006): This code can be used in two manners:

    1. Photometric Redshifts: using a set of template models at different redshifts, LePHARE performs a χ^2 minimization to find the best model that fits a set of magnitude points, retrieving the redshift of the object. For more details, see Section 4.4, where we perform a detailed study of galaxies in the S-PLUS survey to retrieve their photometric redshifts.
    2. SED fitting: if one chooses to fix the redshift, LePHARE works in a different way, trying to find the best fitting model to a set of magnitude points. In this

case, it returns the recovered Spectral Energy Distribution (SED) of the object and the main physical properties that define these models, such as mass, age and metallicity.

The latter is the method used in this chapter to understand the properties of NGC 3115 and its components.

To perform the SED fitting we have used the templates from Bruzual and Charlot (2003). In total, these are 26 Simple Stellar Population (SSP) models computed using the Padova 1994 evolutionary tracks. These models were computed using the Chabrier (2003) Initial Mass Function (IMF), with lower and upper mass cutoffs of $m_L = 0.1M_\odot$ and $m_U = 100M_\odot$, respectively, and using 6 different metallicities:

$$Z = 0.0001, 0.0004, 0.004, 0.008, 0.02(Z_\odot), 0.05$$

.

Finally, these models allow for 9 different star-formation histories, with:

$$\tau = 0.1, 0.3, 1, 2, 3, 5, 10, 15 \text{ and } 30,$$

where τ measures the exponential decrease of the SFR function, defined as:

$$SFR(t) \sim e^{-t/\tau}. \tag{2.5}$$

It is important to mention that these models do not include extinction. Moreover, it is important to reinforce that LePHARE will be used only to recover ages for the galaxy and its components, the other parameters will be retrieved with the code CIGALE. The results obtained with LePHARE are shown in Table 2.3.

- CIGALE (Burgarella et al., 2005; Noll et al., 2009): In order to accurately and consistently estimate properties of the galaxy, we perform SED fitting with and without the AGN models. CIGALE allows one to optionally include AGN emission templates in the SED fitting, which means that one can quantify how the derived galaxy properties are affected by the inclusion or exclusion of AGN emission templates in the fit.

As shown by Almeida et al. (2018), NGC 3115 is the nearest galaxy hosting a billion solar masses black hole and it hosts a low luminosity AGN (LLAGN). Even knowing that the AGN activity in this galaxy is low, it is still a challenge, when dealing with a galaxy hosting an AGN, to determine what is the impact of this AGN emission on the SED of the galaxy, being able to accurately decompose the galaxy SED into stellar, dust, and AGN components. The AGN can have a significant effect on the light of the galaxy SED and its components across a wide range of wavelengths, especially in the bulge of the galaxy. Since in this work we aim to understand if the blue color observed in the bulge is the result of recent star formation events in this region or emission of the AGN (or a composite), we use CIGALE to perform the SED fitting, accounting for models that include both the contribution of stellar and AGN emission.

We fit a total of 12 free parameters to the SED fit of the galaxy and its components: 6 parameters for the star formation history (SFH), 1 parameter for the dust attenuation, and 5 parameters for the AGN emission templates. In our SED fitting, we include the AGN emission models of Fritz et al. (2006), models of dust emission attributed to star formation (Dale et al., 2014), and the stellar populations of Bruzual and Charlot (2003). We assume the dust attenuation model described by Calzetti et al. (2000), a Salpeter IMF (Salpeter (2005)), and a delayed exponential SFH with a constant burst/quench term:

$$\begin{aligned} &\mathrm{SFR(t)} \propto \mathrm{t} \times \exp(-\mathrm{t}/\tau), \text{ when } \mathrm{t} < \mathrm{t_{trunc}} \\ &\mathrm{SFR(t)} \propto \mathrm{r} \times \mathrm{SFR}\ (\mathrm{t} = \mathrm{t_{trunc}}), \text{ when } \mathrm{t} > \mathrm{t_{trunc}} \end{aligned} \tag{2.6}$$

where r is the constant burst/quench term, defined as the ratio between SFR(t) and SFR($\mathrm{t} = \mathrm{t_{trunc}}$) at $\mathrm{t} > \mathrm{t_{trunc}}$, and $\mathrm{t_{trunc}}$ represents the time at which the SFR changes given by a burst or quench event (for a full description of the star formation history models, see Ciesla et al., 2018). Moreover, Ciesla et al. (2017) showed that the delayed SFH provides a good estimate of the SFR on main-sequence galaxies, starbursts, and rapidly quenched systems at all redshifts.

It is especially important to include AGN emission in the SED fit of lenticular galaxies, as it can have a drastic impact on the derived properties of the host galaxy and

Table 2.3 - SED Fitting results obtained from the CIGALE and LePHARE codes. The sixth column shows the ages obtained with LePHARE using the SSP models from Bruzual and Charlot (2003). The other properties were obtained with CIGALE and are divided in two: containing AGN models in the fitting process and without AGN models.

	Component	**SFR** ($M_\odot\,yr^{-1}$)	**Z**	$M_\star\,(M_\odot)$	**Age (Gyr)** (LePHARE)
Without AGN	Bulge	25.2 ± 1.6	0.05 ± 0.01	$(2.9 \pm 0.3) \times 10^{10}$	12.0 ± 2.0
	Thick disc	13.3 ± 1.4	0.04 ± 0.01	$(1.2 \pm 0.4) \times 10^{9}$	10.0 ± 1.0
	Thin disc	9.8 ± 3.5	0.03 ± 0.02	$(5.9 \pm 3.4) \times 10^{9}$	10.5 ± 1.0
	Total	29.5 ± 1.5	0.05 ± 0.01	$(3.4 \pm 0.3) \times 10^{10}$	12.0 ± 3.0
	Ellipse	28.6 ± 2.9	0.05 ± 0.01	$(3.1 \pm 0.7) \times 10^{10}$	11.5 ± 2.0
With AGN	Bulge	12.9 ± 2.0	0.04 ± 0.01	$(1.3 \pm 0.4) \times 10^{10}$	
	Thick disc	2.4 ± 0.3	0.05 ± 0.01	$(2.6 \pm 0.6) \times 10^{9}$	
	Thin disc	1.9 ± 0.2	0.02 ± 0.01	$(2.0 \pm 0.4) \times 10^{9})$	
	Total	14.4 ± 1.8	0.05 ± 0.01	$(1.4 \pm 0.4) \times 10^{10}$	
	Ellipse	8.6 ± 1.8	0.02 ± 0.01	$(8.1 \pm 2.9) \times 10^{9}$	

bring light to the role of the AGN in the evolution of S0 galaxies. For example, in the UV and optical wavelength range, a large portion of the emitted light of a galaxy hosting an AGN can be attributed to the AGN emission given by the accretion disc, and could thus explain the blue colors that are observed in the bulge of NGC 3115. The key reason for us to use CIGALE is that it includes the AGN emission in the SED fit, then carefully removes this emission from the derived galaxy properties, so the resulting SFR and stellar mass will be those intrinsic of the host galaxy and independent of the AGN contribution.

The resulting SEDs obtained with CIGALE including AGN models are shown in the left column of Fig. 2.12 and the SEDs without AGNs in the right column. In the figure, we also indicate the contribution of dust emission and attenuation and of stellar emission.

The results shown in Fig. 2.12 are summarized in Table 2.3, showing the main physical properties obtained for the galaxy and its components with CIGALE including and not including AGN models in the fitting process. For completeness, in the final column of Table 2.3, we also show the ages obtained with LePHARE using the stellar population models of Bruzual and Charlot (2003).

From Fig. 2.12 and Table 2.3, we begin to understand the influence of the AGN in the emission of the galaxy and its components at different wavelength ranges. As several works have shown before (Dolfi et al., 2020; Guérou et al., 2016; Arnold et al.,

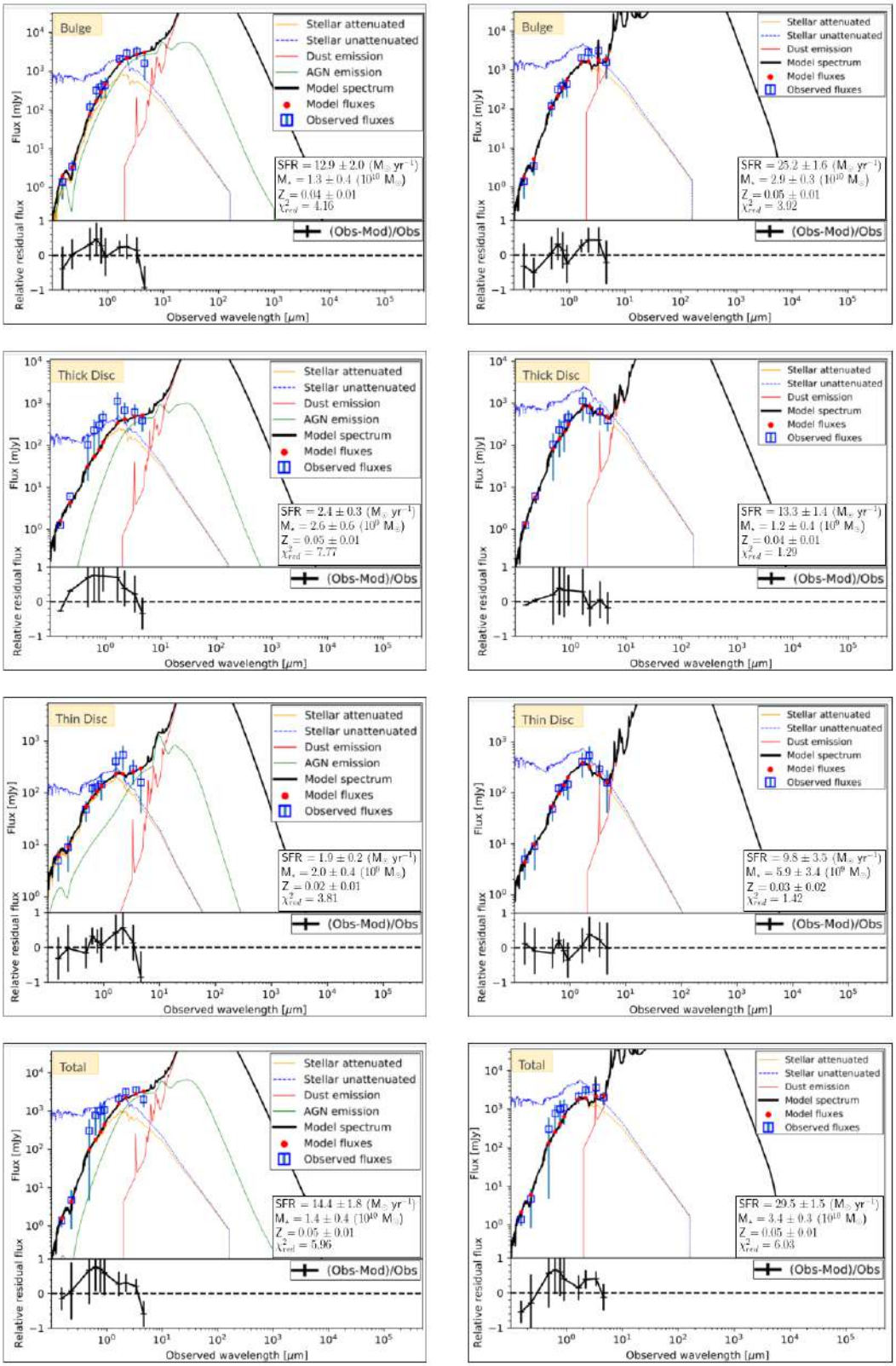

Figure 2.12: Spectral energy distribution of each subcomponent of NGC 3115: bulge, thick disc and thin disc, and the total model of the galaxy, which are shown in each line, respectively. In the left column we show the SEDs obtained including AGN models in the fit and in the right we show the SEDs without AGN models. Additionally, in each panel, we show the retrieved physical properties. The blue squares stand for the input fluxes, the red dots are the model fluxes, the black line is the modelled spectrum, the orange line is the stellar attenuation, red line is the dust emission, blue dashed line is the stellar emission unattenuated and green line (only present in the plots in the left) is the AGN emission.

2011), the galaxy is overall old and with low amounts of gas in all components, as shown by the results obtained with LePHARE in the sixth column of Table 2.3. However, using photometric data in the UV, we were able to detect blue colors in the bulge of the galaxy (see Section 2.4.1), inconsistent with the old ages derived in these other works and with LePHARE. Assuming these ages are correct, the emergence of this blue color could be then due to a recent star formation event in the center of the galaxy, or it could be an artifact given to AGN emission.

Comparing the SEDs obtained using AGN models and without them in CIGALE, we can actually measure the influence of the AGN emission in the SED of the bulge (and the galaxy as a whole). Firstly, focusing on the results of the bulge displayed in the first and sixth lines of Table 2.3, we see that the difference in the SFR from the fitting with and without AGN emission is significantly large (around 10 solar masses a year). So, excluding the AGN emission, the colors observed in the bulge in the previous section would be less blue. Nonetheless, even excluding the AGN emission, we can see that the SFR of the bulge is still high and larger than the other components, showing that there may be a star formation event occurring in the center of the galaxy, together with the AGN activity. We also see that the mass of the galaxy is mainly in the bulge, where the super massive black hole lies.

Going outwards to the thin disc, we see a strong decrease in the SFR, that grows again when reaching the thick disc, where the effect of minor mergers and accretion of companions would account for the larger rates of star formation.

Finally, we compare the results obtained with GALFITM for the total model of NGC 3115 (bulge+thick+thin disc) with results obtained with Ellipse in IRAF -a tool to measure the photometry of objects in increasing isophotes- to check if the results that we are obtaining with GALFITM are reflecting realistic features of the galaxy. One important reinforcement to make in this comparison is that Ellipse integrates the light of the galaxy until the outermost isophote, whilst GALFITM integrates until infinite, so the magnitudes obtained are expected to be fainter for Ellipse, so the SED results should reflect these differences. we see, however, that the results are equal within errors, showing again the strength of GALFITM in recovering the galaxies' properties in the model.

2.5 Discussion

2.5.1 Residuals

The residuals of NGC 3115, i.e., our best fit model subtracted from the input images, are very peculiar and show the same patterns independently of the code used to fit the image, raising the question whether there are other components in the galaxy.

Guérou et al. (2016) proposed that the outskirts of the galaxy exhibit reminiscent of spiral arms, which can be seen as very shallow symmetric structures in almost every residual image of the galaxy (see Fig. 2.15).

Moreover, analysing the residuals of the image, we observe a central component similar to a bar. Adding a fourth component to our fit (a Sérsic model with Sérsic index lower than 1), we were able to fit such structure, a Sérsic profile with n lower than 1 is typical of a bar. However, we could only add this fourth component in the model of the SUBARU images, because of the higher SNR. The images in UV and IR are faint and even the model without a bar is hard to be fitted (see the residuals in FUV band, for example, with hints of over-extraction of light).

However, knowing that the model in the optical bands is improved with the addition of the bands, we looked for alternative ways to prove the hypothesis of the presence of this bar. We compared NGC 3115 with two simulated galaxies: one with a bar and one without a bar to see which ones were more similar and showed similar residuals.

The unbarred simulation is the star-forming simulations described in Clarke et al. (2019) and Beraldo e Silva et al. (2020) (who refer to it as FB10). It forms clumps at early times which produce a thick disc in the system. The bar simulation, on the other hand, is a pure N-body (no gas or star formation) simulation initially comprised of a thin+thick disc. This model is similar to the thin+thick disc simulations described in Debattista et al. (2017), but with the initial thick disc having a scale-height of 900 pc. After it forms a bar, we view the system edge-on with the bar end-on.

For the comparison, we have created unsharp masks for the r band of NGC 3115, for the unbarred galaxy and the barred galaxy. The unsharp mask is an image sharpening technique, which consists on digitally blurring or "smoothing"the original image. This operation suppresses features which are smooth (i.e., which have structure on large scales) in favor of sharp features (those with structure on small scale), resulting in a net enhance-

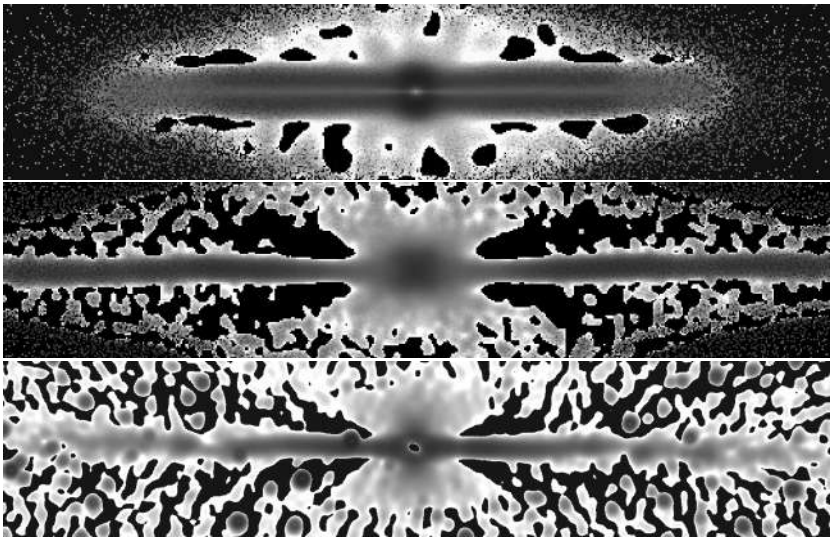

Figure 2.13: **Top**, unsharp mask of a simulated unbarred galaxy with a bulge, thick and thin discs. **Centre**, unsharp mask of a simulated barred galaxy, also with a bulge, thick and thin discs. **Bottom**, unsharp mask of the r band of NGC 3115.

ment of the contrast of fine structure in the image. The unsharp masks used in this work were created using a 25 by 25 median box to create the median subtracted image and a circular Gaussian smoothing with sigma = 5.

Top panel of Fig. 2.13 shows the unsharp mask of the simulated unbarred galaxy, where it is possible to see a star formation stripe in the centre of the galaxy. The simulated barred galaxy is shown in the central panel of Fig. 2.13 and the unsharp mask of the r band of NGC 3115 in the bottom panel of Fig. 2.13.

It is clear that the hourglass shape present in the unsharp-mask image of the r-band image is also present in the simulation of the barred galaxy, indicating that this feature is probably caused by the presence of a bar. Guérou et al. (2016) also reported the possible existence of an end-on bar, based on the study of the correlation of the rotation velocity and the second moment of Gauss-hermite (h3).

2.5.2 Dwarf Companion

By studying NGC 3115, we noticed a small companion to this galaxy, the dwarf galaxy KK084. This small galaxy was studied as part of the globular cluster system of NGC 3115 in several previous papers (Cantiello et al., 2014; Kuntschner et al., 2002; Jennings et al., 2014). In order to understand if this dwarf galaxy was created in the process of formation of its lenticular counterpart, we decided to study its stellar population and colours, to see

if they share properties that could be related to their formation histories.

To do this, we fitted the dwarf galaxy with GALFITM to retrieve parameters such as effective radius, Sérsic index and magnitude in the different wavelengths; however, this was done solely for the three deep SUBARU images, since they are the only ones in which KK084 is visible. The model created for KK084 uses a single component and is shown in Fig. 2.14.

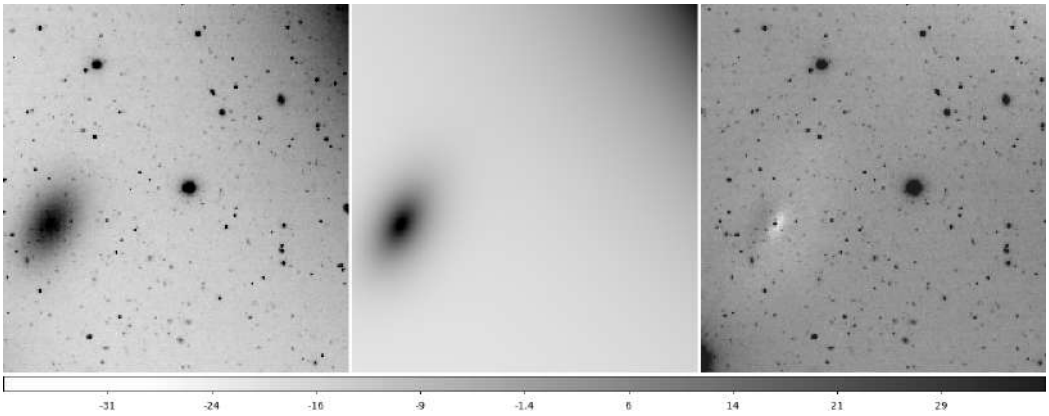

Figure 2.14: Best fitting model of KK084 in the three SUBARU bands, fitted with a single sersic model.

Using the models created with GALFITM, we computed the colours $g-r$, $g-i$ and $r-i$ for the companion and each of the components of NGC 3115 for comparison. These results are shown in Table 2.4.

Colour (mag)	NGC 3115	Bulge	Thick Disc	Thin Disc	Companion
$g-r$	0.99	0.95	0.95	1.11	0.55
$g-i$	1.05	1.03	0.99	1.17	0.92
$r-i$	0.05	0.08	0.05	0.06	0.37

Table 2.4 - Colour of the components of NGC 3115 and the dwarf companion KK084 retrieved using GALFITM.

It is interesting to notice that the (g-r) and (r-i) colours of the companion galaxy differ from the galaxy colour and the colours of the components. Yıldız et al. (2020) proposed that g-r colour images might reveal the presence of dust and sub-structures. We could speculate that the companion galaxy suffered a recent star formation episode caused by the interaction with NGC 3115. Unfortunately this galaxy is too faint to be observed in the other bands and perform an SED fitting. Exploring S-PLUS $H\alpha$ images of NGC 3115 might reveal recent star formation episodes in the galaxy and its periphery.

Moreover, to investigate the stellar populations of the companion and their relation with NGC 3115, we derived the RGB image of the dwarf and the residuals of NGC 3115 (see Fig. 2.15).

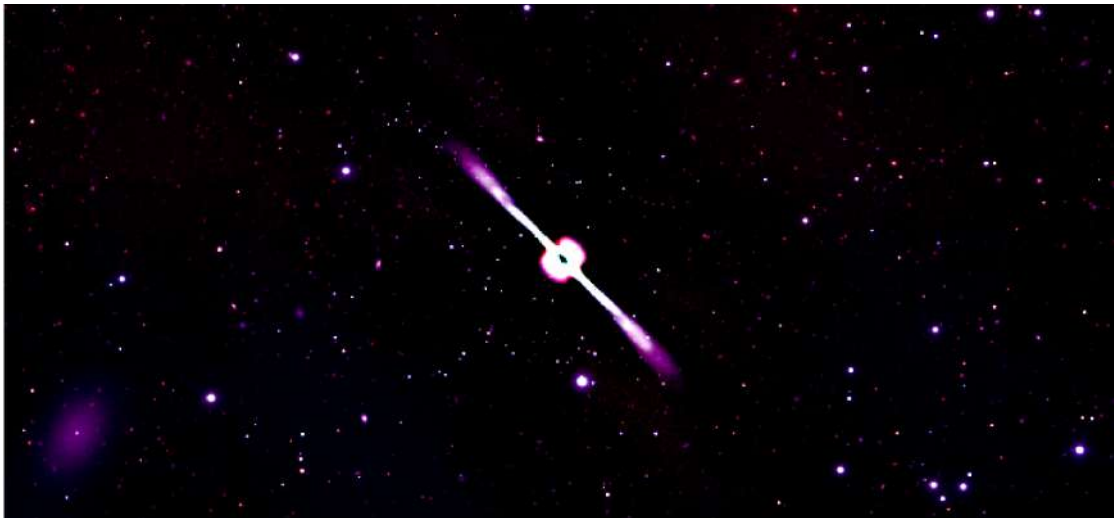

Figure 2.15: RGB image of the residuals of NGC 3115 and its dwarf companion KK084 created using the g, r and i bands of SUBARU.

An extremely interesting feature of Fig. 2.15 is how similar the colour of the companion is to the residuals of NGC 3115. These features seen in the residuals of NGC 3115 have been proposed as remnants of spiral arms. Using the colours retrieved and shown in Table 2.4, we can see that the dwarf galaxy is not very similar to the components of NGC 3115 but it is, however, similar to the spiral arms of NGC 3115, what could mean that they were formed at the same epoch and maybe from the same material. However, for more information, we need spectroscopic data of the faint companion for further comparisons with the great amount of information available for NGC 3115 in the literature.

2.5.3 The Formation History of NGC 3115

NGC 3115 is an unique and extremely interesting object to study. Studying this galaxy, we have faced ourselves with the emergence of several extra components, and also the usually observed bulge and disc of lenticulars. The existence of these components seem to reinforce a complex formation scenario to this galaxy. Moreover, the addition of data in such extended wavelength range, brings up important information regarding the stellar populations of each of these components. As previously discussed, NGC 3115 was largely studied in the past few years, using photometric, spectroscopic and IFU data. Various

works propose the two-phase formation scenario as the most plausible to explain the formation of this galaxy (Arnold et al., 2011, 2014; Guérou et al., 2016; Dolfi et al., 2020). Arnold et al. (2011) describes this formation as the central region being formed in a violent and dissipative event, such as a gas-rich major merger, followed by a sequence of dry minor mergers and accretion events, that would have been responsible for the assembly of the outer bulge and halo of the galaxy. Such scenario would be supported by the declining rotation and metallicity profiles found by their work, using optical imaging and multi-slit spectra. Guérou et al. (2016), using IFU data, recovers the same rotation and metallicity profiles as Arnold et al. (2011) and Arnold et al. (2014). In their paper, Guérou et al. (2016) also bring attention to the emergence of new hypothetical components to this galaxy, such as an end-on bar and a nuclear disc (reinforced by the correlation between the velocity and the second moment of Gauss-Hermite (h3)), and remnants of spiral arms in the faint end of the thin disc of the galaxy. In a more recent study, Dolfi et al. (2020), using a great amount of data on NGC 3115 and faint companions, covering up to 6.5 effective radius on looking through a kinematical point of view, confirms the assembly history proposed by Arnold et al. (2011), showing an older bulge pressure-supported, followed by a transition in the kinematic profile in 0.2 Re to a rotationally supported disc, that goes up to 2-2.5 Re and then changes again to an outer disc pressure-supported. Such transition agrees well with the two-phase formation scenario.

Our results from the analysis of the SED fitting of the components and from the pixelized-CMD seem to agree with the previously proposed scenario for the formation of NGC 3115. We see that all of the components of the galaxy are old, as it was retrieved by Guerou et al. 2016, we see the declining metallicity from the bulge to the outer thick disc, as recovered by Arnold et al. (2011). Moreover, components that were before only hypothetical, such as the thin disc, were taken into consideration in our analysis and we could see the great improvement that the inclusion of this component brought to the model of the galaxy. One difference, however, between our work and the previously cited, is the appearance of blue stellar populations in the central region of the galaxy. The inclusion of images in the ultraviolet has shown the presence of such bluer populations in the bulge of the galaxy, that we propose to be a combination of the nuclear activity present in the galaxy (Almeida et al., 2018) and a recent encounter with the gas-rich companion KK084 that was capable, on one hand, to increase the star formation in the bulge (compatible

with the SFR retrieved from the SED and with the blue color observed in the pixelized-CMD) and, on the other hand, to provoke instabilities in the disc, generating spiral-like/ring features in the faint end of the thin disc. This is reasonable to assume given that the colors of these spiral-like features are similar to the companion, as seen in Fig. 2.15.

Based on all of these results and taking into consideration all of the previous scenarios proposed for the formation of NGC 3115, we propose a complex scenario for the galaxy, where, in a first moment a violent, dissipative gas-rich major merger created the bulge of the galaxy, the remaining gas from the merger was able to generate the observed thin disc of the galaxy (also explaining the similar ages of the components). Instabilities in the disc would have created the central bar, proposed in several works, and such bar would be the responsible for dragging gas from the disc to the center of the galaxy, feeding the SMBH and igniting the AGN activity in the galaxy. The now massive galaxy starts to accrete companions via dry minor mergers, building up the halo of the galaxy. The continuing accretion and increasing mass of the galaxy cause the AGN feedback event, ceasing the star formation in the thin disc. The now without gas thin disc is unable to feed the AGN anymore, diminishing the AGN activity (observed to be low nowadays, Almeida et al. 2018) and the galaxy enters a moment of passivity. A final encounter with the gas-rich companion KK084 is capable of creating a starburst event in the center of the galaxy, explaining the blue population and high SFR observed, and also to cause instabilities in the disc that would generate the spiral-like features observed today.

This formation scenario is summarized in Fig. 2.16.

2.6 Conclusions

In this work we have studied the closest lenticular galaxy to the Milky Way, NGC 3115. For this, we have used 11 images going from UV to IR, observed with different telescopes, to perform multi-wavelength fitting in a broader wavelength range. Using GALFITM we have modeled this galaxy with a set of initial structural parameters to find the ones that best fit the galaxy and its components. The best-fit model of NGC 3115 has three components: a bulge with Sérsic profile described by $n = 3.5$ and $R_e = 21.685$ arcsec, a thick disc and a thin disc.

The SED fitting of the components has shown that the bulge of this galaxy is the

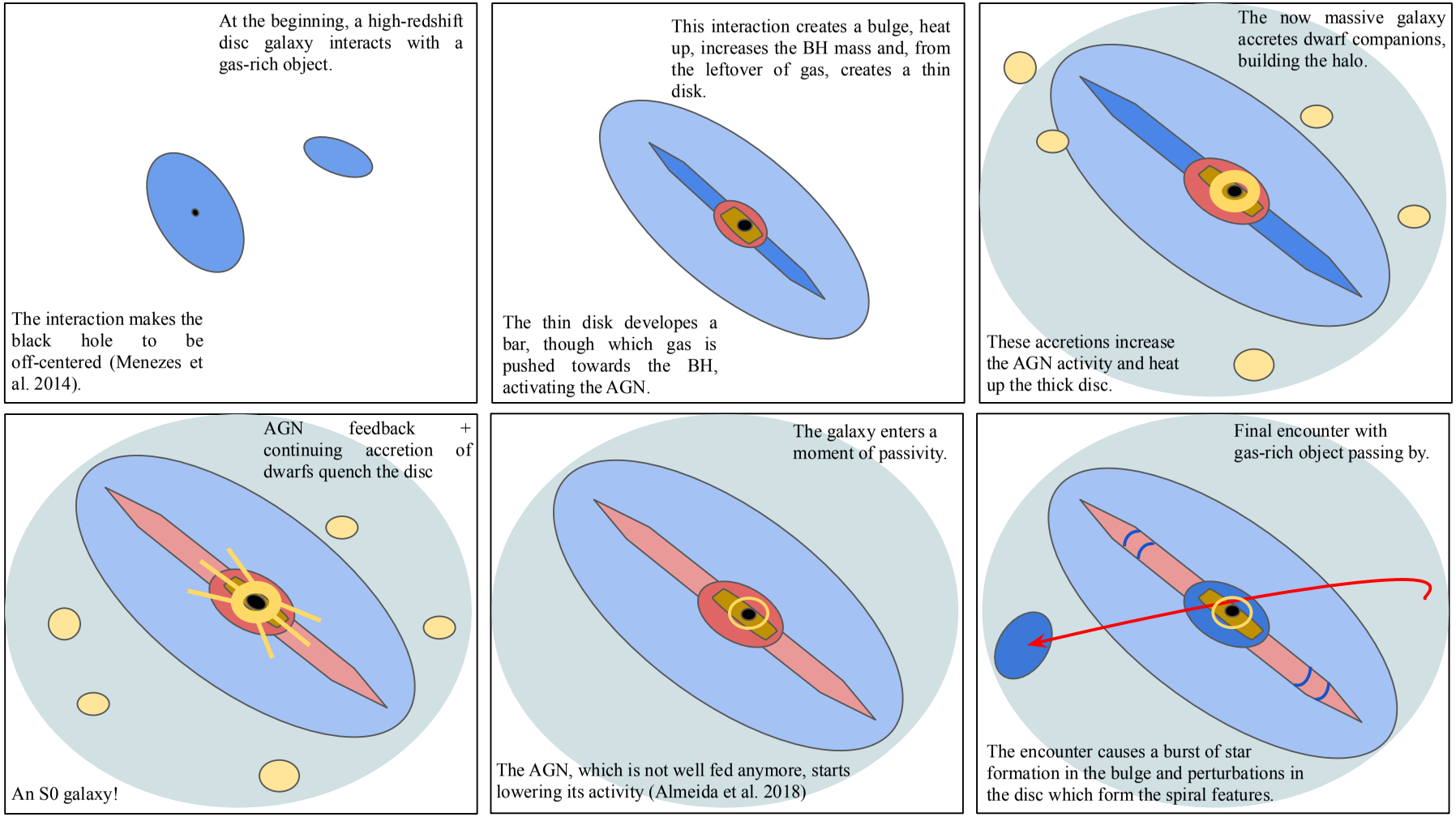

Figure 2.16: In this sketch, we show the proposed method for the formation of the lenticular galaxy NGC 3115, going from an initial gas-rich major merger responsible for forming most of its components, to a sequence of accretions and feedbacks that quench the galaxy, turning it into an S0. A recent encounter with its companion its capable of reigniting the star formation in the bulge and generates instabilities that could lead to the spiral-like features observed.

most massive component, as well as the bluest one. Comparing the SEDs obtained using AGN models and without them in CIGALE, we can see that there are bith AGN activity and a recent SF event that are accounting for the blue populations in the bulge of the galaxy. Going outwards to the thin disc, we see a strong decrease in the SFR, that grows again when reaching the thick disc, where the effect of minor mergers and accretion of companions would account for the larger rates of star formation.

The residuals of our models have shown a possible end-on bar in the center of this galaxy, confirmed by simulations, where we compare the r-band image of NGC 3115, with two galaxies containing a bulge, thick and thin disc, but one of them with a bar. The features such as an hourglass bulge and the flares seen in the barred-simulated galaxy and NGC 3115 confirm that this galaxy has a bar.

We also studied the dwarf companion of NGC 3115, KK084, to understand if this dwarf was formed in the process of formation of NGC 3115. For this, we have modeled this galaxy and retrieved its color-magnitude diagram to understand its stellar populations and colours. Also, using the residual of the fit of NGC 3115, we have studied the spiral arms in the center of the lenticular, before suggested by Guérou et al. (2016), and we show that the colour of the spiral arms are very similar to the ones of the dwarf KK084, suggesting that they could have been formed in the same event (from the same material). Moreover, the colour of these spiral arms suggests that the galaxy may be in the process of reigniting star formation, since these arms are younger than the discs surrounding them and show very blue populations, as the RGB image has shown.

Finally, we propose a scenario for the formation of NGC 3115 based on a initial gas-rich merger, followed by a sequence of accretions and AGN feedback, quenching the galaxy, until a recent encounter with KK084 able of reigniting the star formation in the bulge and generating the spiral features observed.

Chapter 3

Major merger as a possible scenario to create an S0 galaxy: the interacting system NGC 1487

An interaction of a galaxy with other galaxies might change several of its features, thereby shaping its evolution. As described in Section 1.2.2, an S0 can be formed through such a process, becoming the remnant after the interaction has ceased. In this chapter, we focus on the "in between" phase that may lead to the formation of an S0 through mergers, i.e. how are the galaxies affected when they are *still undergoing* such transformations? What can we say about how their features will change with time and, more importantly, how can we observe and analyse these changes? We provide in this chapter an analysis of the interacting system NGC 1487, a case-study to help finding answers to these questions. We point out the specific features that might be imprints of the interaction, and also consider if those could be compatible with the future creation of an S0, given the main theme of this thesis.

Kewley et al. (2006) have shown that interacting galaxies display lower central gas-phase abundances of metals than isolated galaxies at a given mass. This "dilution"in the central abundances may be produced by gas inflows to the galaxy center from the less metal enriched areas in the outskirts of the galaxy. In the same context, observations have shown that interacting galaxies display flatter gas-phase metallicity distributions than non-interacting objects, which is consistent with the scenario described by Kewley et al. (2006), if we consider that these flat gradients may also be associated with gas flows of more pristine gas from the outskirts inwards. The flattening in the metal distribution has been found even at large galactic radii, when considering tidal structures (e.g. Torres-Flores et al. (2014) for NGC92, Chien et al. (2007), for the Mice system). In some cases the

gradients are even inverted, with central values being lower than abundances measured in the outskirts. The origin of these inverted gradients in the local Universe should be linked with gas inflows produced by the interaction events, as in the case of flat metal distributions (e.g Werk et al. (2011)). On the other hand, a few authors have found metallicity drops in the inner regions of dwarf star-forming galaxies. In these cases, metal-poor gas accretion from the cosmic web can explain the metallicity inhomogeneities (e.g. Sánchez Almeida et al. (2014), Sánchez Almeida et al. (2015)). The same scenario may explain the inversion in the metallicity gradient of high-redshift galaxies (Cresci et al., 2010) and maybe this can also be a relevant scenario for interacting systems.

All these theories provide good explanations of how interactions can transform some of the galaxies' features. Nevertheless, only a few studies have confirmed observationally the connection between gas flows and flat metallicity gradients (e.g. Torres-Flores et al. (2015)), mainly due to the lack of suitable instrumentation. In this work, we perform a detailed study of the interacting galaxy NGC 1487 in order to map its metal content and chemical enrichment to help fill in this observational gap. This allows us to understand better galaxies emerging from such interactions and their possible influences and imprints on the formation of S0 galaxies.

To understand the merging system NGC 1487 and the metal mixing process taking place in this galaxy, it is important to analyze data with high spatial resolution, that allows the determination, pixel-by-pixel, of the metal distribution in an interacting/merging system. In this work, we use data from MUSE/VLT which provides spectroscopic information for each individual pixel, with an excellent spectral coverage, to study the interstellar medium of this interacting/merging system.

The different physical parameters derived from the MUSE data allow us to determine the origin of the perturbed metal distribution and to determine which regions deviate from the regular situation (given by non-mergers) in the merging system NGC 1487.

3.1 Data

3.1.1 MUSE/VLT observations

The NGC 1487 MUSE dataset were obtained as part of the "MUSE Atlas Database"campaign (MAD, Carollo et al., 2017; Erroz-Ferrer et al., 2019; den Brok et al.,

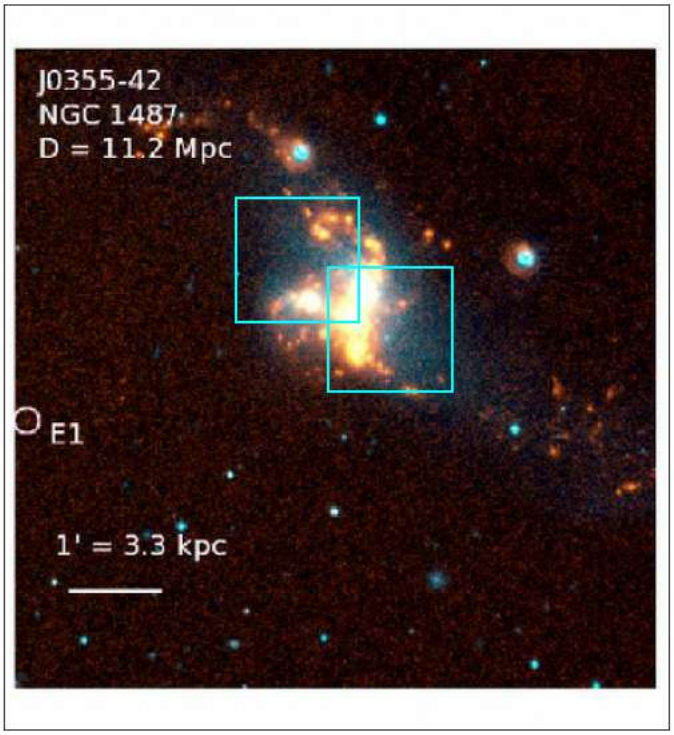

Figure 3.1: GALEX color image of NGC 1487, where blue shows FUV while yellow shows NUV. The blue squares show the MUSE/VLT pointings of NGC 1487.

2019) and has been subsequently released to the community. The MAD database is a sample of 45 galaxies observed to an unprecedented detail.

We here make use of data for only one object that we analyse in detail, including metallicity and kinematic images of the system in order to understand its peculiarities.

MAD was observed as part of the MUSE GTO observations, and the data was reduced using the MUSE Instrument Pipeline (Bacon et al., 2010).

The process of observation and reduction of the data is thoroughly described in Erroz-Ferrer et al. (2019). In their paper, they discuss the properties of 41 out of the 45 sample galaxies, where the 4 galaxies not included are merging systems. NGC 1487 is one of these four galaxies. The process of analysis of this object is more complicated for being a large mosaic. In fact, there were three pointings of this galaxy with MUSE: one in the sky and two in the galaxy itself, with a field-of-view of 1 arcmin^2 each. The alignment and combination of the cubes was done by us using the MUSE Python Data Analysis Framework (MPDAF Bacon et al., 2016) code.

We correct each spaxel for Milky Way extinction using $A_{V,mag} = 0.033$, the value retrieved from NED. Obtained from the Schlafly and Finkbeiner (2011) recalibration of the

Schlegel et al. (1998) dust map. This recalibration assumes a Fitzpatrick (1999) reddening law with $R_V = 3.1$.

3.2 Methods

3.2.1 FADO

FADO (Fitting Analysis using Differential Evolution Optimisation - Gomes and Papaderos (2017)) is a tool designed to perform population spectral synthesis in order to derive different physical parameters from a galaxy spectrum. Population spectral synthesis can be understood as the decomposition of a spectrum in terms of a superposition of simple stellar populations of various ages and metallicities. FADO, different from other fitting routines, uses differential evolution optimization, which leads to greater computational efficiency. The software incorporates a chain of modelling, including pre, post-processing, storage and graphical description of the outputs. The main goal of FADO is to derive the chemical enrichment and star-formation history of galaxies based on 2 elements in spectral fitting models:

1. self-consistency between the best-fitting star formation history and the nebular emission of the galaxy;

2. artificial intelligence algorithms and differential optimization.

FADO is more advantageous than other existing population spectral synthesis codes for the following reasons, according to Gomes and Papaderos (2017):

- It computes and incorporates the contribution of the nebular continuum to the best-fitting SED.

- It identifies the ages, metallicities and mass fractions of individual simple stellar populations that best reproduce the nebular characteristics of the investigated galaxy.

- Using artificial intelligence, it automatically characterises the input spectrum in order to optimise the Simple Stellar Populations (SSP) library and fitting strategy.

- It computes and stores the errors of the computed parameters.

- It computes the electron temperature and density of the ionised gas.

- It determines the intrinsic extinction in the nebular and stellar component.
- It offers high computational efficiency and stability.

The main components of FADO are divided in (1) pre-processing of the spectral data, (2) spectral synthesis and computation and (3) storage of the output. Fig. 3.2 shows what each of these subdivisions is responsible for, in the process of fitting with FADO.

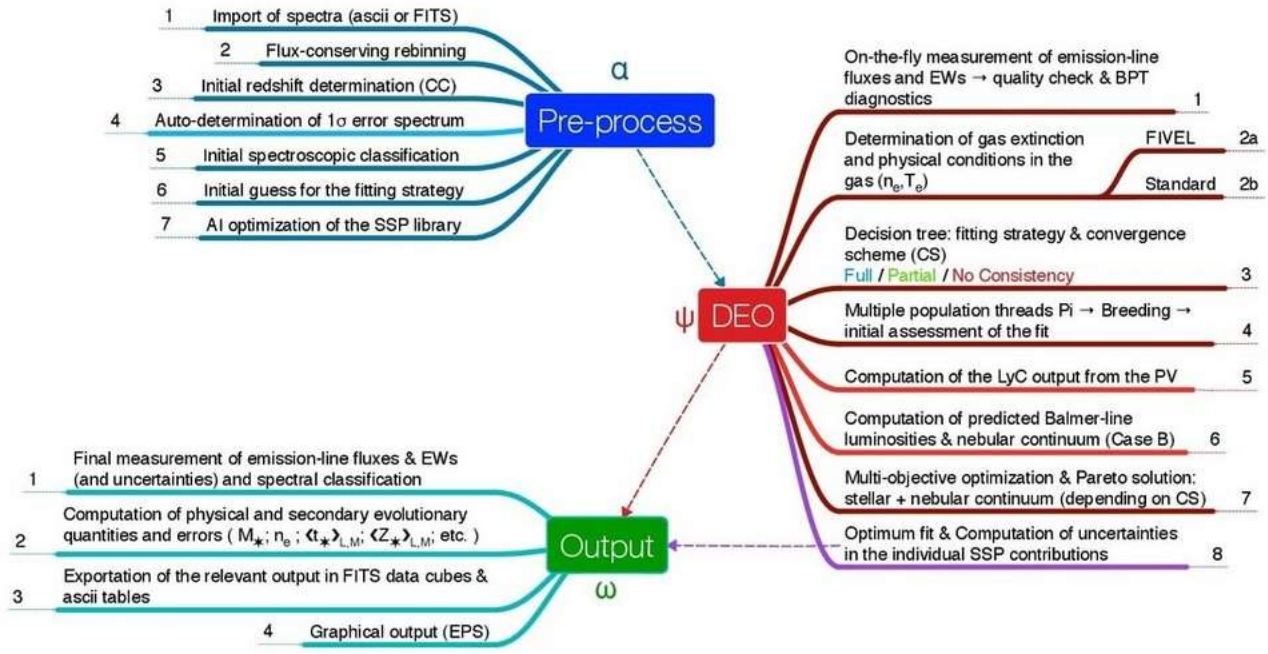

Figure 3.2: FADO's chain of modelling, including all the steps of the pre-processing part, post-processing and the storage and graphical description of the outputs. Image extracted from Gomes and Papaderos (2017).

One important thing to understand about FADO is that this code is designed to study single spectra of galaxies, and it was not developed to study IFU data. Therefore, a first step in using FADO to analyse our data was to refine the code to iterate over all the spectra available in each cube. Since FADO performs its analysis in each spectrum separately, at the end we had the results and models for each spaxel, i.e. a pixel-by-pixel information of the main physical parameters of the galaxy.

We ran FADO for each spaxel of NGC 1487 using:

1. The SSPs from Bruzual and Charlot (2003);
2. The Calzetti et al. (2000) extinction law;

3. The spectral range used in the modelling was $4800-9300$ Å, to include all the redshifted lines and for which the synthetic best-fitting model is exported together with the wavelength step-size, which was set to be 1.25 (half of the spectral resolution);

4. A spectral resolution of 2.51 Å;

5. A luminosity distance of 12.3 Mpc;

6. A recessional velocity of 848.0 km/s;

7. The flux units of 1.e-20 ergs/s/cm^2/A.

In Fig. 3.3 one can see what an output of FADO looks like for one specific spaxel of the galaxy NGC 1487. This result, together with the results from the rest of the cube were used to obtain: 1) emission-line maps, 2) BPT diagrams, 3) electron densities, 4) extinction maps, 5) gas metallicity, 6) mass, 7) star formation rates and 8) velocity fields.

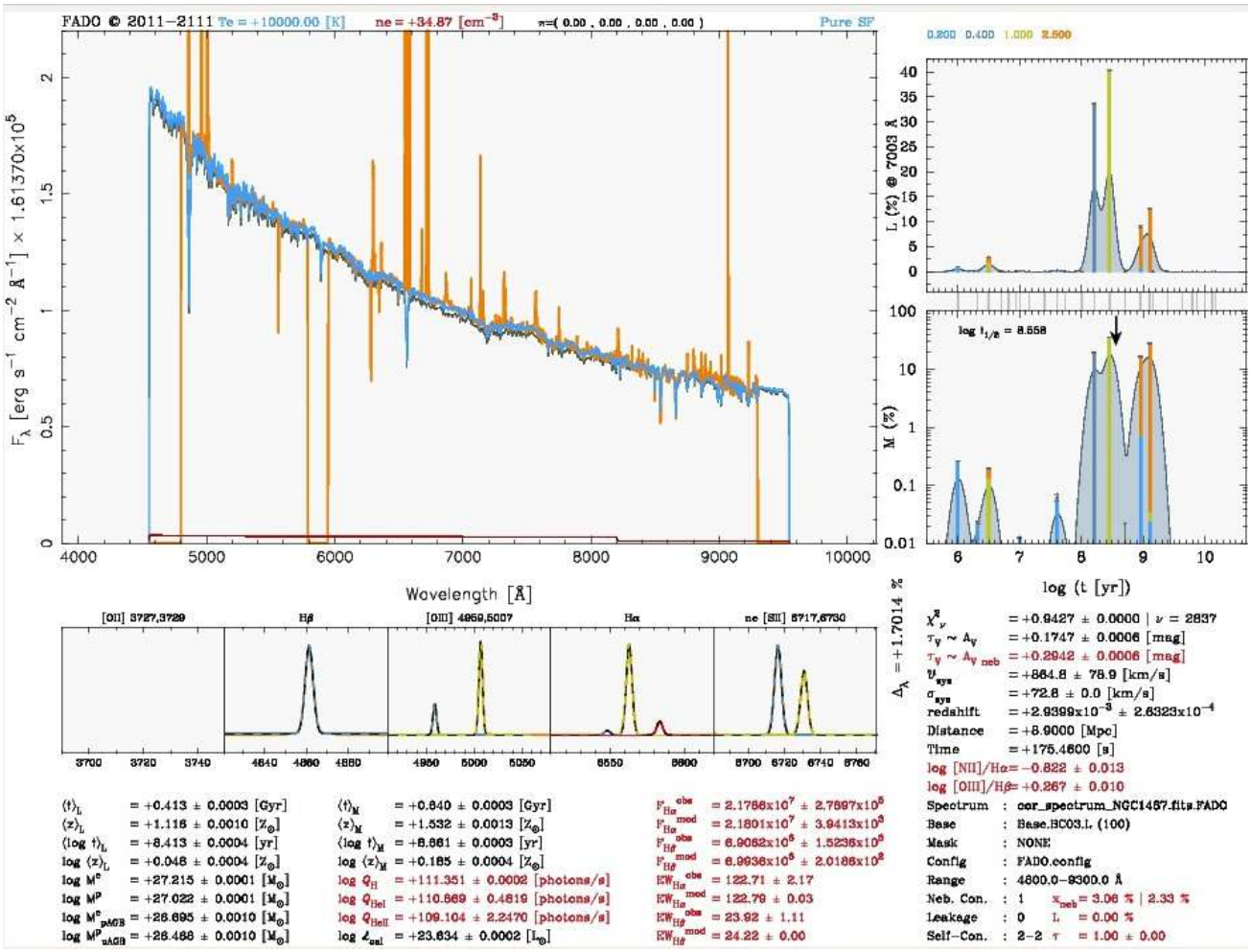

Figure 3.3: Example of FADO output for one spaxel of NGC 1487. This output shows the model created for the spectrum, the predicted and measured line values, the estimated mass, metallicity, eletron density and temperature, as well as the estimated age and classification of the galaxy according to its main ionization mechanism.

It is important to mention that an improved version of FADO is currently being developed to work with IFU data. This code is based on the already existing PORTO3D routine (Papaderos et al., 2013), and will be called FADO3D.

3.3 Ionised gas emission

The MUSE data has the wide wavelength range of $4800 - 9300$, covering all the most important lines, from $H\beta$ to [SII]λ6717, λ6731.

The full cube fitted with FADO is shown in Fig. 3.4, highlighting the four bright condensations called APC1, APC2, APC3 and APC4, which will guide the majority of this work. The identification of these regions were first proposed by Aguero and Paolantonio

(1997).

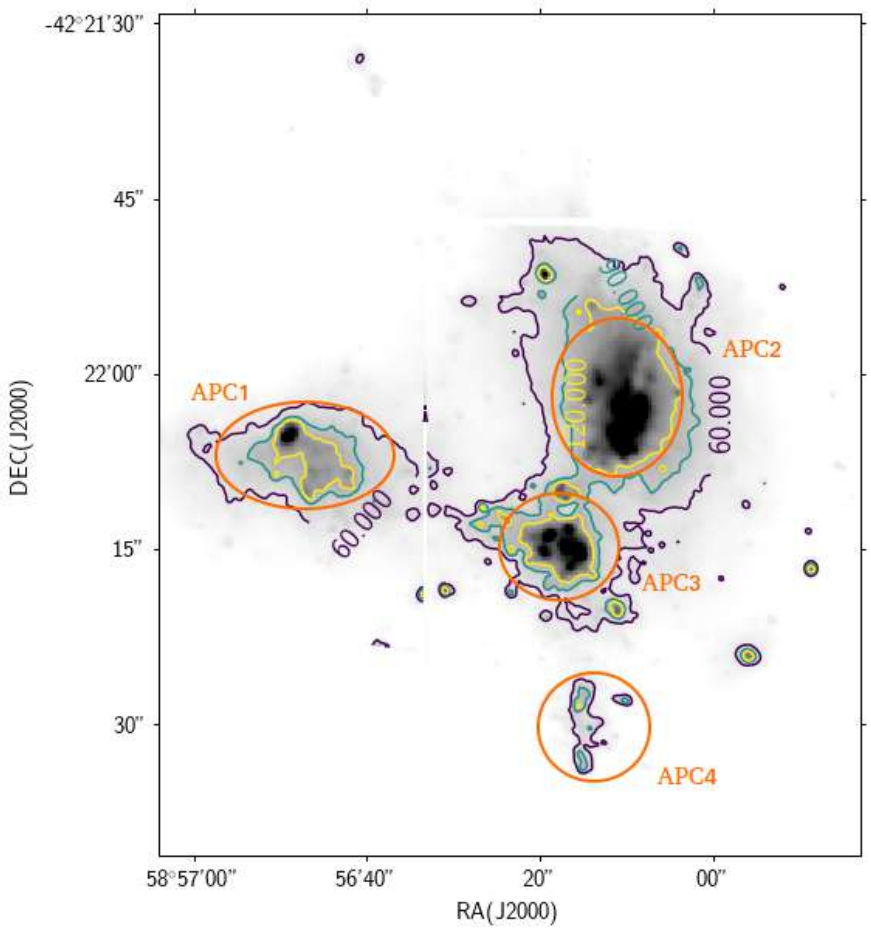

Figure 3.4: Synthesized V-band image of the combined MUSE datacube highlighting the four high condensations in the merging system NGC 1487: APC1, APC2, APC3 and APC4 (Aguero and Paolantonio, 1997). Overlaid in black are the V-band isophotes that will be used to guide the eye in the rest of this dissertation.

The cubes in general show very high singal-to-noise ratios (SNR) for all the emission lines we are interested in, so a Voronoi tesselation would not be necessary if we were interested only in the gas emission. However, for the kinematics, the binning showed a great improvement in the recovered velocity fields and velocity dispersion maps. Therefore, to secure a high quality of the analysis, the spectra in each cube were spatially binned using the Voronoi method of Cappellari and Copin (2003) to achieve a minimum SNR of ≈ 30 per spatial element. The signal-to-noise ratio map of each the emission lines after the Voronoi tesselation is shown in Fig. 3.5. In this figure, we fixed the SNR to vary from 0 to 500 for all lines for a comparison sake.

We can see that the signal-to-noise of the Hα and [OIII] lines are much higher than the other lines. From these maps, we can already see that the four bright condensation

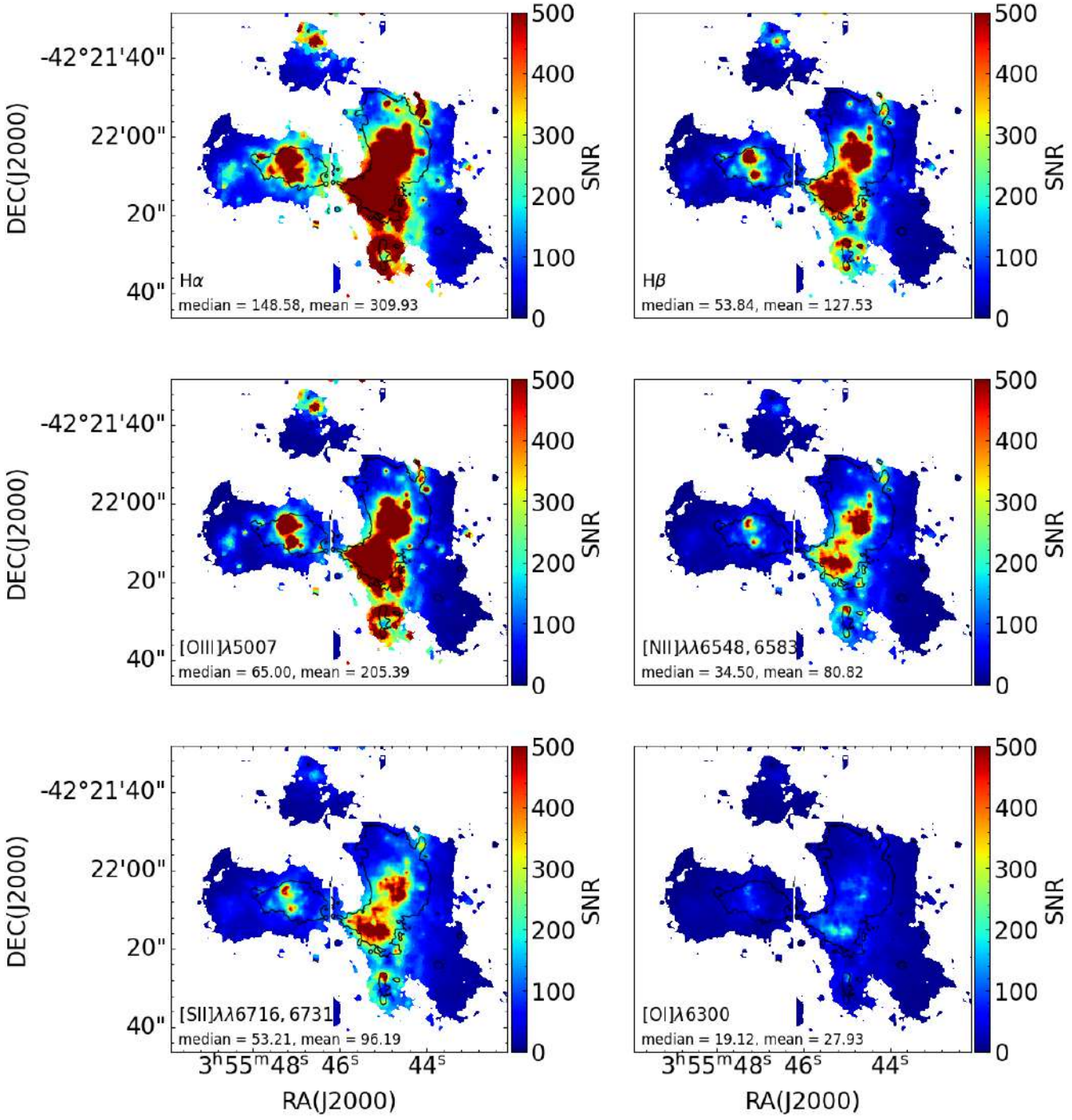

Figure 3.5: Signal-to-noise ratio maps retrieved for the MUSE datacubes of NGC 1487, after a voronoi tesselation to minimum SNR of 30. The maps show the ratios for the lines $H\alpha$, $H\beta$, [OIII]λ5007, [OI]λ6300, [NII]λ6548, [NII]λ6583, [SII]λ6717 and [SII]λ6731, respectively. The black lines represent the V-band isophotes of NGC 1487 derived from the MUSE datacube.

(APC1, APC2, APC3 and APC4) are the parts with higher SNR. One more important remark of these maps is the very low SNR of the [OI]λ6300 lines, which will be used in this work for the derivation of diagnostic diagrams to retrieve the ionization source of the system.

3.3.1 Emission Line Maps

As described in Section 3.2.1, the emission line maps were obtained using the fitting analysis routine FADO. We have derived the maps for the most important lines for our analysis and corrected them all for extinction, which are: $H\alpha$, $H\beta$, [OI]λ6300, [SII]$\lambda 6717, 6731$, [NII]$\lambda 6548, 6583$ and [OIII]$\lambda 4959, 5007$ doublets. In Fig. 3.6 we show the maps derived from this analysis.

We can notice a high Hα emission in the center of the galaxies, especially in the regions of APC2 and APC3, and a very noticeable ring-shaped emission in the location of APC4, which is not visible in the optical image (see Fig. 3.4).

3.3.2 $H\alpha$ emission and dust attenuation

The MUSE datacubes have sufficient continuum SNR, spectral resolution and wavelength range to allow subtraction of the stellar absorption from the Balmer emission lines, which is part of the fitting process of FADO. This allows the measurement of the dust attenuation affecting the nebular lines and the intrinsic distribution of ionized gas. The dust attenuation (A_V,gas) map is constructed from the Hα/ Hβ ratio map using the attenuation law from Calzetti et al. (2000) which is applicable to starbursts and star-forming galaxies.

The emission lines of galaxies are attenuated both by internal and external dust. To account for this, the emission line intensities need to be corrected, first for Galactic extinction (described in Sec. 3.1) and then for internal attenuation. For this work, we assumed a case B recombination with a density of $\eta = 100 cm^{-3}$ and a temperature of $T = 10^4$ K, which gives the predicted ratio (unaffected by reddening or absorption) of $H\alpha/H\beta = 2.86$ (Osterbrock and Ferland, 2006).

According to Brocklehurst (1971) and Izotov and Pilyugin (1994), the effect of redde-

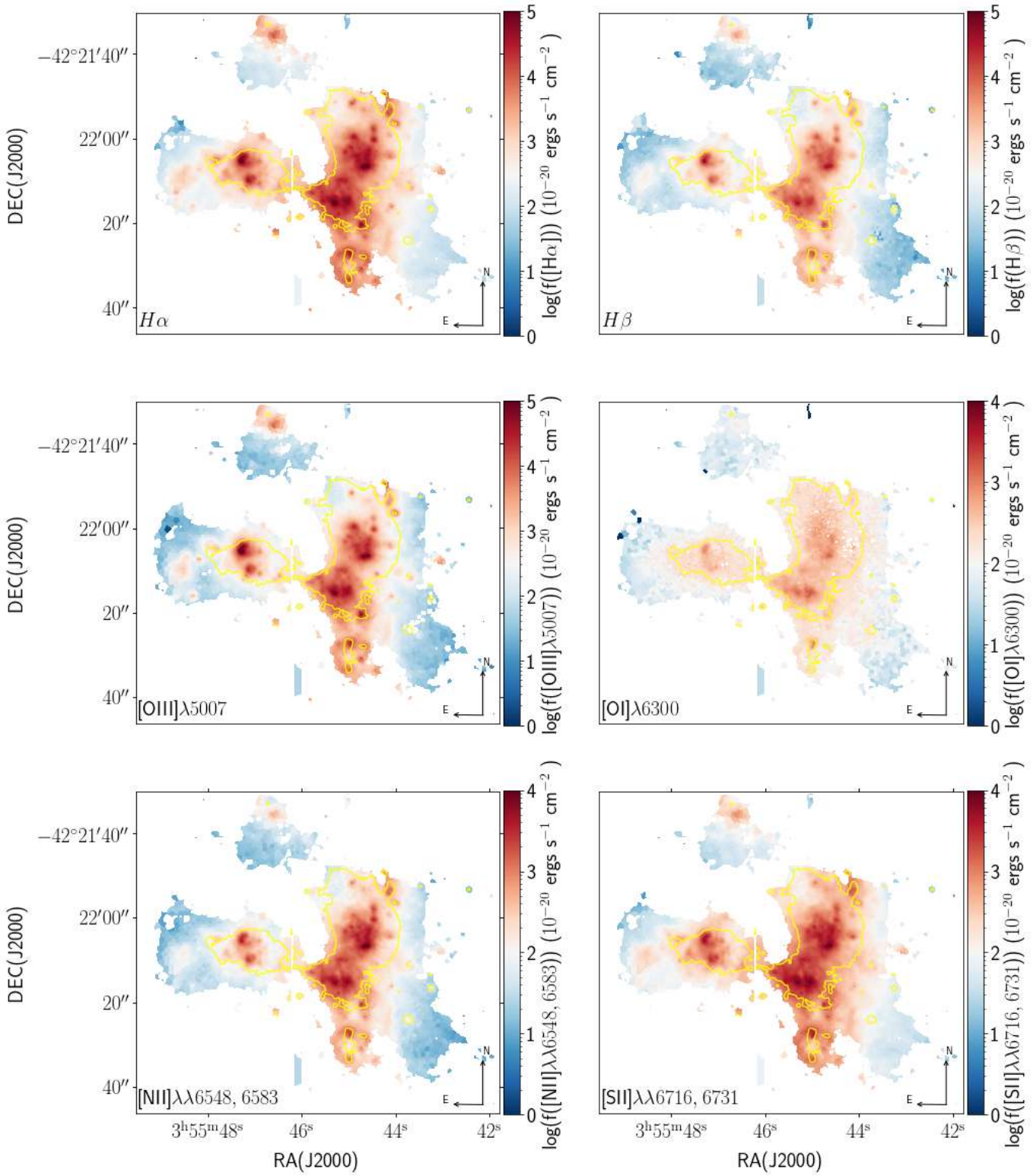

Figure 3.6: Emission line maps retrieved using the fitting analysis FADO. The panels show the uncorrected for extinction maps of: $H\alpha$, $H\beta$, [OIII]λ5007, [OI]λ6300, [NII]$\lambda\lambda$6548, 6583, [SII]$\lambda\lambda$6716, 6731, respectively. The yellow lines represent the V-band isophotes.

ning in the $H\alpha/H\beta$ can be expressed as:

$$\frac{I_{\lambda 1}}{I_{\lambda 2}} = \frac{F_{H\alpha}}{F_{H\beta}} \cdot 10^{0.332c}, \tag{3.1}$$

where $\frac{I_{\lambda 1}}{I_{\lambda 2}}$ is the de-reddened value for the emission line ratio, $F_{H\alpha}$ and $F_{H\beta}$ are the observed fluxes for the $H\alpha$ and $H\beta$ lines, respectively, and c is the reddening parameter, defined by:

$$c = 1.47 \cdot E(B-V) = 1.47 \cdot A_V/3.2 = 0.46 \cdot A_V, \tag{3.2}$$

with $E(B-V)$ being the color excess and A_V the extinction; knowing that the intrinsic $\frac{F(H\alpha)}{F(H\beta)} \sim 2.86$, we have:

$$F(H\alpha) = 2.86 \cdot F(H\beta) \cdot 10^{0.152\,A_V}. \tag{3.3}$$

Therefore, the dust attenuation can be expressed as:

$$A_V = 6.579 \cdot \log_{10}\left(\frac{F(H\alpha)}{2.86 \cdot F(H\beta)}\right). \tag{3.4}$$

Using this equation, we can correct the $H\alpha$ emission for dust together with the equation derived by Seaton (1979) to correct an observed flux for reddening defined as:

$$F_{corr} = F_{obs} \cdot 10^{0.46 \cdot A_V \cdot (1+f(\lambda))}, \tag{3.5}$$

where F_{corr} stands for the corrected emission, F_{obs} the observed flux and $f(\lambda) = -0.325$, from Izotov and Pilyugin (1994), with $\lambda_{H\alpha} = 6563$Å. Finally, the corrected $H\alpha$ emission is calculated as:

$$F(H\alpha)_{corr} = F(H\alpha) \cdot 10^{2.03 \cdot \log_{10}\left(\frac{F(H\alpha)}{2.86 \cdot F(H\beta)}\right)}. \tag{3.6}$$

Under the assumption of spherical symmetry, the luminosity of the $H\alpha$ emission line can be calculated as follows:

$$L(H\alpha) = 4\pi \cdot D_L^2 \cdot F(H\alpha)_{corr}, \tag{3.7}$$

with D_L being the luminosity distance, calculated at $12.3 Mpc$ for the galaxy NGC 1487.

Fig. 3.7 shows the observed Hα line flux, the emission line attenuation map (A_V,gas) and the dust-attenuation corrected (intrinsic) Hα line luminosity.

We measure a maximum attenuation of 0.9 mag in the center of APC2 and in the NE part of APC3, typical for an ordinary star-forming galaxy. High attenuation regions are observed in the tidal tails and outer-regions of the galaxy as well. After correcting for

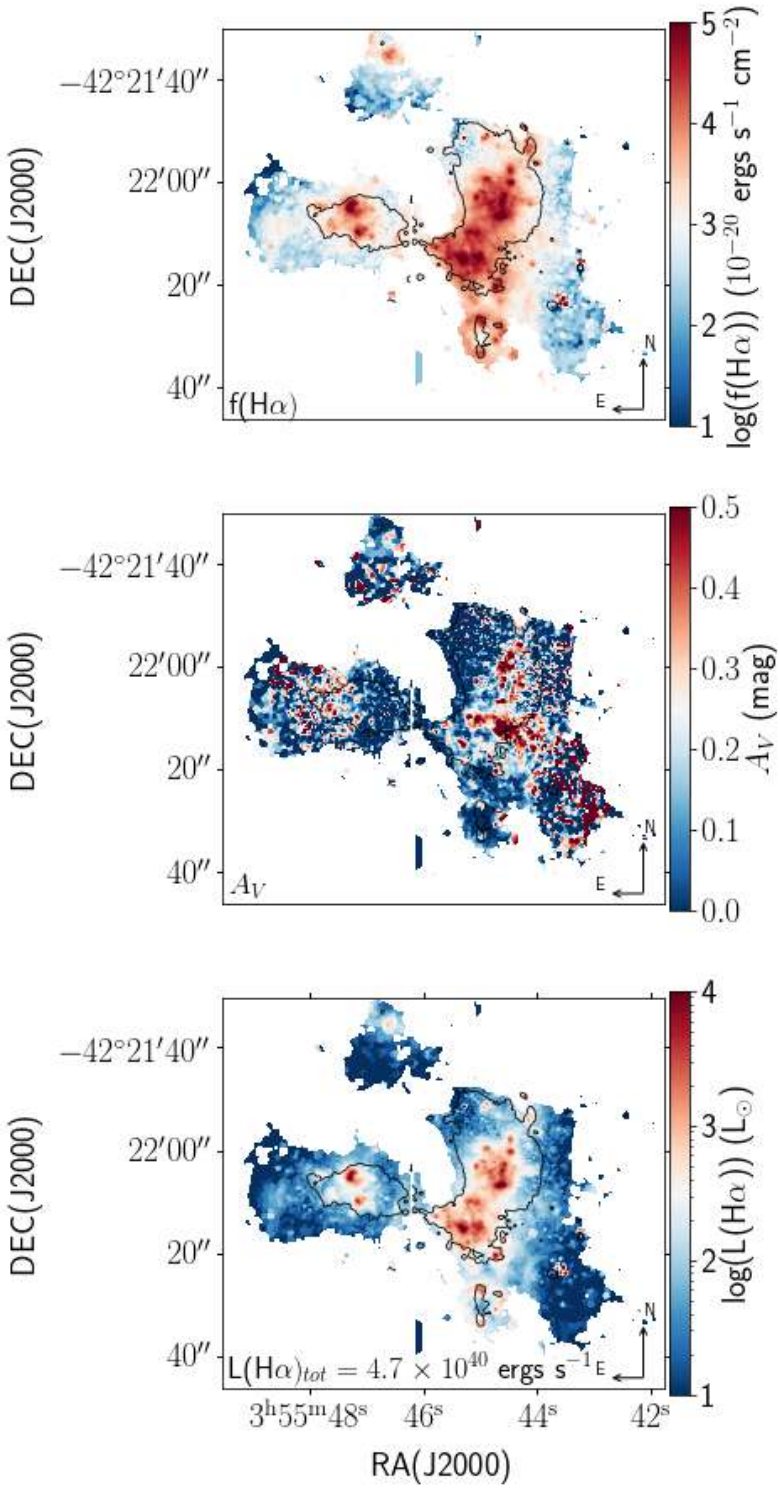

Figure 3.7: 2D-maps from the MUSE dataset. The black contours indicate the V-band isophotes as displayed in Fig. 3.4. *Top:* $H\alpha$ emission line flux. *Center,* Emission line attenuation calculated from the observed $H\alpha/H\beta$ emission line ratio and dust attenuation law of Calzetti et al. (2000), suitable for low redshift star-forming galaxies. *Bottom,* Dust attenuation corrected $H\alpha$ luminosity surface density.

the dust attenuation, we see the ionized hydrogen emission is concentrated in the central regions of the galaxies and show very low luminosity in the outer-regions and in the NW part of APC2.

We can notice a high Hα emission in the center of the galaxies, especially in the regions of APC 2 and APC3, but more noticeable is the ring-shaped emission in the location of APC4, which is not visible in the optical image (see Fig. 3.4).

3.3.3 Emission line ratios sensitive to ionization source and Diagnostic Diagrams

Standard line ratios sensitive to the shape of the ionizing spectrum ($[NII]\lambda6583/H\alpha$, $[SII]\lambda6731/H\alpha$, $[OIII]\lambda5007/H\beta$ and $[OI]\lambda6300/H\alpha$) are shown in Fig.3.8.

The line ratios make it clear that the the ionization source of the galaxies is mainly generated by photo-ionization by stars. The maximum value encountered for log([NII]/Hα) was -0.44, whereas the maximum ratio observed to classify star-forming galaxies from Kauffmann et al. (2003) is N[II]$/H\alpha = -0.25$, we can conclude that all the spaxels are in the star-forming region of the diagram, but the BPT diagrams were constructed to confirm thess results.

The BPT diagnostic diagrams (Baldwin et al., 1981) are used to distinguish the ionization mechanism taking place on the nebular component of galaxies. For this, they use a set of emission line ratios sensitive to the main ionization source of the system. In this work, we derive the three most commonly used BPT diagrams: ([NII]$\lambda\lambda6548, 6583/H\alpha$), ([SII]$\lambda\lambda6717, 6731/H\alpha$) and ([OI]$\lambda6300/H\alpha$). These diagrams show dividing lines that were developed as a function of the ionization models (e.g., Veilleux and Osterbrock, 1987; Osterbrock, 1989; Kauffmann et al., 2003; Kewley et al., 2001, 2006; Stasińska et al., 2006; Kewley et al., 2013). These lines separate objects mainly ionized by star-formation from those ionized by active galactic nuclei (AGN), they can also be classified as low-ionization nuclear emission-line regions (LINERs) and Seyfert galaxies depending on where they fall on these diagrams. A composite ionization by star-formation and AGN is also possible and delineated in the diagrams. These diagrams are shown in Fig. 3.9, where the different colours represent the regions APC1, APC2, APC3 and APC4.

From Fig. 3.9 we see that the system is primarily ionized by photo-ionization, with very few points of APC1 and APC2 in the AGN regions of the BPT-SII diagram. To see where these points are located in the system, we created a 2D BPT-SII (Fig. 3.10) diagram. In

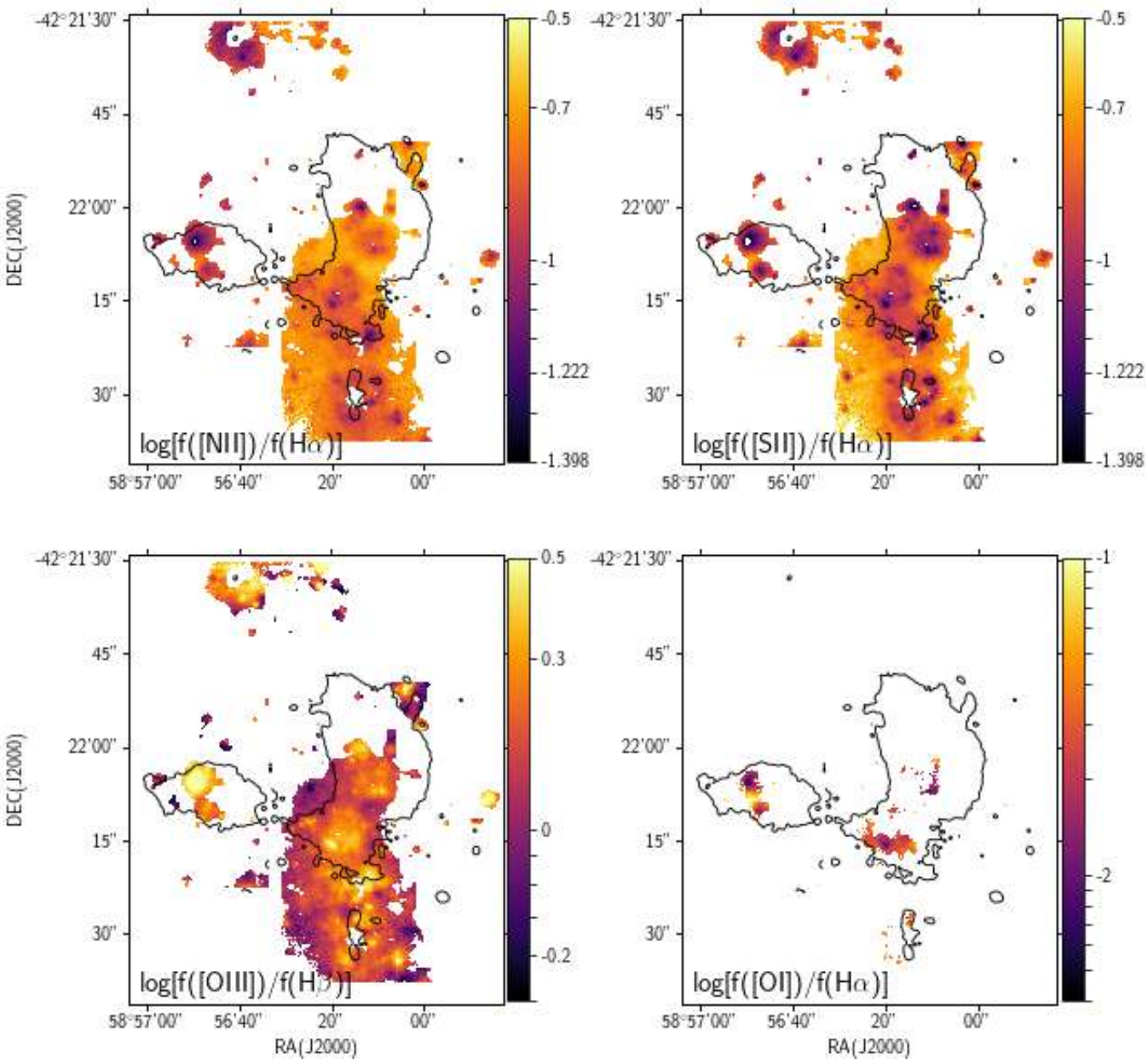

Figure 3.8: Diagnostic diagrams computed from the MUSE dataset. *Top left to bottom right:* emission line flux ratio maps for $[NII]\lambda6583/H\alpha$, $[SII]\lambda6731/H\alpha$, $[OIII]\lambda5007/H\beta$ and $[OI]\lambda6300/H\alpha$. The black contours indicate the V-band isophotes.

this map, we color in blue the spaxels that lie below the main separator between SF and AGN ionization, and in red the spaxels that are above the line.

From Fig. 3.10 we can see that all of the spaxels identified to be primarily ionized by nuclear activity are in the outskirts of the galaxy or in regions with low SNR (see Fig. 3.5 of the SII lines.

Belfiore et al. (2016) show, using a sample of galaxies observed with the MaNGA survey,that there are galaxies that are mainly ionized by star formation, but show spaxels

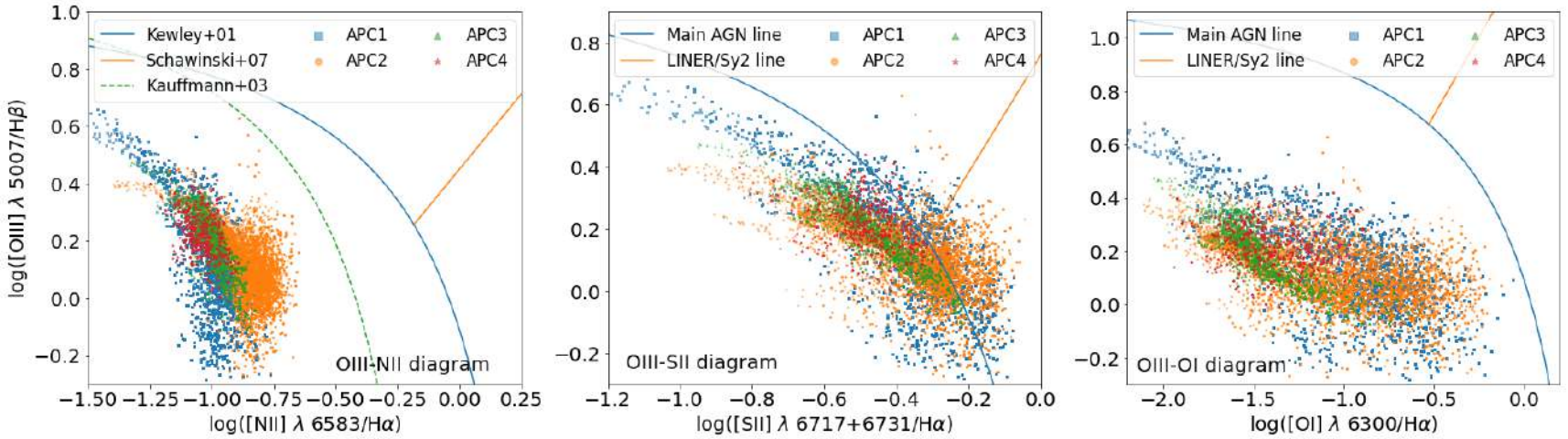

Figure 3.9: Line ratio diagnostic diagrams from the MUSE dataset, showing line ratios for independent spaxels in NGC 1487. The diagrams are the BPT-NII, BPT-SII and OI, respectively, from left to right. Overplotted as blue lines are empirically and theoretically derived separations between star-forming regions and AGNs (Kewley et al., 2001), as orange lines are the separations between LINERs and Seyferts (Stasińska et al., 2006), and the green line in the BPT-NII diagram delineate the composite region between star-forming and AGN (Kauffmann et al., 2003). The color of the dots stands for their position across the galaxy. Blue squares are in APC1, orange points in APC2, green triangles in APC3 and red stars in APC4.

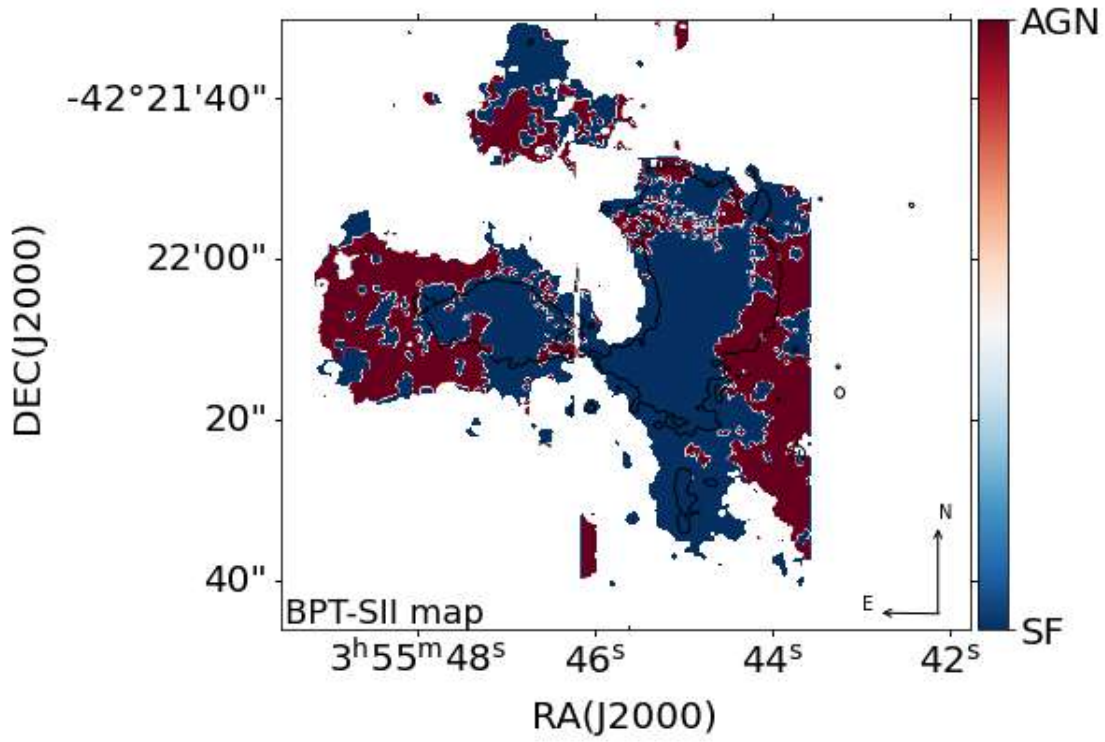

Figure 3.10: 2D BPT SII diagram. The colormap shows the spaxels mainly ionized by star formation (in blue) and by nuclear activity (in red).

in the LINER and AGN region of the BPT-SII diagram, however, similar to our case, these spaxels are mostly in the outer-regions, where AGN acitivy is rarely found. They call these galaxies "LIERs"(firstly introduced by Stasińska et al. (2008)), for showing a large amount of spaxels in the LINER region of the BPT and not actually having this type of ionization. Specifically, they show the example of one inidividual merger between two star-forming galaxies (MaNGA-ID 12-193481), where the central regions and most of the tails are dominated by SF line ratios, but a large fraction of the more diffuse gas shows line ratios falling beyond the SF sequence in the BPT diagram (both LIER-like and Seyfert-like). They attribute this behaviour to shocks, non-virial motions and outflows that may be playing a major role in the ionization structure of this type of systems.

3.3.4 Emission line ratios sensitive to gas density

The electron density, Ne, is one of the key physical parameters characterizing an ionized gaseous nebula. The electron density can be measured by observing the effects of collisional de-excitation on forbidden emission lines. In the optical wavelength region, the most commonly used density-diagnostic ratios are $[OII]\lambda3729/\lambda3726$ and $[SII]\lambda6716/\lambda6731$.

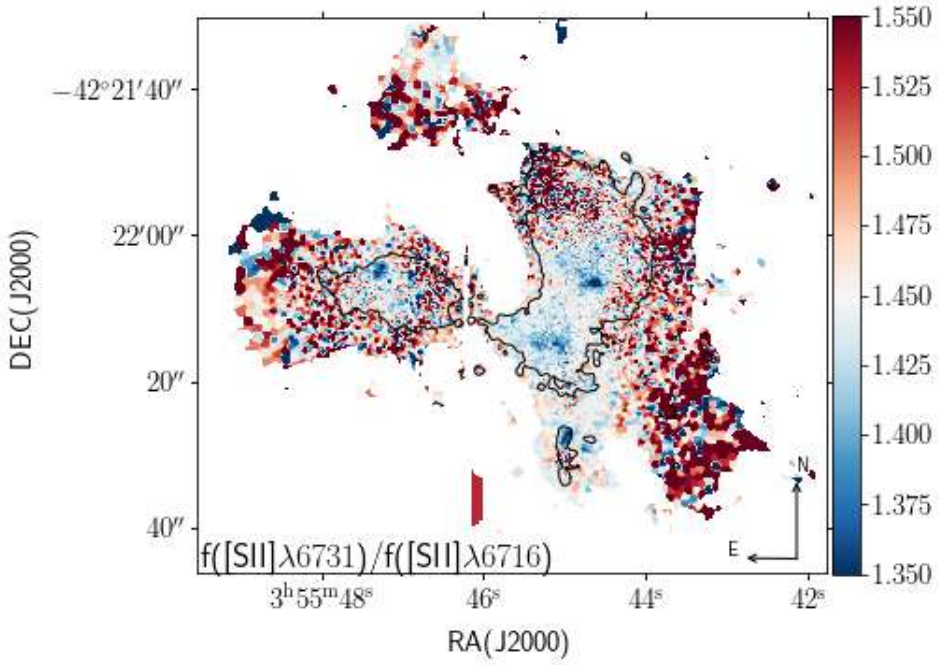

Figure 3.11: [SII]λ6731/[SII]λ6717 line ratio map, indicating the variation in electron density.

Since the wavelength range of the MUSE data starts at 4800 Å, we used the [SII] doublet to derive the electron density in this system.

In Fig. 3.11 we show the [SII]λ6731/[SII]λ6717 line ratio which is primarily sensitive to the electron density of the emitting gas. This ratio is ~ 0.4 where $n_e \approx 10^5$ (cm^{-3}) and 1.4 for electron densities $n_e \approx 100$ (cm^{-3}) (at $Te = 10^4$, Osterbrock and Ferland (2006)).

All condensations show complex distributions in their gas densities. Regions with particularly low [SII] ratios (higher densities) are the central regions of APC1, APC2 and APC3. Although APC4 has a large emission in Hα, it shows less concentration of gas (higher SII ratios). The gas density of the galaxies varies mostly between 1.3 and 1.5, showing that in all parts the electron density $ne \leq 100$cm^{-3}.

3.3.5 Gas-phase metallicities and Star Formation Rates

The most accepted formation scenario for galaxies consists on an inside-out formation (White and Frenk, 1991; Mo et al., 1998), where the stars in the central regions are formed before the stars in the outskirts. As a consequence, we see a metallicity decreasing with galactocentric radius (i.e. negative gradient). As discussed in the introduction, non-interacting galaxies show, in general, negative oxygen abundance gradients (Searle, 1971), consistent with this formation scenario. Interacting galaxies, however, seem to have flatter

metallicity gradients than isolated galaxies, likely because of gas flows induced by the merger.

The study of the gas-phase metallicity distribution of this system is one of the major goals of this work.

The chemical composition of galaxies provides an important insight on the processes governing the evolution of galaxies. There are still many open questions about the internal processes that drive chemical evolution and the importance of the environment in shaping the evolution of galaxies.

There are several methods for estimating the metal content of a galaxy. One of these methods is to analyse the emission lines of gaseous nebulae to estimate the abundance of the interstellar gas.

The oxygen abundances in this work were computed using the calibration by Marino et al. (2013) which uses the O3N2 index described as:

$$O3N2 = \log(([OIII]\lambda5007/H\beta)/([NII]\lambda6583/H\alpha)). \tag{3.8}$$

By using this index together with stellar evolutionary synthesis and photoionization models, Marino et al. (2013) proposed an empirical metallicity calibration described as:

$$12 + \log(O/H) = 8.533[\pm0.012] \; - \; 0.214[\pm0.012] \times O3N2. \tag{3.9}$$

We calculated metallicities from the [OIII] and [NII] emission lines (Pettini and Pagel, 2004) in all regions, but here we focus on the parts where the line ratios indicate the gas is primarily photo-ionized by hot stars (APC1, APC2, APC3 and APC4).

Flat gradients in interacting systems are expected, but such a flat gradient is expected to only occur in later stages of a merger (Kewley et al., 2010). Therefore, studying the metallicity gradient of the galaxy, we can have an idea of the stage of the merger of NGC 1487. However, knowing that the galaxy is already one galactic body, it is expected that the system is experiencing at least some flatness in the gradient currently.

Another indicator of the stage of the merger is the star formation rate of the system. Several studies show that mergers are responsible for creating high star formation episodes. However, Bergvall et al. (2003) show that the ignition of the star formation is dependent on the properties of the progenitor galaxies and if a gas-rich merger can evolve to a poor starburst system. In the regions of the galaxies where the gas is photo-ionized by light from

stars, we can measure the SFR from the dust attenuation corrected Hα line luminosity, using the standard conversion to star formation rate (Kennicutt, 1998). For the remaining regions we also obtained SFR estimates, but these are only an upper limit on the SFR, because a fraction of the Hα flux in these outer-regions must arise from processes unrelated to star formation.

In the regions not dominated by star formation (regions identified to be in the AGN/LINER regions in the BPT diagrams), where the dust attenuation is larger, it is possible that the attenuation correction is leading to incorrect emission line strength estimates and therefore non-reliable SFR estimates.

To calculate the SFR, we start from the $H\alpha$ emission line, which is one of the most reliable SFR indicators. The $H\alpha$ nebular emission arises directly from the recombination of HII gas ionized by the most massive O- and early B-type stars and therefore traces the star formation over the lives of these stars. The luminosity of the $H\alpha$ recombination line is directly coupled to the incident number of Lyman comtinuum photons produced by these young stars, and is hence proportional to the SFR. The $H\alpha$ luminosity was already derived in Section 3.3.2, assuming a case-B recombination. The luminosity of the $H\alpha$ line, as well as the broadband colours of galaxies, are known to be very sensitive to the slope of the Initial Mass Function (IMF) (See van de Sande et al. (2015)). The Salpeter IMF (Salpeter, 2005) was proven to fit the properties of normal spiral galaxies better than other IMFs and is the adopted IMF when deriving SFRs from nebular emission lines (Dutton et al., 2012). We can use the dust attenuation corrected Hα luminosity to estimate the star formation rate (SFR) in the galaxies, by applying the Kennicutt (1998) conversion:

$$\mathrm{SFR}(M_\odot\,\mathrm{yr}^{-1}) = 7.9 \times 10^{-42}\ \times L(H\alpha)(ergs\ s^{-1}), \tag{3.10}$$

and, given that

$$L(H\alpha) = 4\pi \cdot D_L^2 \cdot F(H\alpha)_{corr}(ergs\ s^{-1}), \tag{3.11}$$

we have:

$$\mathrm{SFR}(M_\odot\,\mathrm{yr}^{-1}) = 7.9 \times 10^{-42} \cdot 4\pi \cdot D_L^2 \cdot F(H\alpha)_{corr}(ergs\ s^{-1}). \tag{3.12}$$

Since $F(H\alpha)_{corr}$ is in units of $10^{-20}\ ergs\ s^{-1}\ cm^{-2}$, when converting from Mpc to cm^2, we have:

$$\mathrm{SFR}(M_\odot\,\mathrm{yr}^{-1}) = 7.9 \times 10^{-42} \cdot 4\pi \cdot D_L^2 \cdot 9.52 \times 10^{48}[cm^2] \cdot F(H\alpha)_{corr}(10^{-20} ergs\ s^{-1}\ cm^{-2}). \tag{3.13}$$

By converting to SI units, equation 3.13 will have the form:

$$SFR(M_{\odot}\,\mathrm{yr}^{-1}) = 9.45 \times 10^{-12} \cdot D_L^2 \cdot F(H\alpha)_{corr}(ergs\ s^{-1}) \tag{3.14}$$

with $D_L = 12.3Mpc$ for NGC 1487.

Fig. 3.12 shows the oxygen abundance and star formation rate maps retrieved using the O3N2 index and the conversion from Kennicutt (1998). To trace the metallicity and SFR across the system, we draw lines cutting the system in several positions and directions to guide the estimation of the gradients, these are shown in the bottom panel of Fig. 3.12.

The metallicity of the gas throughout the galaxies range from 8.3 to 8.8, where the lowest metallicities are found in the four central condensations, whereas the higher values are in the outskirts of the galaxies.

As expected, the areas with lowest oxygen abundances are the ones with the highest star formation rates, indicating that the merger should be responsible for bringing less-enriched gas to the center of the galaxies inducing starburst events in these regions. The overall SFR of this galaxy is calculated as $0.37M_{\odot}/yr^{-1}$. Although this galaxy seems to have a higher overall SFR, this phenomena was previously studied for this galaxy in Bergvall et al. (2003).

As previously mentioned, Bergvall et al. (2003) studies a sample of 59 interacting and merging galaxies and 38 isolated galaxies for comparison, using photometric and spectroscopic data. They find that the interacting and merging galaxies in comparison to the isolated ones are more luminous in optical and near-IR and that the dust temperature is higher. However, although this is often claimed as an effect of starburst activity, they favour the explanation that interacting galaxies have higher masses than the non-interacting ones and/or the gas, dust and young stars are more centrally concentrated. For NGC 1487 specifically, they conclude that this is a poor-starburst galaxy, by comparing the emission of the system in the optical (B) and near-IR (H), and although the optical band shows a chaotic signature of a starburst, the nearinfrared counterpart outlines the old stellar populations in the galaxy. They claim that this galaxy could be the merger of several dwarf galaxies, instead of two massive ones, what in turn would increase the mass density and gas mass of the galaxy, increasing the Halpha luminosity, but not necessarily the star formation rate when compared to non-interacting systems.

By analysing the gradients shown in Fig. 3.12, we can see that the central condensations

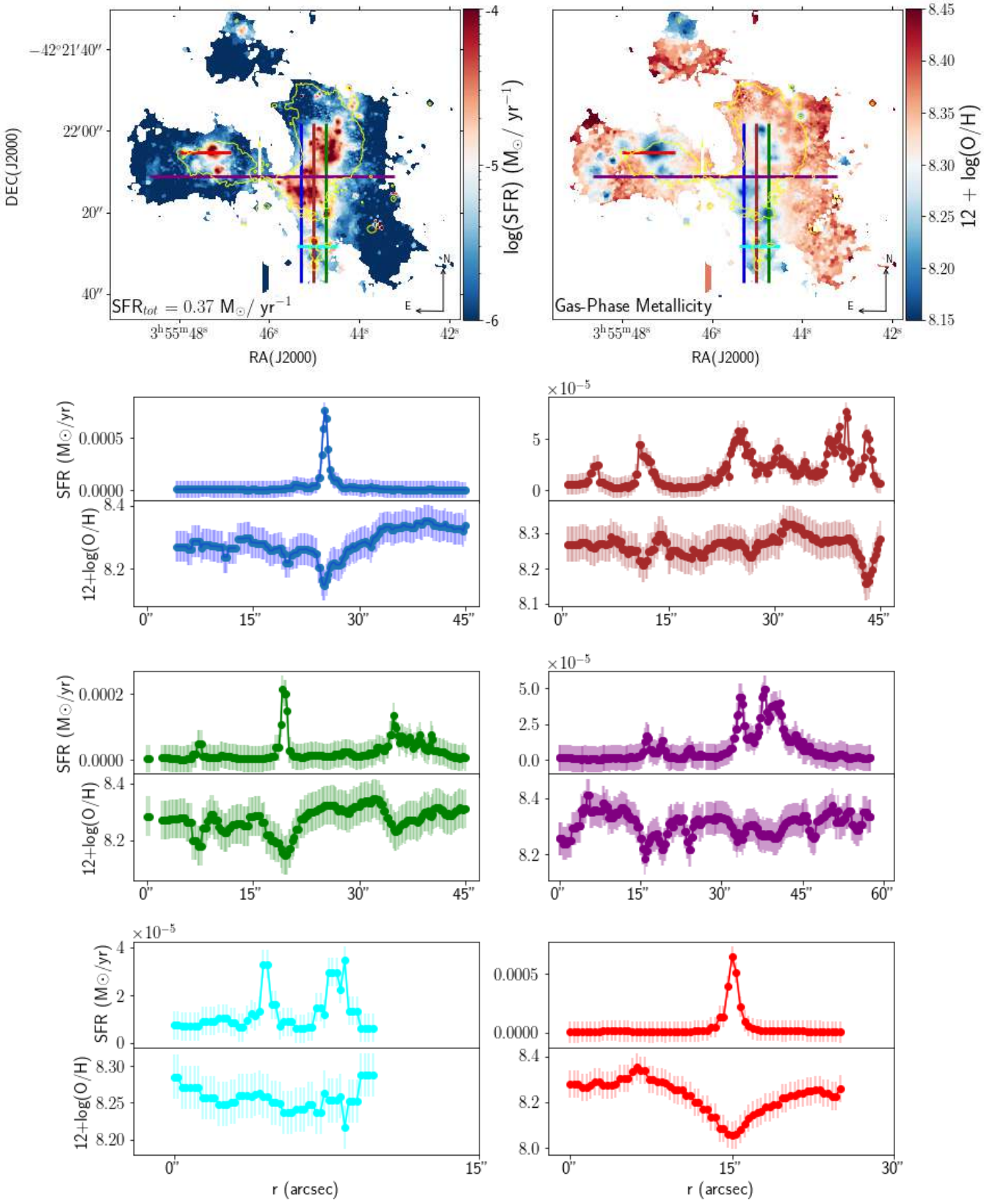

Figure 3.12: Upper row: star formation rate map in the left and oxygen abundance map of NGC 1487 retrieved using the O3N2 method in the right. The black lines represent the V-band contours constructed from the MUSE datacubes. Each line drawn in the maps represents the displayed gradients shown in the bottom panels. Each gradient plot shows in the top the SFR variation and in the bottom the oxygen abundance variation.

show lower abundances than the outskirts, characterizing an inverted metallicity gradient to NGC 1487.

3.4 Stellar Populations

3.4.1 Mass

We calculate the mass of the galaxies using an approximation based on the best-fitting solution out of the SSP "building blocks" picked up from the BC03 library, from now on referred as population vector (PV). In practice, the code FADO is used for that. It gives the most probable mass based on the definition above.

Using the best fit Spectral Energy Distribution (SED) from the input SSPs from Bruzual and Charlot (2003), FADO is able to calculate the most probable stellar mass of the galaxy. The map of the mass in each spaxel is shown in Fig. 3.13.

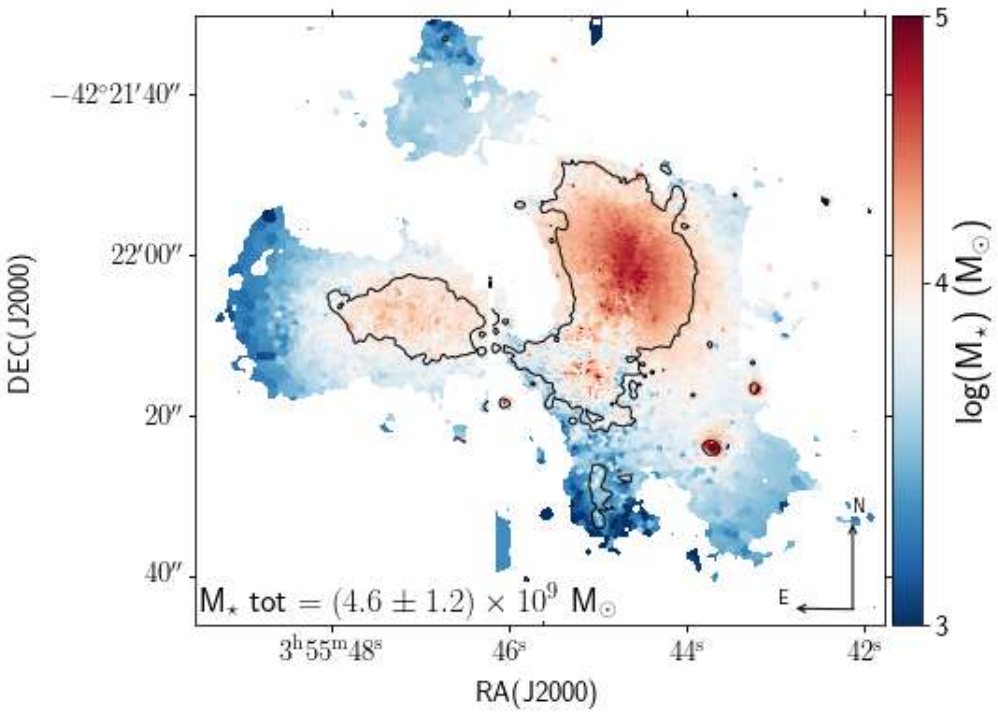

Figure 3.13: Stellar mass presently available in the galaxy. The map shows the mass of each individual spaxel, resulting in a total mass of $(4.6 \pm 1.2) \times 10^9 M_\odot$

These measurements of each individual spaxel allow for the calculation of the global mass of the system, estimated to be around $M_{NGC1487} = (4.6 \pm 1.2) \times 10^9 M_\odot$, consistent with the results obtained by Aguero and Paolantonio (1997). Moreover, from Fig. 3.13

we can see that the region of APC is a factor of 1-2 dex more massive than the rest of the galaxy, what leads to the conclusion that the stellar body of the galaxy is in this regions. The region is the one that shows the lowest SFR among the four condensations also, showing the detachment of the gas and stellar components in the galaxy.

3.4.2 Ages

To calculate the ages, FADO reduces the population spectral synthesis output into a few key variables characterizing the stellar and nebular components of a galaxy. These secondary model quantities, include the first moments of the best-fitting population vector (PV), that is, the mean stellar age and metallicity, expressed both in linear and logarithmic form, for the age, we have:

$$\langle t_\star \rangle_{\mathcal{L}} = \sum_j^{N_\star} \frac{L_{j,\lambda_0}}{L_{\lambda_0}^{total}} t_j = \sum_j^{N_\star} x_{j,\lambda_0} t_j \text{ weighted by light,}$$

$$\langle t_\star \rangle_{\mathcal{M}} = \sum_j^{N_\star} \frac{M_j}{M_\star} t_j = \sum_j^{N_\star} \mu_j t_j \text{ weighted by mass,} \tag{3.15}$$

with $L_{\lambda_0}^{total}$ standing for the total luminosity of the galaxy at the normalization wavelength λ_0, t_j and M_j being the age and mass presently available in the j^{th} SSP contributing a mass fraction μ_j to $\mathcal{M}_\star$. $x_{\lambda_0} = (x_{1,\lambda_0}, ..., x_{N,\lambda_0})$ is the fractional light contribution of SSPs of a given age and metallicity.

The luminosity-weighted stellar age is shown in the left panel of Fig. 3.14. This map reflects the most luminous stars within a galaxy, therefore, it tends to highlight younger stellar populations inside the galaxies and their respective ages.

On the other hand, the mass-weighted stellar age, shown in the right panel of Fig. 3.14 tends to show the older stellar populations, once the older stars are the ones that hold the majority of the mass inside a galaxy.

Converting the observed maps into physical properties, we find an inversion in the age gradient, with the younger stars in the center of the galaxies. The center of APC1, APC3 and the whole region of APC4 have distinctly younger stellar populations, with light-weighted ages of $\sim$ 100 Myr or mass-weighted ages of $\sim$ 300 Myr. The region of APC2 and outer-regions have the oldest mean stellar ages of about 2 Gyr (light-weighted) or 3 Gyr (mass-weighted).

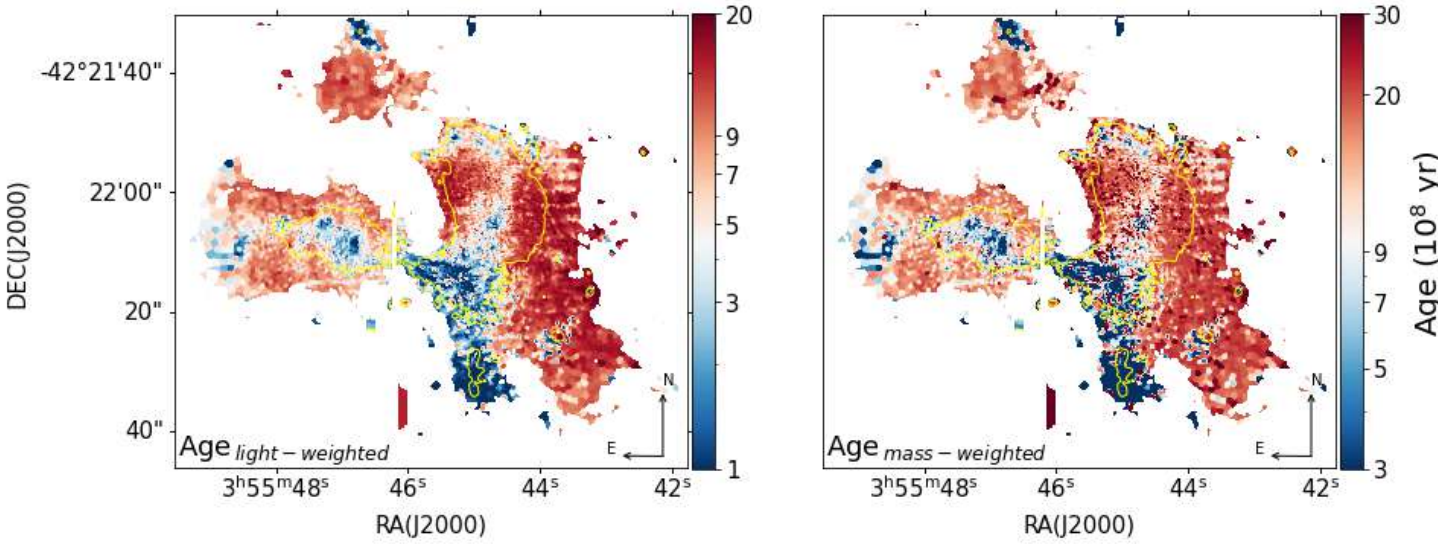

Figure 3.14: Left, Luminosity-Weighted Age. *Right,* Mass-Weighted Age from MUSE dataset of NGC 1487.

3.5 Kinematics

The kinematics of the system was extracted using the penalized pixel-fitting (pPXF) code (Cappellari and Emsellem, 2004), which consists on the modelling of the observations by a combination of spectral templates convolved with a line-of-sight velocity distribution parametrized as a Gauss-Hermite profile (see Gerhard (1993)). pPXF is thoroughly presented in Cappellari and Emsellem (2004).

We fitted each spectrum with 8 kinematic components, one stellar and 7 focused on specific nebular emission lines ($H\alpha$, $H\beta$, [OIII]λ5007, [OI]λ6300, [SII]λ6716, [SII]λ6731 and [NII]$\lambda\lambda$6548, 6583). The gas velocities are computed using a set of Gaussian emission line templates from the EMILES library (Vazdekis et al., 2016), while the stellar velocities are calculated using Simple Stellar Population (SSP) templates from Vazdekis et al. (2010), constructed with stellar spectra of the EMILES library. In Fig. 3.15 we show an example of the fitting process of pPXF for bin 1 after the Voronoi tesselation is performed.

With this analysis, we recovered the velocity field and velocity dispersion maps of each emission line and stellar component. The velocity field can provide important information regarding the gravitational support of NGC 1487, while the dispersion map can be useful to understand the turbulence on this system. Figs. 3.16 and 3.17 show the resulting maps of the systemic velocity and velocity dispersion of NGC 1487 for each of the above emission lines. In these maps, we show in the first row the velocity of the line of Hα and of the

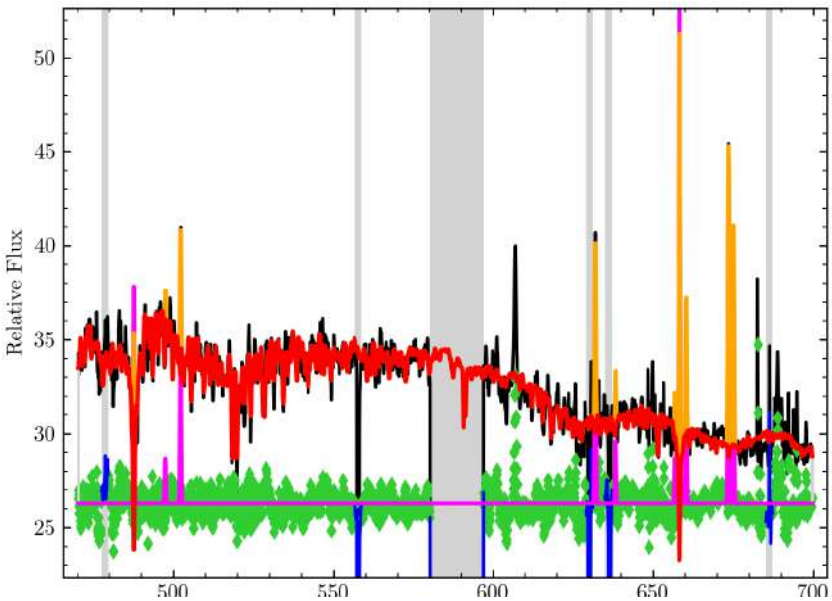

Figure 3.15: Example of the fitting process with ppxf for the MUSE observations of NGC 1487. The observed spectrum is shown by the black line, the best fit for the stellar component is shown in red, and the best fit for the emission lines is shown in the pink line. The green line shows the residual of the fit.

stars and in the subsequent panels, we compare the velocity of the other lines to Hα.

The most intriguing feature of the velocity field is in APC2. The region is almost entirely uniform, with a radial velocity ranging between ∼750 and ∼800 km/s, except in the Northern tail, where there are signs of rotation. This absence of velocity gradient could mean that the overall system is not rotating or that it is rotating but, by chance, in a face-on disk-like structure. If the system is in an active phase of merging, the stars and the gas could move in a disorderly fashion around the center of mass, thus the integrated line-of-sight profiles do not display any ordered motions. However, in that case we expect that the gaseous profiles get broader due to integration of random motions along line-of-sights. The velocity dispersion map shows that the profiles are narrower in the central regions (∼35-45 km/s) of the system than in the outskirts (∼25-30 km/s). From the combination of the velocity field and of the velocity dispersion field we conclude that APC2 is undergoing a phase of merging during which the gas, out of equilibrium, shows disordered motions. The gas disk has not yet had time to be rebuilt and that is why we do not observe large-scale ordered motions. The duration of this phase is relatively short because the gas is collisional and tends to reform a disc relatively quickly.

The velocity field of APC1 also displays an uniform velocity field with a mean velocity

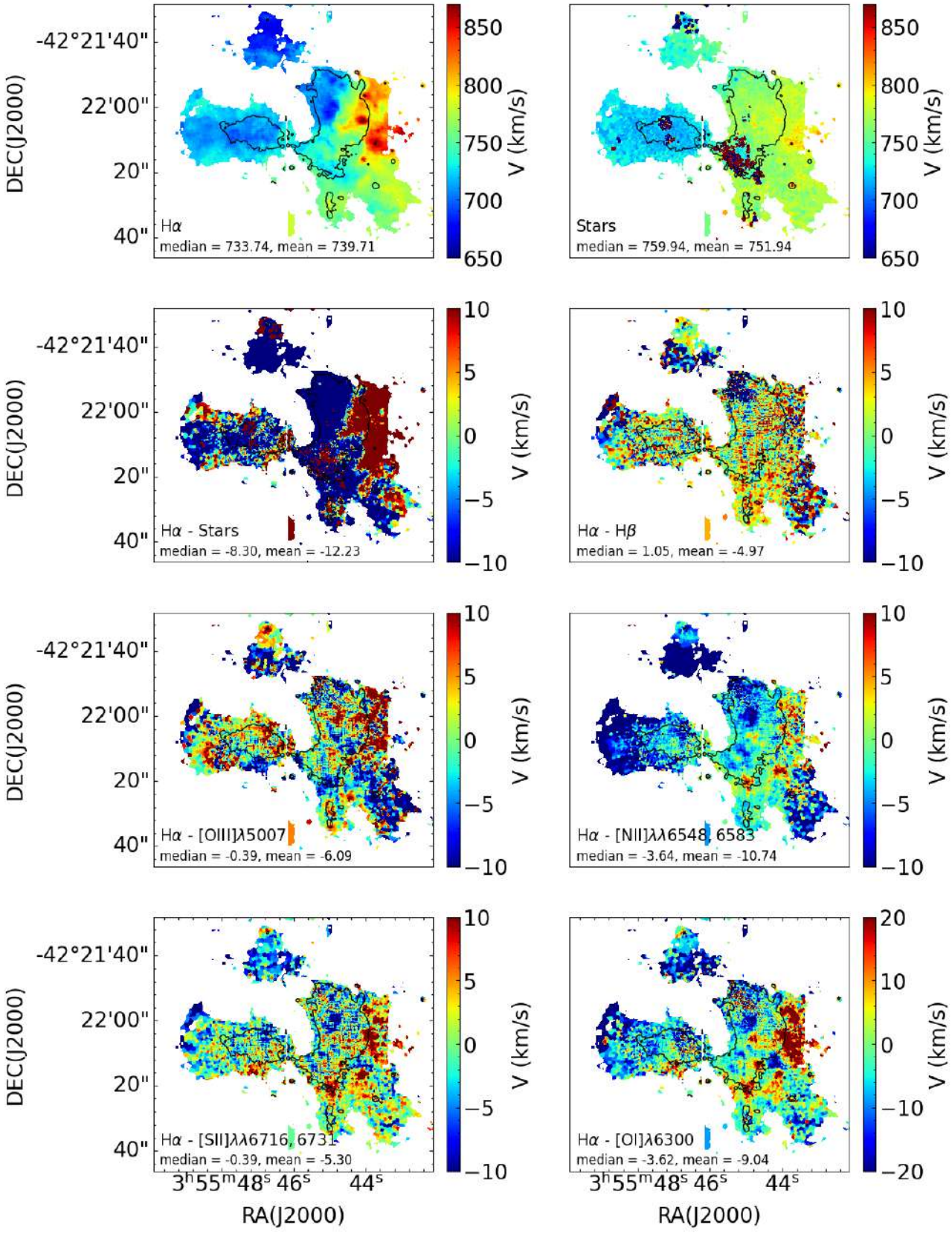

Figure 3.16: Velocity fields of NGC 1487 obtained using pPXF with 7 nebular and 1 stellar component. The first row shows the velocity of the Hα line and of the stars, and the following panels show the velocity of the stars and of the other emission lines compared to Hα. Respectively: stars, $H\beta$, [OIII]λ5007, [NII]$\lambda\lambda$6548, 6583, [SII]$\lambda\lambda$6717, 6731 and [OI]λ6300.

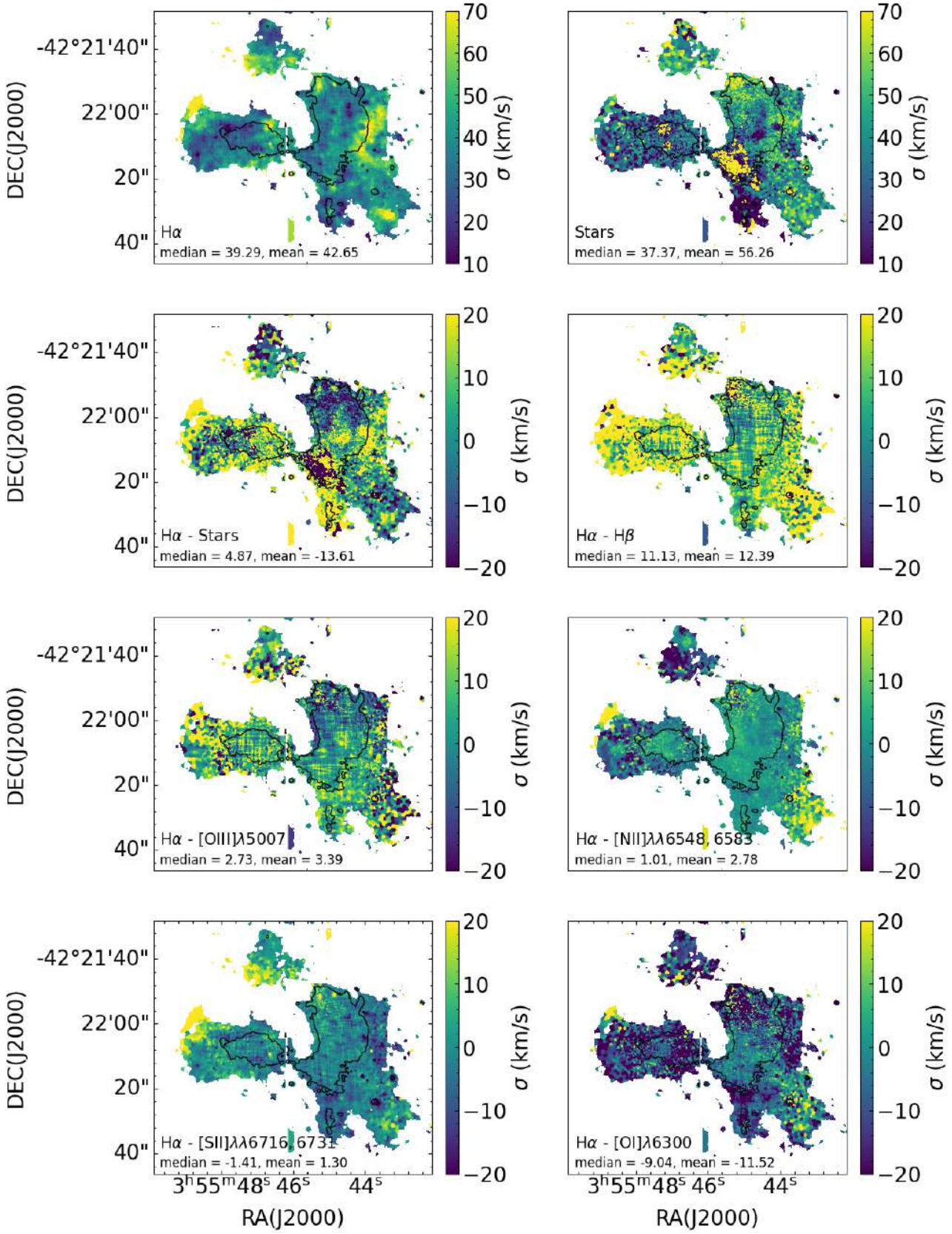

Figure 3.17: Velocity dispersion maps of NGC 1487 obtained using pPXF with 7 nebular and 1 stellar component. The first row shows the velocity of the Hα line and of the stars, and the following panels show the velocity of the stars and of the other emission lines compared to Hα. Respectively: stars, $H\beta$, [OIII]λ5007, [NII]$\lambda\lambda$6548, 6583, [SII]$\lambda\lambda$6717, 6731 and [OI]λ6300.

slightly lower than APC3 ($\sim$ 700 km/s)

From Figs. 3.16 and 3.17 we see that the amplitude of the stellar component is much lower than the nebular component, indicating either that the stars do not present any motions, or that the continuum is not enough to perform this kind of study with the MUSE dataset.

3.6 Discussion and Conclusion

3.6.1 Can the merging of the NGC 1487 system generate an S0-like galaxy?

From the formation scenarios studied in Section 1, we have seen that S0 galaxies can be the result of major merger events (Tapia et al., 2017), when and if the encounter is between two gas-rich galaxies, together with other special conditions discussed. In this type of events, in the beginning of the process, the parameters, such as magnitudes and internal velocity of S0s may deviate a lot from the Tully-Fisher relation (Tully and Fisher (1977)) of spirals and S0s, since the merger induces large disturbances in the morphology and kinematics of the system. Afterwards, the galaxy evolves passively to become an S0 as we see today, with $v/\sigma \approx 1$, where the S0s lie on the Tully-Fisher lower than the spirals because of fading.

Galaxies created in this way have usually younger stellar populations in their centers and older in their outskirts, due to infall of gas into the center of the galaxies triggered by the encounter (Bekki and Couch, 2011).

These properties seem to agree well with the observed status of NGC 1487. Due to infall of gas, the galaxy shows younger stellar populations in the center and older populations in its outskirts, but the kinematics of the system is chaotic. If this galaxy evolves passively from the current stage, reconciling the kinematics to the found observationally for S0s (Cortesi et al., 2013), this scenario seems plausible for the creation of an S0 galaxy, in the same way that studies support that other S0s observed today are the remnants of major mergers that occurred around $z \sim 0.8$ (Tapia et al. (2017)). The system could evolve to a spiral or elliptical galaxy as well, depending on the initial and current conditions of the system.

3.6.2 Morphology

NGC 1487 was studied by few works in the past years and none seem to have reached a consensus on the morphology of the galaxy. Aguero and Paolantonio (1997) suggest that the galaxy is a merger between two gas-rich galaxies. In the other hand, Bergvall et al. (2003) show, comparing optical and IR data, that the galaxy is most probably involved in a process of merger between several dwarf galaxies forming a small group, instead of the merger of two massive galaxies. This scenario would explain the low rates of SF observed today in the galaxy.

Georgakakis et al. (2000) observing NGC 1487 in radio, concluded that the galaxy is a gas-rich major merger and that the galaxy is in a pre-merger stage, where the gas is not coalescent yet.

If, in one hand, the merger between several dwarfs would explain the observed rates of SF, we would also expect to see more scattered distributions of mass, metallicity and age in the galaxy, once the galaxy is still in an earlier stages of the merger and did not have the time yet to homogeneize some of its physical properties.

On the other hand, in the velocity field, we clearly see a distinction between the velocities in the region where APC1 is located from APC2, APC3 and APC4, indicating that these may be two galaxies that merged, each with its own systemic velocity and have not reached equilibrium yet.

Based on the derived mass, velocity and age of NGC 1487, we conclude that it is unlikely that the galaxy is a result of several minor mergers, but is actually the result of the merger between two gas-rich galaxies, where the two galaxies can be identified by the differences in the velocity field in Fig. 3.16.

3.6.3 On the four bright condensations of NGC 1487

As mentioned throughout this paper, the four bright condensations APC1, APC2, APC3 and APC4 proposed by Aguero and Paolantonio (1997) have guided the majority of the results of this work. As a summary, these regions were found to host the youngest ages, highest levels of star formation, the lowest oxygen abundances and highest electron densities. These regions also revealed to be mostly ionized by star formation, with very few hints of nuclear activity. These regions also show the lowest amounts of dust, the higher

Table 3.1 - Physical properties of NGC 1487 and its four main condensations.

Physical Property	**NGC 1487**	**APC1**	**APC2**	**APC3**	**APC4**
$\sum$ f(Hα) (10^{-20} ergs/s/cm^2/Å)	1.7×10^8	2.2×10^7	6.2×10^7	4.2×10^7	1.4×10^7
Mean A_V, gas (mag)	0.006	0.103	0.128	0.111	0.048
$\sum$ L(Hα) ($L_\odot$)	1.2×10^7	1.5×10^6	4.6×10^6	2.9×10^6	8.3×10^5
Ionization Source	SF	SF	SF	SF	SF
Mean [SII]$\lambda\lambda$6716, 6731 ratio	1.46	1.46	1.46	1.44	1.45
$\sum$ SFR ($M_\odot$/yr^{-1})	0.373	0.045	0.139	0.089	0.025
Mean 12 + log(O/H)	8.33	8.30	8.33	8.29	8.27
$\sum$ $M_\star$ (10^9 $M_\odot$)	4.61 ± 1.24	0.62 ± 0.06	1.81 ± 0.36	0.25 ± 0.06	0.08 ± 0.02
Mean age (light-weighted) (Myr)	235	615	936	253	274
Mean age (mass-weighted) (Myr)	437	1147	1798	925	774

dust attenuation is actually found in the transition from APC2 to APC3. In Table 3.1 we summarize our results in function of the condensations, showing all the derived properties of NGC 1487 for each region and the system as a whole.

3.6.4 Gas-phase metallicity and metal mixing

As discussed in the introduction, theoretical studies show that major mergers may lead to the formation of bars that will, in turn, push less-enriched gas from the outskirts towards the center of the galaxies, inducing central starbursts.

In NGC 1487, we detect an overall flat oxygen abundance gradient with large depressions of low-metallicity gas in the central regions of all four condensations, which would characterize an inversion in the oxygen abundance distribution. We observe a systematic shift in the systemic velocity (Fig. 3.16) from the region of APC1 ($\sim$ 700 km/s) to the regions of APC2 and APC3 ($\sim$ 800 km/s), indicating that these may be the two massive galaxies merging (although we can only observe one galactic body nowadays). This transition supports the idea of a gas flow between the galaxies and this gas flow may be the main responsible in producing this inversion in the metallicity gradient. This is in agreement with recent simulations that show that interactions and mergers induce gas inflows towards the center of the galaxies, diluting the central abundances and producing flat metallicity gradients (Rupke et al., 2010; Perez et al., 2011).

Large field-of-view kinematic data would be the right data sources to look for such flows and explain this observed inversion in the metallicity gradient.

3.6.5 Star formation rates

The first impression when inspecting all of the previous physical properties derived for this galaxy is the large discrepancy between the emission in the optical, given by the V-band isophotes, overplotted to the images (Fig. 3.4), and the nebular emission. These seems to exist an offset between the optical emission in the Northern region of the galaxy, where the gas emission is nearly zero. In the same context, a strong star forming region is found in the lowest region of APC2, as if a shock pushed the gas towards APC3. We conclude that the merging event was responsible for suppressing or at least not encouraging star formation in the regions that dominate the optical, mainly represented by APC1 and APC2, but, at the same time, it triggered star formation in the central regions of APC3 and even created a ring-shaped star forming region in APC4.

From the SFR map we can also see that the encounter created one distinguishable tail above APC1 (NW to APC2) with high levels of star formation.

3.6.6 Ionization Source

By studying the line ratio maps sensitive to the shape of the ionizing spectrum and the BPT diagrams, we see that the majority of the spaxels fall in the star-forming region, being solely ionized by photoionizing stars.

Although studies support that merger events can induce AGN activity, this is not seen in this analysis. However, as Lee and Lee (2005) suggested, this merger is still young (approximately 500Myrs), and we can expect that AGN events may still happen, probably in the final stages of the merger.

We identified, in the BPT-SII diagram, signs of nuclear activity ionizing some spaxels of the galaxies. These spaxels are mostly in the outer-regions of the galaxies and, as studied by Belfiore et al. (2016), these type of behaviour is not generally reflecting the true ionization source of the spaxels. Galaxies that show these outer spaxels in the AGN regime of the BPT diagrams are usually called “LIERs”, for showing nuclear activity in unrealistic spots.

Belfiore et al. (2016) argues that this type of behaviour is usually reflecting other types of events, such as shocks, non-virial motions and outflows that may be playing a major role in the ionization structure of this type of systems.

Inflows and outflows are consistent with the scenario of a decreasing metallicity towards the center of the system and may be the explanation of the inverted gradient that we observed. To be able to fully understand the flows taking place, we need higher field-of-view velocity fields.

3.6.7 Ages and Mass

The study of the age distribution of the system suggests that the center of the four condensations reveal younger stellar populations than the outskirts of the galaxies, what is consistent with the higher rates of star formation in these regions. These younger populations are mostly observed in the light-weighted age map, and they show ages of around $\sim 100 - 300$ Myr, consistent with the age of the merger derived by Lee and Lee (2005) (~ 500 Myr).

The map of the mass-weighted ages, in turn, reveals the old stellar populations in the system, found mostly in the northern region of APC2 and outer-regions. The ages of these regions range from $\sim 2 - 3$ Gyr and coincide with the location of the most massive region of the system (see Fig. 3.13).

3.6.8 Kinematics

When analysing the velocity field and velocity dispersion maps of NGC 1487 we identified a rotation pattern in the region of APC2, what shows that the galaxy is rebuilding a disk. In the region of APC3, we see regions with higher velocity dispersion, what suggests that this region is undergoing a phase of merging during which the gas, out of equilibrium, shows disordered motions.

The gas disk has not yet had time to be rebuilt and that is why we do not observe large-scale ordered motions, only in the region of APC2. Moreover, the clear difference in the mean velocity of APC1 to the region with APC2, APC3 and APC4, suggesting the contours of the two merging galaxies, although the galaxies are today only one galactic body. A deeper study of the gas flows and motions in the system and two tidal tails requires 2D kinematic data over an extended area. This is currently being studied using Fabry-Perot data by Torres-Flores et al. in prep.

Chapter 4

S0 galaxies in the Southern Photometric Local Universe Survey

The spatial distribution of objects in the universe can provide us crucial information about the structure and evolution of these objects and of the universe. The identification of various morphological types of galaxies within the large-scale structure, for example, can lead us to a greater understanding of the mass build-up of galaxies, i.e. how galaxies formed and evolved in different environments over cosmic time. This is only possible, however, when dealing with large surveys, where the statistics allow for accurate determinations of high and low-density areas, as well as the galaxy populations present in each of those.

As discussed in Chapter 1, the number density of all galaxies in the nearby universe that are of types S0 or SB0 is $\sim 8\%$ in the field, 13% in groups, 15% in all clusters, and 28% in dense environments such as the Virgo cluster (van den Bergh, 2009). In this Chapter, we use observations of $\sim 20k$ galaxies from the Southern Photometric Local Universe Survey (S-PLUS) to recover photometric redshifts, physical properties and the distribution of these galaxies across the nearby universe. As part of a much broader and ongoing effort by us to supply the S-PLUS collaboration with reliable photometric redshifts, here we will use our analysis to try to identify S0-like galaxies and present a preliminary analysis of their distribution. We discuss what are the limitations and implications of applying our method for the identification of S0 galaxies, and how this method can eventually lead to the study of the evolution of this class of galaxies, in the ongoing S-PLUS project.

4.1 S-PLUS

For this work, we use data from S-PLUS, the Southern Photometric Local Universe Survey, a novel survey that will cover ~ 9300 deg^2 in twelve filters, using a robotic 0.8m-aperture telescope at the Cerro Tololo Interamerican Observatory (CTIO), Chile. The twelve filters used by S-PLUS are shown in Fig. 4.4 and include the standard SDSS-like optical bands u, g, r, i, z, and 7 narrow filters centered on common features of stars and nearby galaxies: [OII], Ca H+K, G-band, $H\delta$, Mgb, Hα, and CaT. Although there are many current and future large-area imaging surveys in the Southern Hemisphere, S-PLUS provides a unique sampling of the optical spectrum thanks to its seven narrow-band filters. The area covered by the S-PLUS survey compared to other surveys is shown in fig. 4.1.

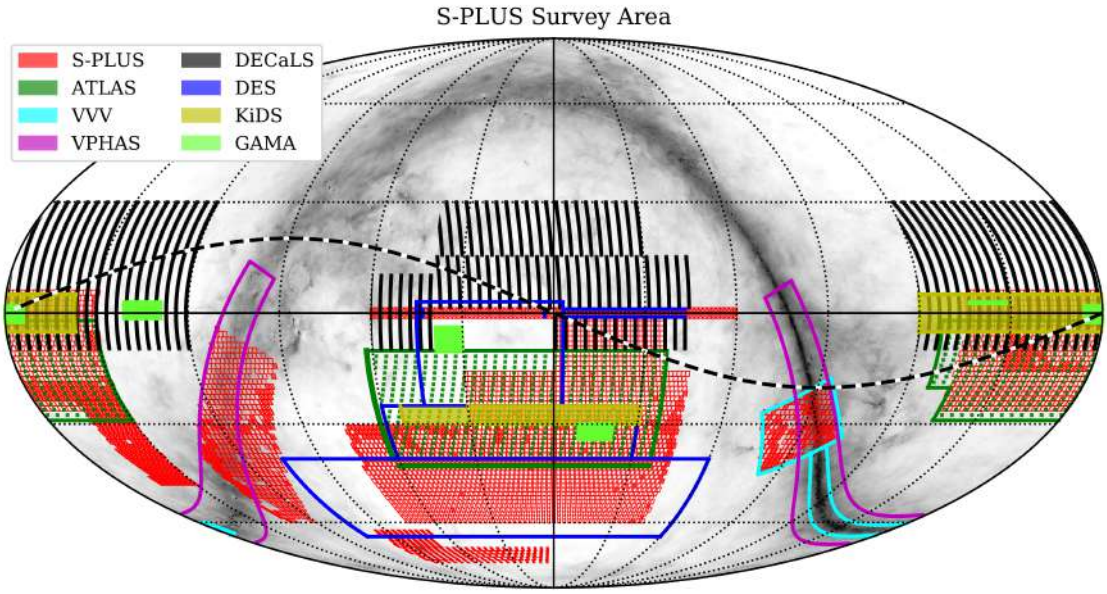

Figure 4.1: Comparison between surveys coverage. The planned S-PLUS footprint is shown in red (Mendes de Oliveira et al., 2019).

4.1.1 S-PLUS strategies

The S-PLUS survey is composed of five sub-surveys, briefly described below.

- The Main Survey: The Main Survey (MS) of S-PLUS will cover an area of ≈ 8000 deg^2 with a single epoch observation of each field, per filter, under photometric

conditions and seeing from 0.8″ to 2.0″. The MS strategy is mainly focused on extragalactic science.

- The Ultra-Short Survey: The Ultra-Short Survey (USS) has the same footprint as the MS and is motivated by the search for low-metallicity stars.

- The Variability Fields: The Variability Fields Survey (VFS) will perform repeated observations with a cadence set by the frequency of non-photometric nights, covering a number of fields already observed by the MS. The VFS is focused on the inspection of new asteroids and other moving objects, as well as some SNe may also be identified.

- The Galactic Survey: The Galactic Survey (GS) covers an area of about 1420 deg^2 in the Milky Way plane, including regions of the bulge and the disc. The main studies with these data are: (1) Variable stars: the number of observations is suitable for the detection of variable sources, including pulsating RR Lyrae and Cepheids, CVs and eclipsing binaries, as well as transient sources such as microlensing events. (2) Stellar Open Clusters: The multi-band photometry of the S-PLUS survey together with the high-precision measurements of GAIA will allow a systematic study of open clusters down to a magnitude deeper than current analyses.

- Marble Field Survey: The Marble Field Survey (MFS) is composed of a set of specific fields that will be revisited as often as possible under dark or grey nights and bad photometric conditions. Some objects that are part of the MFS are the M83 galaxy, the SMC, the Dorado Group, and the Hydra cluster. This strategy is good for nearby galaxies, galaxy groups and clusters, and their surroundings, i.e., galaxy halos, intragroup and intra-cluster light. The MFS may also be used for identification and characterisation of variable sources.

4.1.2 Data Reduction

The data reduction of the S-PLUS data is based on the pipeline jype (developed by CEFCA's Unit for Processing and Data Archiving, UPAD) designed to reduce data for the J-PLUS and the J-PAS surveys (Cristóbal-Hornillos et al. 2014). The basic four steps of this reduction are: 1) The creation of a master bias; 2) The creation of a master flat; 3)

Reducing individual frames and 4) Combine the individual frames into one astrometrically-corrected image.

The bias frames are obtained every night and are stable over a period of 30 days. Master flats are obtained for each filter, and only the flat field with counts between 8000 and 45000 are used. The master flats are created after the trimming, bias and overscan subtraction and their creation is based in obtaining, for each pixel, the median value, with 3-sigma clipping, of all usable flats of a given filter using the task IMCOMBINE in IRAF. The master flats are then normalized to have a mean of unity.

The reduction of individual images consists of applying the overscan subtraction, trimming, bias subtraction, and master flat division, as well as satellite tracks, cosmic rays and fringing are corrected. The fringing is corrected by combining the final individual frames that suffer from fringing to create a fringing frame that is stable over several months.

The combination of individual images, typically three images of each field and filter, is done by summing them up, pixel by pixel, using the code SWarp[1] (Bertin et al. 2002).

The calibration of zero-points in the S-PLUS survey based on novel photometric calibration technique (Sampedro et al. in prep) and consists in using template fitting algorithms to compute a preliminary model stellar magnitude, in each of the 12 bands, for a set of tipically one thousand stars in an S-PLUS tile that have known magnitudes. For each star, the best-fitting model is found for the literature photometric information and this best model is used to correct the S-PLUS measurements. The initial zero-points of the S-PLUS filter system are determined through convolution of the filters with the best model, and comparison between the resulting magnitudes and the instrumental magnitudes obtained for each star in the S-PLUS image. The stellar templates are from the Next Generation Spectral Library (NGSL, Heap & Lindler (2007)) and the Pickles library (Pickles 1998).

Once the initial zero-point values have been derived for the S-PLUS filter system, the process is iterated by fitting again the stellar models, but now to the newly derived 12- band photometry for each object. This is done for a few iterations, until reaching convergence to a final solution for the zero-points in every filter. All zero-points are then absolute-calibrated to match Gaia's photometry (Arenou et al. 2017).

The calibrated data are then used to generate the Photometric Catalogues of S-PLUS. These final catalogues include the coordinates, photometry and errors, and morphological

[1] `https://www.astromatic.net/software/swarp`

parameters (e.g., ellipticity, position angles, major and minor axis ratio, and stellarity) of each source in the S-PLUS images.

4.1.3 Photometric Depth

The photometric depth of the S-PLUS images is shown in table 4.1. These depths were calculated using five different definitions of magnitudes in a given filter with a signal-to-noise ratio ≥ 3.

Filter	m_{peak}	$m_{50\%}$	$m_{80\%}$	$m_{95\%}$	m_{3arcs}
u	21.07	22.10	23.11	24.12	22.56
J0378	20.64	21.83	22.86	23.88	22.27
J0395	20.11	21.47	22.52	23.65	21.87
J0410	20.30	21.53	22.57	23.67	21.94
J0430	20.38	21.54	22.59	23.67	21.94
g	21.79	21.88	22.85	23.88	22.16
J0515	20.61	21.33	22.42	23.53	21.64
r	21.63	21.12	22.07	22.88	21.32
J0660	21.36	21.02	21.98	22.93	21.12
i	21.22	20.54	21.41	22.07	20.72
J0861	20.32	20.23	21.29	22.36	20.39
z	20.64	20.27	21.05	21.77	20.37

Table 4.1 - Photometric Depth of S-PLUS data.

Where, m_{peak} is the Petrosian magnitude, $m_{50\%}$, $m_{80\%}$ and $m_{95\%}$ are the magnitudes that include 50%, 80%, and 95% of the total detected sources and m_{3arcs} corresponds to the integrated magnitude within circular apertures of 3 arc-second diameter. To summarize, the S-PLUS images are expected to be complete down to a magnitude $g < 21.62$ and $r < 21.38$ for all sources (point and extended) with a $S/N > 3$.

4.2 Data used for this work

From S-PLUS Data Release 1 we use a sample of 17500 galaxies with reliable spectroscopic redshifts to determine photometric redshifts.

4.2.1 The spectroscopic control sample

To evaluate the accuracy of the photometric redshift determination, we have compared our results with a sample of spectroscopic redshifts from SDSS (Szalay, 1999), 2dF (Hawkins et al., 2003) and BOSS (Dawson et al., 2013) surveys. This work will be extended in the future for the whole sample of galaxies and quasars of Data Release 1 and 2 of S-PLUS.

The spectroscopic sample selection is thoroughly described in Molino et al. (2019) and the comparison between the main properties of the objects can be seen in Fig. 4.2. We consider that the spectroscopic sample utilized for this work can be considered as representative in colour, magnitude, redshift and spectral-types, for the entire universe with S-PLUS observations. Therefore, the characterization of the photometric redshift performance can be considered as a good estimate of the performance of the entire survey.

4.3 Photometric redshifts

One of the most important observables to measure the distance to an object is its spectral energy distribution (hereafter SED), which is composed of a continuum together with a series of emission and/or absorption lines. The expansion of the Universe causes SEDs to shift to the red, analogous to the Doppler Effect, but for light instead of sound. This expansion stretches the SED towards longer wavelengths by a factor $1 + z$, with z being the redshift. The contrary effect, known as *blueshift*, where the SED is compressed toward smaller wavelengths, is also possible due to local motions of galaxies. This is, however, only possible in regions where the gravitational attraction surpassed the expansion of the universe, giving objects a peculiar velocity component in the direction of the observer. This is the case of the Milky Way, as seen from Andromeda, and vice-versa, for example. However, this occurs only on relatively small scales, inside groups, clusters and superclusters.

The observational difficulty in the determination of galaxies' distances consists in identifying characteristic features in the SEDs and measuring how far stretched they are. The measured redshift is directly related to a proper distance, although it depends on the adopted cosmological model.

There are several methods to estimate photometric redshifts. These methods are mainly sub-divided in two:

1. Physically Motivated Methods (Template Fitting): In this branch, the mapping

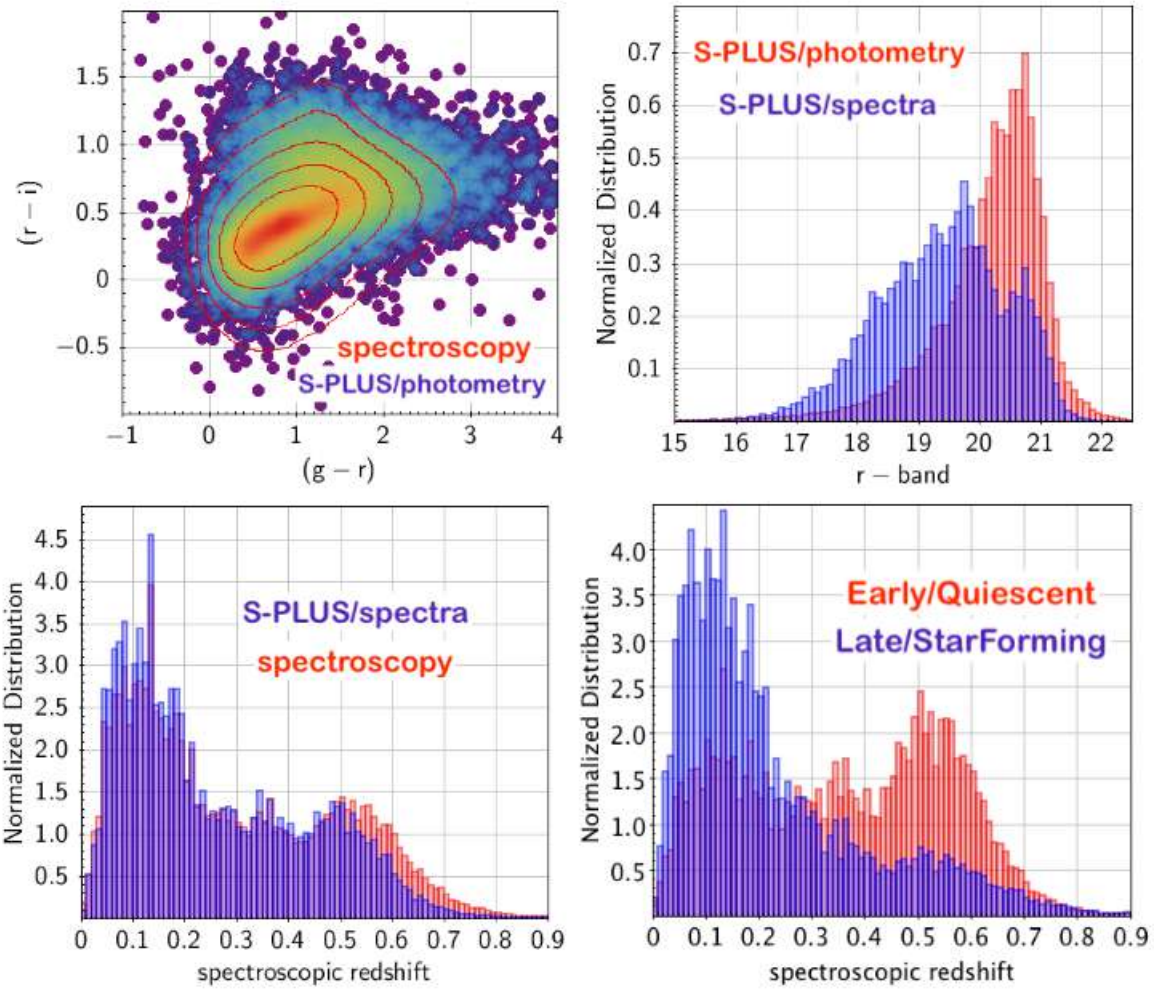

Figure 4.2: Validation of the spectroscopic redshift sample. *Top-left:* comparison of the colour-colour distribution for spectroscopic control sample (contours) and the photometry obtained with S-PLUS (dots). *Top-right:* Magnitude distribution of galaxies in the spectroscopic (blue) and photometric (red) samples. *Bottom-left:* Redshift distribution of both samples. Red histogram shows the galaxies with spectroscopic redshift in the S-PLUS footprint. Blue histogram represents the fraction of those galaxies detected in the S-PLUS observations. *Bottom-right:* Spectral-type distribution of galaxies as a function of redshift. Image taken from Molino et al. (2019)

between flux and redshift is predicted using a series of physical processes regulating the observed light emission. The most basic ingredient is the definition of a set of SED templates, which could be either empirical or theoretical. Not only the type of template determines the quality of the photometric redshifts, but also how they cover the colour-redshift and colour-colour space (further discussed in Fig. 4.6).

2. Data-Driven Methods (Machine Learning): Machine Learning algorithms can be categorised into unsupervised and supervised learning, the difference being that unsupervised learning requires only photometry, while supervised methods require both

photometry and spectroscopic redshifts for a data sample during the training of the algorithm. In the photo-z framework, these training samples allow the algorithm to learn the mapping between colour and redshift space.

A comparison of the photo-z determination methods is shown in Fig. 4.3

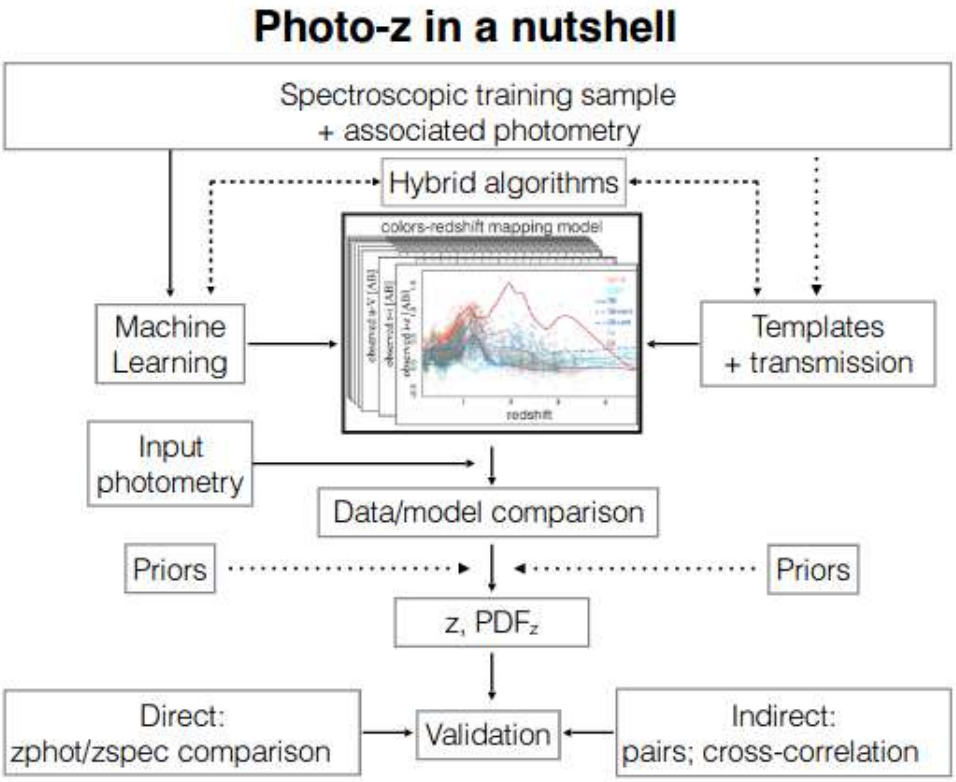

Figure 4.3: Photometric Redshift techniques. This flowchart represents the different steps in photo-z determinations. The core of machine learning, template-fitting techniques and hybrid techniques and their way to map the relation between colour and redshift. Image taken from (Salvato et al., 2018)

For this work, we focus on the template fitting technique to retrieve not only the redshifts of the galaxies, but also their spectral types and physical properties for a detailed study of the S0s among the objects studied. We used LePHARE (Le Photometric Analysis for Redsfhift Estimations) routine (Ilbert et al., 2006) to perform the fit.

4.4 LePhare

Photometric redshifts were derived using LePhare, a template fitting code based on a χ^2 minimization and described in Arnouts et al. (1999, 2002). In the basic setup, the

observed colours are matched with a set of spectral energy distribution (SED) templates, where these SEDs are redshifted in steps of 0.01 and convolved with the filter set of the instrument. The χ^2 minimization method is defined by:

$$\chi^2(z,T,A) = \sum_{f=1}^{N_f} \left(\frac{F^f_{obs} \times F^f_{pred}(z,T)}{\sigma^f_{obs}} \right)^2 , \tag{4.1}$$

where $F^f_{pred}(T,z)$ is the flux predicted for a template T at redshift z. F^f_{obs} is the observed flux and σ^f_{obs} is the error. f stands for the filter and N_f is the number of the filter. Photometric redshifts are determined minimizing χ^2 by varying the three free parameters z, T and the normalisation factor A.

4.4.1 Templates

4.4.1.1 COSMOS

The primary templates used for this analysis are composed of a set of SEDs derived by the COSMOS survey collaboration (Scoville et al., 2007). This SED set includes 19 galaxy templates derived by Polletta et al. (2007) with the code GRASIL (Silva et al., 1998), which goes from UV-optical to MID-IR. Specifically, these 19 galaxy templates are 7 SEDs of elliptical galaxies, 11 spiral galaxies (2 Sa, 2 Sb, 3 Sc, 3 Sd and 1 Sdm) and 1 S0 galaxy. To complement these templates, 12 starburst SEDs were generated using Bruzual and Charlot (2003) models. Fig. 4.4 shows the full library of SED templates used in our analysis already matched with the filter system of S-PLUS.

Together with this set of templates, we have used 4 interstellar extinction laws, one based on the Small Magelanic Cloud (Prevot et al. (1984)) and three from Calzetti et al. (2000), one of them being the most-used Calzetti extinction law for low-redshift star-forming galaxies and two others accounting for possible bumps in the spectra, including the UV bump at 2175 Å. We allow for reddenings of $E(B-V) = 0.0, 0.05, 0.1, 0.15, 0.2, 0.25, 0.3,$ 0.4 and 0.5 mag.

These templates are in units of F_λ. Therefore, to obtain the AB magnitudes from the flux, we used:

$$m_{AB} = -2.5 \log f_\nu - 48.6, \tag{4.2}$$

where

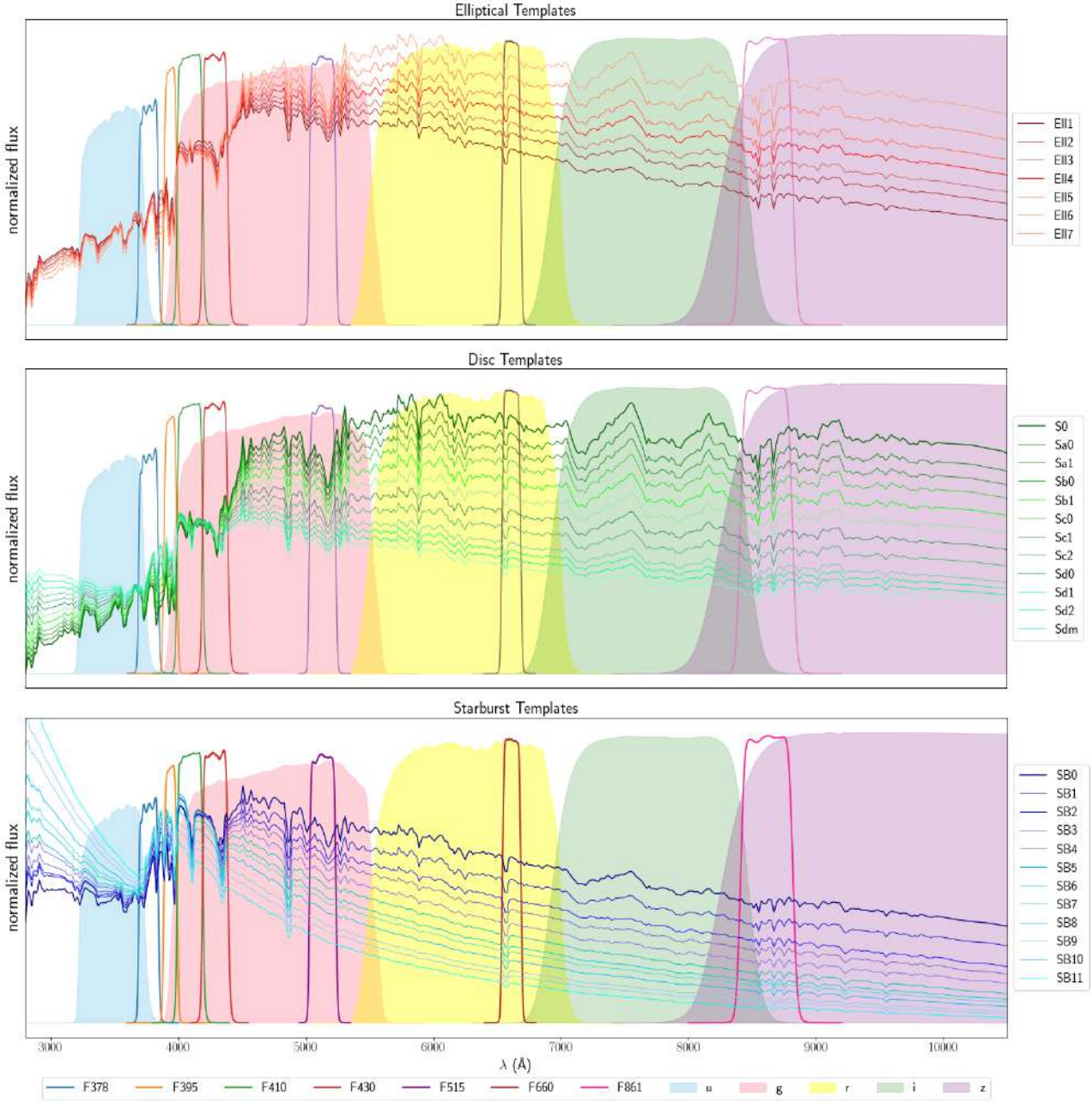

Figure 4.4: Galaxy SED templates

$$f_\nu = \frac{1}{c} \frac{\int F_{\lambda,int}\, T_\lambda\, \lambda\, d\lambda}{\int T_\lambda / \lambda\, d\lambda}, \tag{4.3}$$

where $F_{\lambda,int}$ is the flux at wavelength λ of the template, T_λ is the filter system, λ is the wavelength and c is the speed of light.

If one includes the extinction, the template $F_{\lambda,int}$ becomes $F_{\lambda,obs}$, defined as:

$$F_{\lambda,obs} = F_{\lambda,int} \times 10^{-0.4 \cdot k(\lambda)\, E(B-V)} \tag{4.4}$$

where $E(B-V)$ stands for the colour excess and $k(\lambda)$ correspond to the extinction law used. In this work, we use four different extinction laws, each with 9 different $E(B-V)$, shown in Table 4.2.

Galaxy Class	**Extinction Law**	**E(B-V)**
Elliptical	– –	– –
Bulge-dominated Disc	– –	– –
Disc	Prevot et al. (1984)	0.0, 0.05, 0.1, 0.15, 0.2, 0.25, 0.3, 0.4, 0.5
Starburst	Prevot et al. (1984), Calzetti et al. (2000), Calzetti bump1, Calzetti bump2	0.0, 0.05, 0.1, 0.15, 0.2, 0.25, 0.3, 0.4, 0.5

Table 4.2 - Extinction Law and Colour Excess used in LePHARE for each galaxy type.

The previously mentioned extinction laws were applied to the disc galaxies (not bulge-dominated) and starbursts (see Table 4.2).

Using Equation 4.3, we determined the coverage of our templates in the colour-redshift space to understand if the chosen templates are capable of fitting the observed galaxies detected in S-PLUS (See Fig. 4.5).

Besides the analysis of the coverage of the SEDs in colour-redshift space, we have also analysed their coverage in colour-colour space, as shown in Fig. 4.6

From Figs. 4.5 and 4.6, we can see that the S-PLUS data are well matched to the templates in the (g-r) and (r-i) versus redshift space and in all the colour-colour spaces. The sources that lie outside the coverage of any template correspond to only 1% of the total number of sources, so we consider that our templates are representative. The addition of emission lines, new templates, colour excesses and extinction laws should be able to cover all the missing points and will be done in the future.

4.4.1.2 BC03

The photometric redshift determinations were also done using the Bruzual and Charlot (2003) templates. One major benefit of the template fitting method using theoretical templates such as these ones, is that they provide additional information, besides the redshift, such as physical properties of the objects as a built-in part of the process (e.g. stellar mass, age, metallicity). For further details, see section 2.4.2

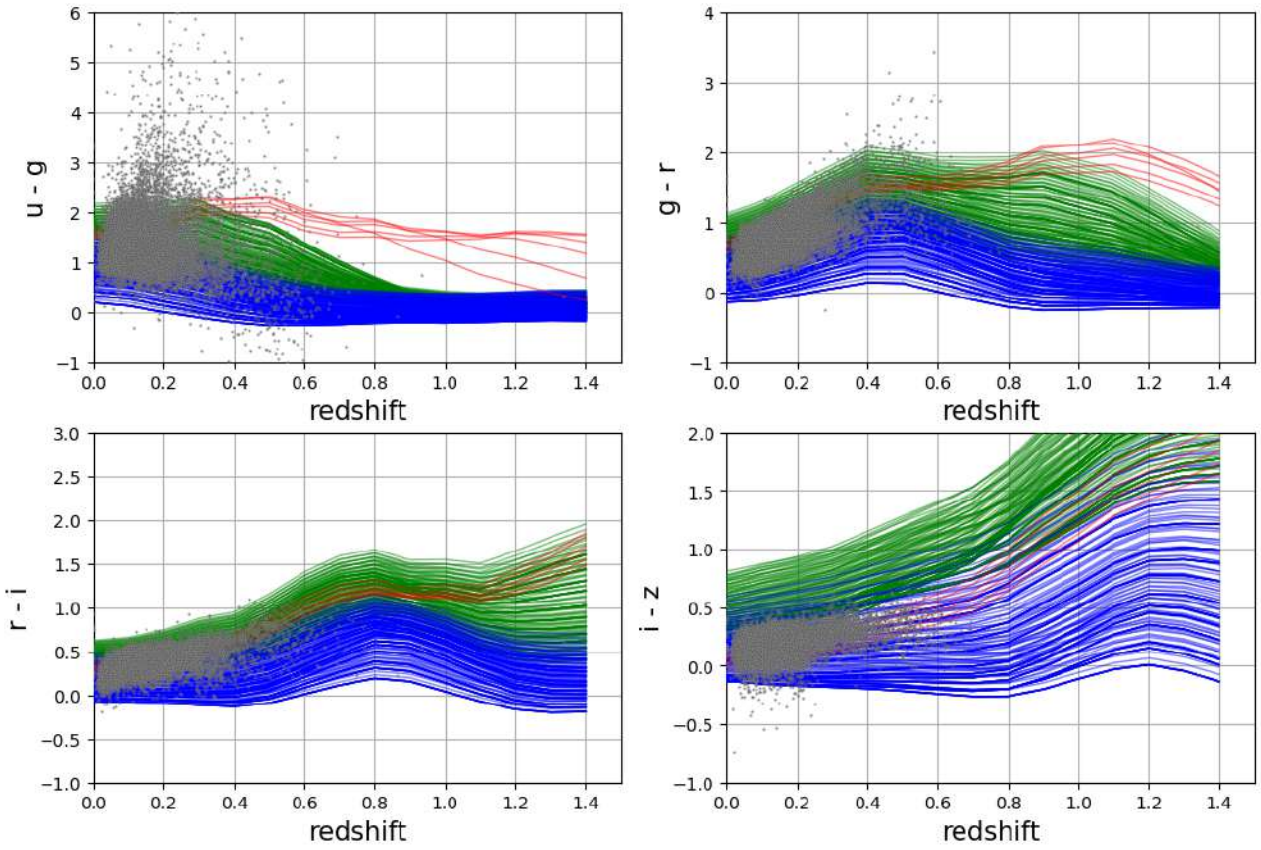

Figure 4.5: Template coverage in the colour-redshift space of the COSMOS SED templates. The orange points are our sample of galaxies observed with the S-PLUS survey. The red, green and blue lines represent the elliptical, disc and starburst templates, respectively.

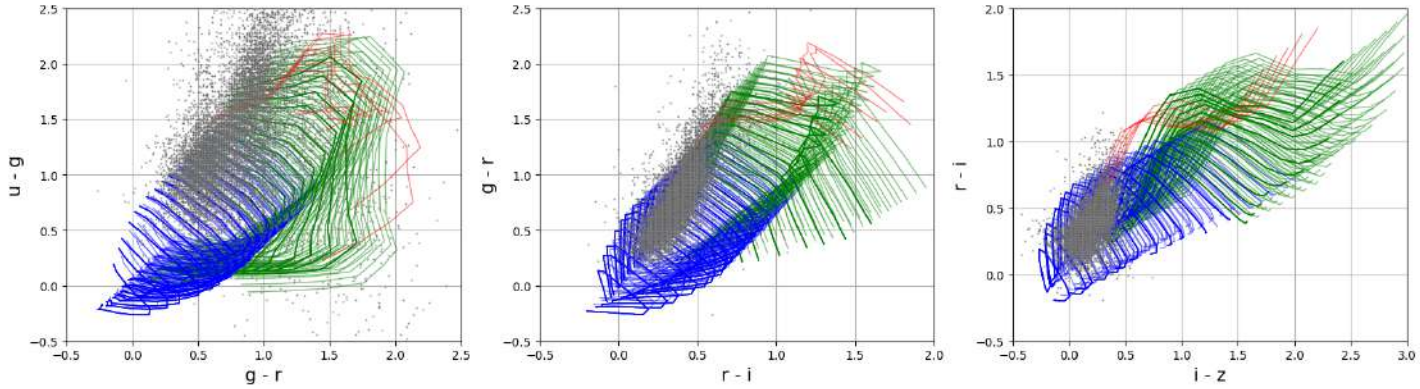

Figure 4.6: Template coverage in the colour-colour space of the COSMOS SED templates. The orange points are the colours from our sample of galaxies observed with the S-PLUS survey. The red, green and blue lines represent the elliptical, disc and starburst templates, respectively.

4.4.2 Systematic Offsets

As discussed in the previous section, LePHARE estimations are only meaningful if the colour-redshift relation predicted from the templates is a good representation of the ob-

Filter	$\lambda_{eff}()$	**median(offsets) (mag)**	$\sigma_{\textbf{offsets}}$ **(mag)**
uJAVA	3574	0.074	0.055
F378	3771	0.039	0.043
F395	3941	0.046	0.062
F410	4094	0.032	0.043
F430	4292	0.033	0.039
gSDSS	4756	0.022	0.017
F515	5133	0.027	0.025
rSDSS	6260	0.017	0.014
F660	6614	0.014	0.018
iSDSS	7692	0.023	0.013
F861	8611	0.0095	0.023
zSDSS	8783	0.015	0.012

Table 4.3 - Systematic Offsets LePHARE

served colour-redshift relation. However, uncertainties in the zero-points of any of the 12 S-PLUS bands could lead to systematic shifts between the predicted and observed colours in the colour-redshift and colour-colour relations. A correction for systematic offsets can be obtained by using a sample of galaxies with reliable spectroscopic redshifts in LePHARE, where the redshift estimations are fixed to the spectroscopic redshift and the best-fit template is determined for each of them. If there are no systematic offsets, the observed and predicted fluxes should be the same; however, this is not always observed. These offsets are caused by (1) uncertainties in the absolute calibration of the photometric zero-points and (2) uncertainties in the color modelling (filter transmission curves, incomplete set of templates, incorrect extinction curve, and so on). The systematic offsets are then computed and saved, to then be applied to the whole sample of galaxies for correction before fitting them with the whole template set. The values converge after three iterations and since each tile of the S-PLUS footprint can have different zero-points, the fit was performed for each tile separately. The average offset within the tiles for each band of S-PLUS is shown in Table 4.3 and Fig. 4.7

Our template fitting technique suggests zero-point offsets of $0.01 - 0.07$ mag.

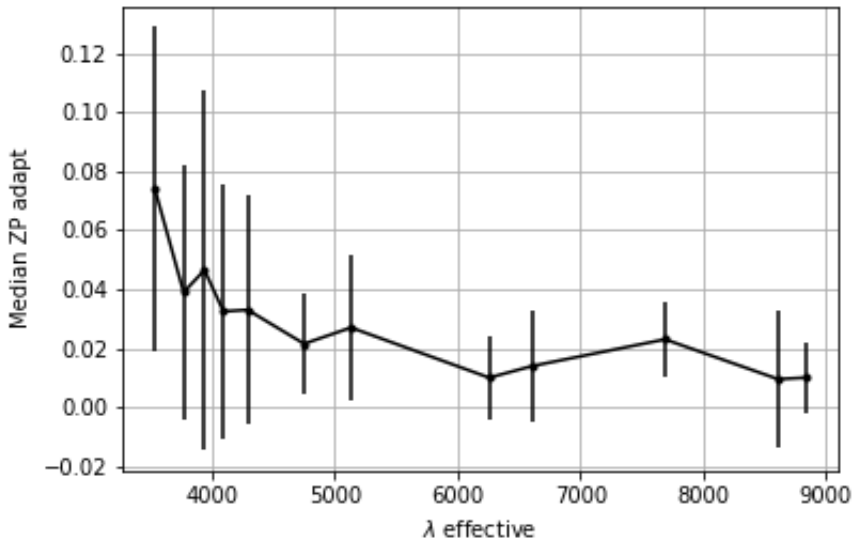

Figure 4.7: Systematic Offsets in the photometric zero-points retrieved for each band, averaged over all tiles of S-PLUS.

4.4.3 Bayesian Approach

Using the *NZPRIOR* function of LePHARE, we inserted relevant a priori information to the analyses. The mathematical formalism of this bayesian approach can be found in Benítez (2000). Following the formalism developed by Benítez (2000), we introduce the prior:

$$p(z, T|i'_{AB}) = p(T|i'_{AB})p(z|T, i'_{AB}), \tag{4.5}$$

with $p(z|T, I'_{AB})$ being the redshift distribution and $p(T|i'_{AB})$ the probability to observe a galaxy with the spectral type T. $p(z|T'_{AB})$ is parametrised as:

$$p(z|T, i'_{AB}) \propto z^{\alpha t} \exp\left(-\left[\frac{z}{z_{0t} + k_{mt}(i'_{AB} - 20)}\right]^{\alpha t}\right), \tag{4.6}$$

and $p(T|i'_{AB})$ as:

$$p(T|i'_{AB}) \propto f_t e^{-k_t(i'_{AB} - 20)}. \tag{4.7}$$

The subscript t denotes the spectral type dependency. Using this formalism, the values of the free parameters are recomputed using the spectroscopic sample, where α_t, z_{0t} and k_{mt} are set in order to maximize the likelihood of "observing"the spectroscopic sample.

Following Bayes Theorem, $p(z, T|i'_{AB})$ is a prior probability function that represents our previous knowledge of the redshift and spectral type distributions of the sample in the analysis.

In LePHARE, using the $g - r$ S-PLUS restframe color and the magnitude of the g band we achieved a significant minimization of the outlier fraction, and therefore it is the prior that we used for this work. Using both the magnitude and restframe colour allows for a compromise between the colour of the object and its distance.

4.5 Results: photometric redshift accuracy

In this work, we use the same statistical analysis as described in Molino et al. (2019). To analyse the accuracy of our photometric redshifts, we use four quantities:

1. Redshift offset:

$$\delta_z = z_{\rm phot} - z_{\rm spec}. \tag{4.8}$$

2. Scatter:

$$\sigma_{\rm NMAD} = 1.48 \times {\rm median}\left(\frac{\delta_z - {\rm median}(\delta_z)}{1 + z_{spec}}\right). \tag{4.9}$$

3. Median redshift bias:

$$\mu = \bar{\delta_z}. \tag{4.10}$$

4. Outlier fraction:

$$\eta = \frac{|\delta_z|}{1 + z_{\rm spec}} > 0.15. \tag{4.11}$$

Fig. 4.8 shows the comparison between the photometric redshift estimates using the COSMOS and BC03 templates in LePHARE against other methods of photo-z estimations using the statistics defined above. We compare the photo-z precision using template-fitting (LePhare, BPZ) and machine learning techniques (ANNz2 and GPz and deep-learning (API Keras) (MSc thesis of Vinicius-Lima (2019)).

Among the compared methods, we highlight the precision of our method in comparison with BPZ (Bayesian Photo-z Estimator) and the application programming interface KERAS using deep learning techniques. While the $\sigma_{\rm NMAD}$ of both template-fitting methods (BPZ and LePHARE with COSMOS template) is almost the same, with variations of

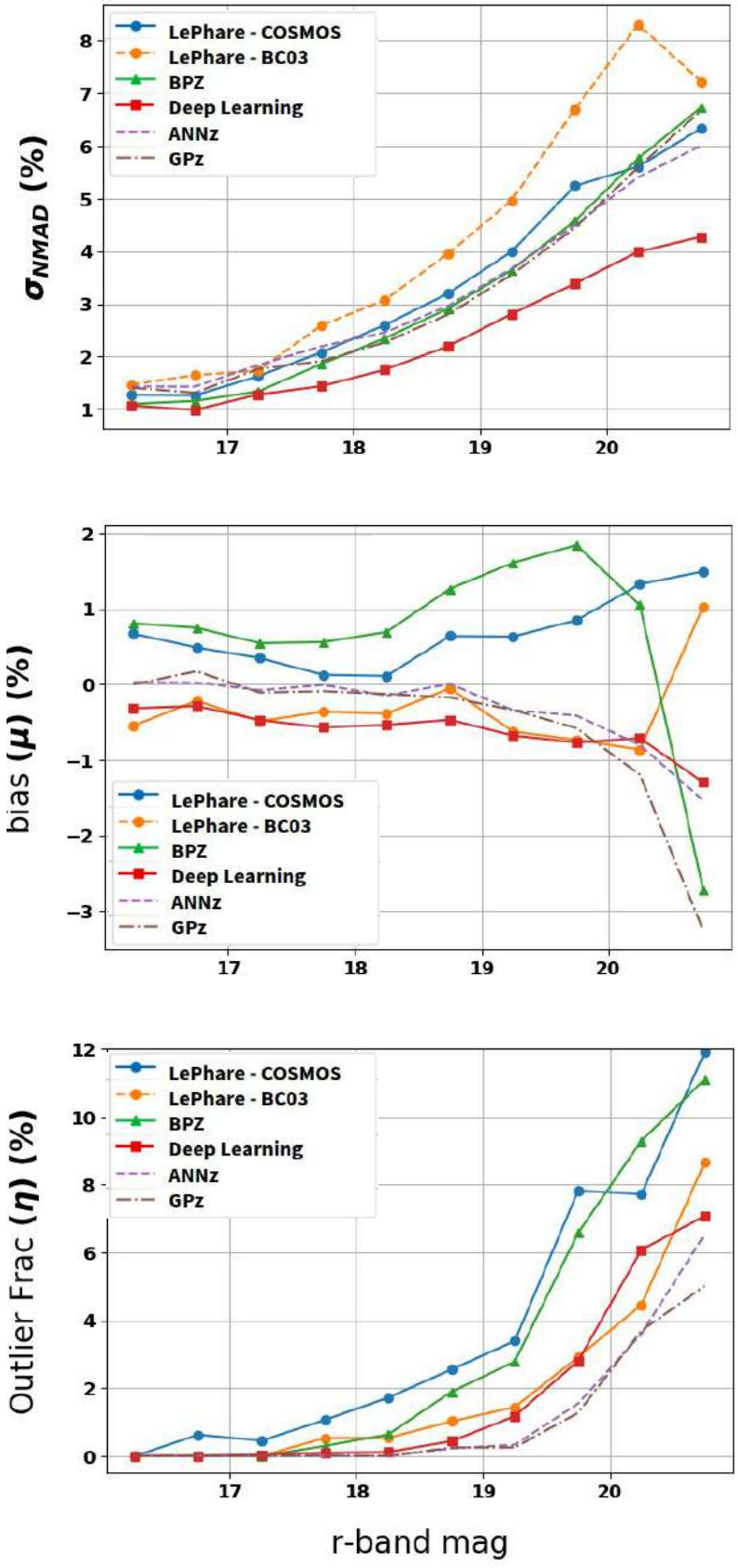

Figure 4.8: Statistics to evaluate the accuracy of the photometric redshift estimates with LePHARE using COSMOS and BC03 templates.

0.03% at most, when we analyse the bias, LePHARE shows a better agreement with $z_{\rm spec}$ than BPZ. The outlier fraction of BPZ is better than LePHARE and it will be improved (Buzzo et al. in prep).

When comparing with Keras, LePHARE has worse performance. However, although Keras performs better at the $0.5-1.5\%$ level for $r > 18$ mag, it requires a training sample and does not provide physical properties.

The performance of LePHARE using the BC03 templates will be discussed in the next section, but it important to mention already that there are great advantages in using BC03 templates, although in our current configuration, its performance is worse compared to when using the COSMOS template SEDs.

The variation between the photometric and spectroscopic redshifts using the COSMOS templates in LePHARE for galaxies with $r < 17$, $r < 19$ and $r < 21.3$ is shown in Figs. 4.9, 4.10 and 4.11

For magnitude limits of $r < 17$, $r < 19$ and $r < 22$ mag, we achieve a precision of 1%, 2% and 3%, respectively, using the COSMOS SEDs, compatible with the literature and the results obtained using the Bayesian Photometric Redshift estimator (BPZ2), described in Molino et al. (2019) (see Tab. 4.4).

Magnitude	**Method**	σ_{NMAD} (%)	μ (%)	η (%)
$r < 17$	LePhare	1.27	0.55	4.15
	BPz	1.15	0.74	3.73
$r < 19$	LePhare	2.39	0.34	3.21
	BPz	2.15	0.82	2.35
$r < 22$	LePhare	3.21	0.57	3.36
	BPz	2.9	1.05	2.95

Table 4.4 - Comparison of the statistics to evaluate the photo-z determinations using LePHARE and BPZ

4.5.1 Physical Properties of Galaxies using BC03 templates

Using BC03 templates, although we lose precision, as discussed in the previous section and shown in Fig. 4.8, we gain a lot of information about the physical properties of the galaxies. For our sample of galaxies, we have retrieved age, star formation rate, specific star formation rate and mass for the galaxies studied. These distributions are shown in

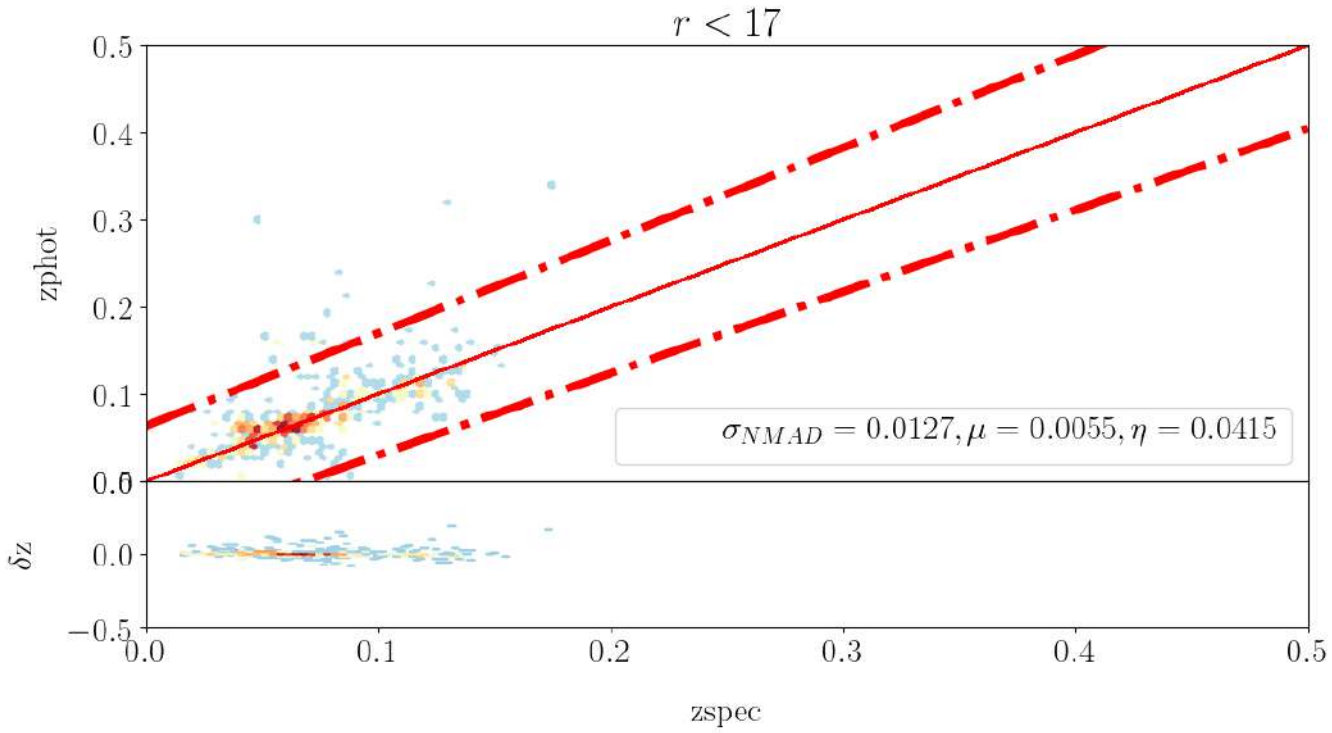

Figure 4.9: Comparison between the z_{phot} and z_{spec} for LePHARE determinations using the COSMOS templates for galaxies with $r < 17$.

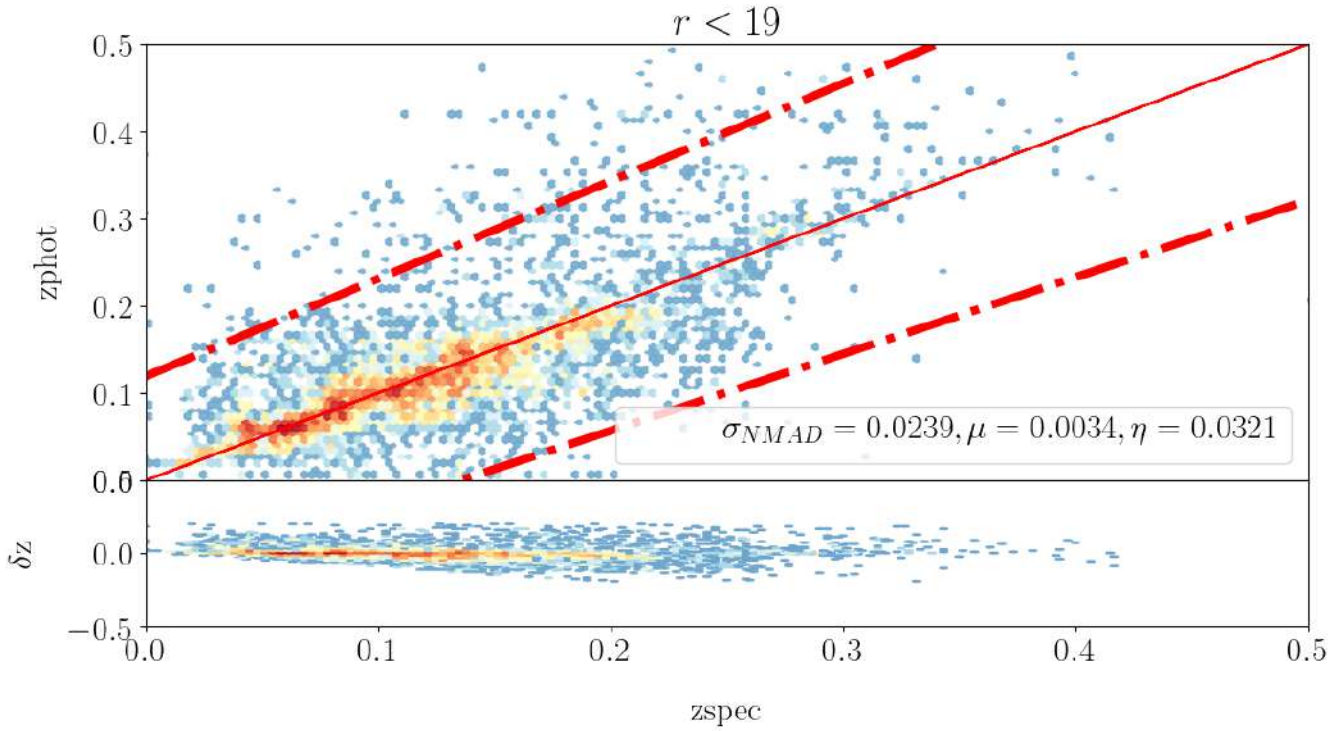

Figure 4.10: Comparison between the z_{phot} and z_{spec} for LePHARE determinations using the COSMOS templates for galaxies with $r < 19$.

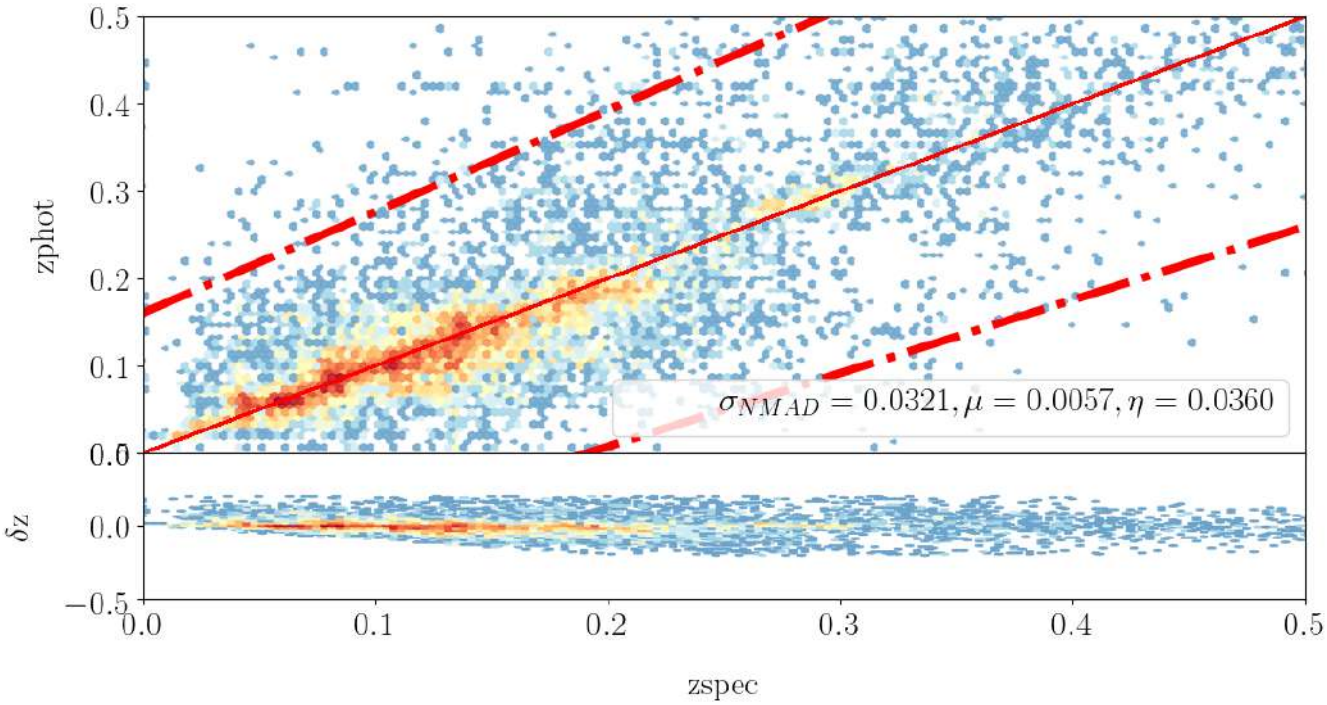

Figure 4.11: Comparison between the z_{phot} and z_{spec} for LePHARE determinations using the COSMOS templates for galaxies with $r < 21.3$.

Figs. 4.12, 4.13, 4.14 and 4.15.

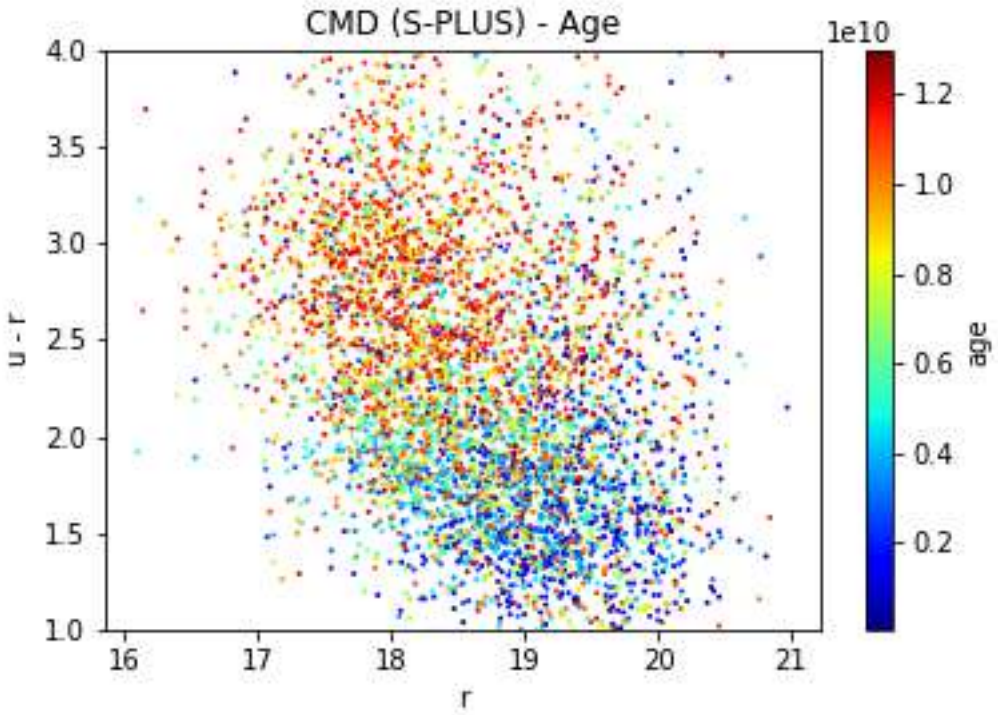

Figure 4.12: Age distribution (in years) of galaxies in our sample fitted with BC03 models across the color-magnitude diagram.

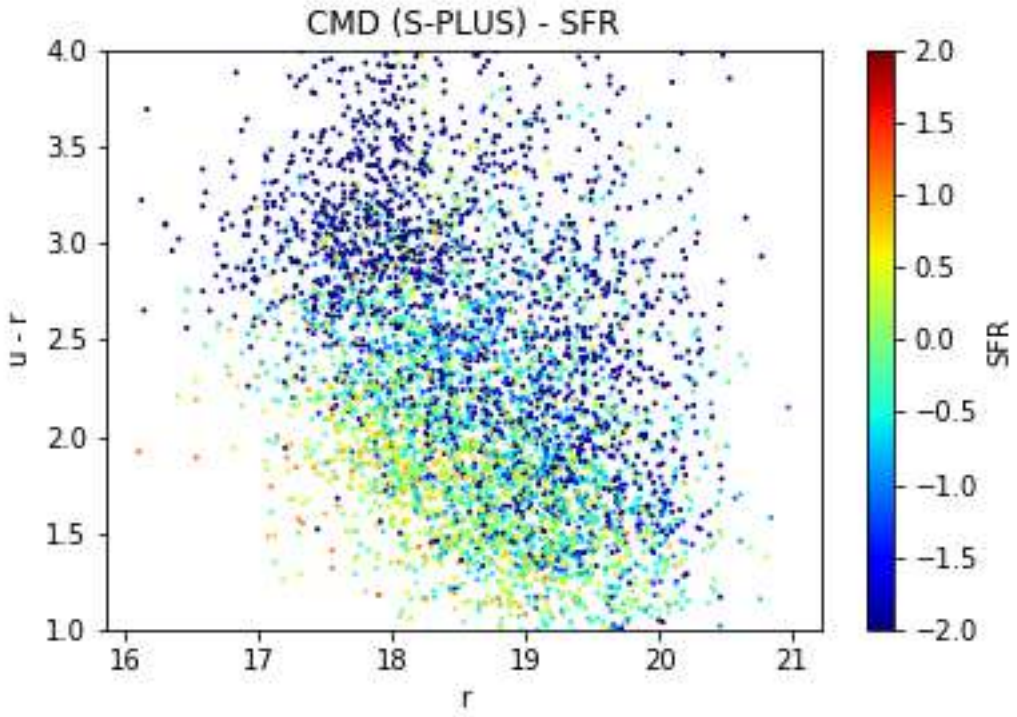

Figure 4.13: Star formation rate (in $M_{\odot}/yr$) distribution of galaxies in our sample fitted with BC03 models across the CMD.

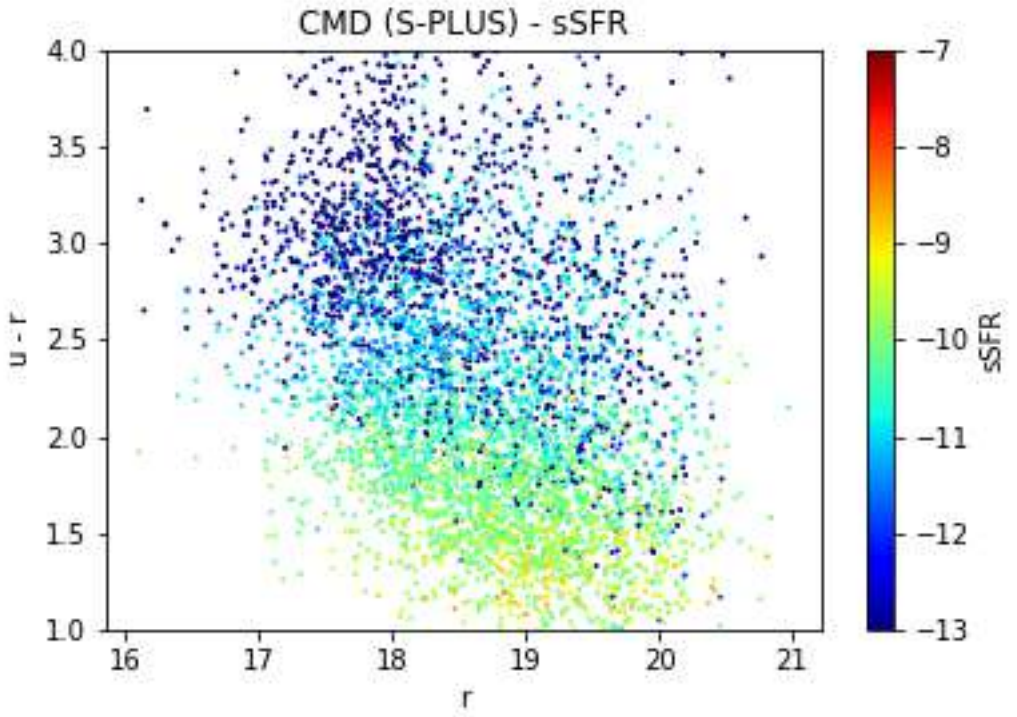

Figure 4.14: Specific star formation rate (in yr^{-1}) distribution of galaxies in our sample fitted with BC03 models across the color-magnitude diagram.

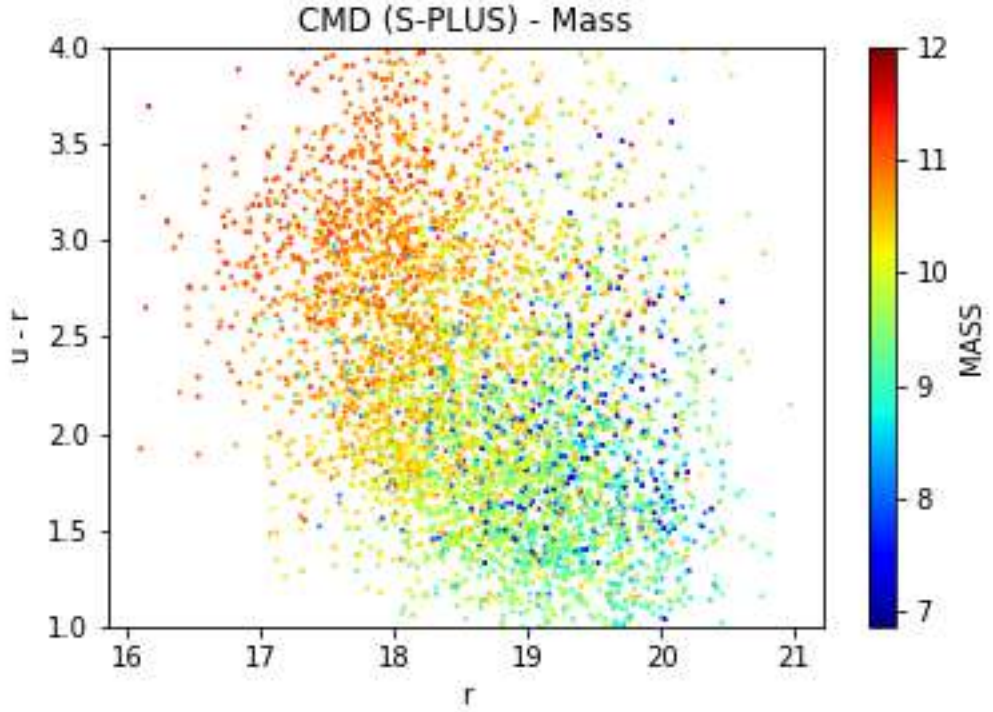

Figure 4.15: Mass distribution (in $\log(M/M\odot)$) of galaxies in our sample fitted with BC03 models

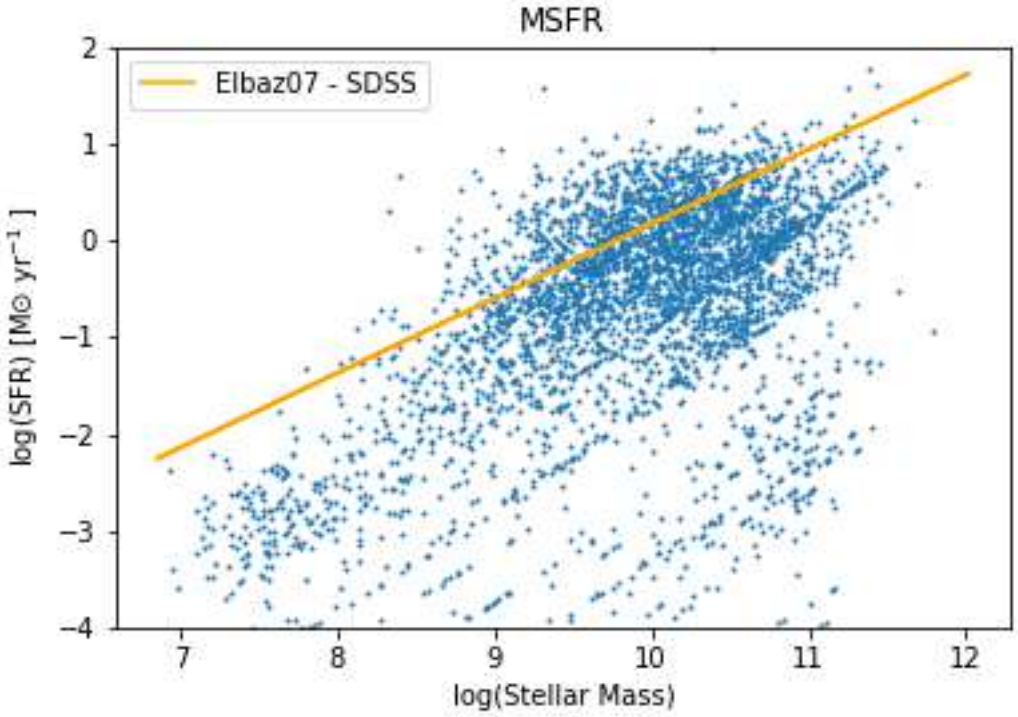

Figure 4.16: Mass-Star Formation Relation for galaxies in our sample fitted with BC03 models. The orange line shows the star-formation "main sequence" from Elbaz et al. (2007).

Depending on the scientific application, the use of BC03 templates is highly advantageous, given to the wide range of information we can retrieve of the objects using this set of SEDs. Analysing the previous plots, we can see that we can clearly retrieve the Blue Cloud, Green Valley and Red Sequence in the diagrams of mass and age, as well as differentiate starbursts of passive galaxies in the SFR and sSFR plots. Moreover, the distribution of objects in the $M_\star$-SFR space agrees well with the relation derived by Elbaz et al. (2007) for SDSS galaxies.

We conclude that, using LePHARE, and more specifically, using BC03 templates, we are able to retrieve reliable information on the spectral types and physical properties of galaxies, while using COSMOS templates we achieve a better determination of photometric redshifts. Therefore, it is possible to choose between a high-performance in photo-z and spectral type determination with COSMOS and physical information of the objects with BC03.

4.6 Probability Distribution Function (PDF) and Large-Scale Structure

Each redshift estimation returns a probability distribution function (PDF) derived directly from the χ^2 distribution, being defined as:

$$P(z) \propto \exp\left(-\frac{\chi^2_{(z)} - \chi^2_{min}}{2}\right). \tag{4.12}$$

The minimum and maximum redshifts around the photo-z solution, corresponding to the 1σ errors, are estimated from the equation

$$\chi^2_{(z)} = \chi^2_{min} + 1. \tag{4.13}$$

The sum of these PDFs results in the PDF of the redshift distribution of all galaxies in the survey and it is a powerful tool because it maintains the full redshift probability distribution (which can contain multiple redshift peaks or plateaus), rather than just the redshift of maximum likelihood and its (assumed to be Gaussian) error. The combined PDF retrieved from our determinations is shown in Fig. 4.17, giving the full redshift distribution expected for the S-PLUS sample as a function of limiting r-band magnitude.

This cumulative distribution function indicates that we have high-probability of finding objects in several discrete "spikes" in the regions of redshifts $z \sim 0.1$ and $z \sim 0.3$. We have

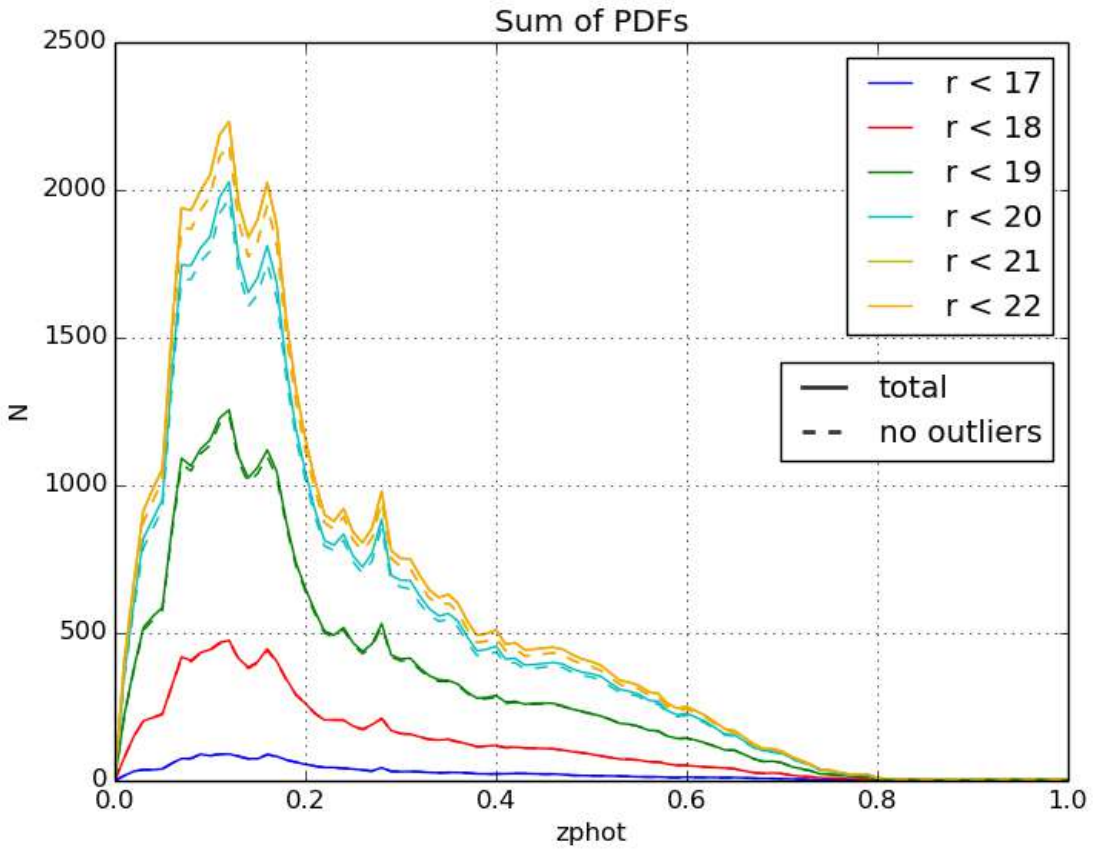

Figure 4.17: Probability Distribution Function of all galaxies in the survey from LePHARE determinations of photometric redshifts as a function of limiting r-band magnitude. Dashed lines show the results after rejecting catastrophic redshift outliers. Several "spikes" in the redshift distribution are seen at $z \sim 0.1$, $z \sim 0.15$ and $z \sim 0.3$, which could be related to the large-scale structure.

checked that the discrete spikes seen in the CDF are not an artifact due to catastrophic outliers in the photometric redshift determination. Also shown in Fig. 4.17 obtained after rejecting all outliers (dashed lines). The redshift spikes are clearly not caused by the outliers. Next, we will analyze the spatial distribution of the sample, to see whether the spikes seen in the CDF can be related to any specific sub-structures in the large-scale structure.

We can now plot the local large-scale structure to understand the distribution of galaxies, overdensities, identify clusters and so on. This distribution is shown in Figs. 4.18 and 4.19, for the objects residing between $-1°$ and $0°$ in declination and $0°$ and $+1°$, respectively.

From these figures, it is clear that we can recover, to some extent, the same large structures that are observed to much greater detail in the spectroscopic sample. We also

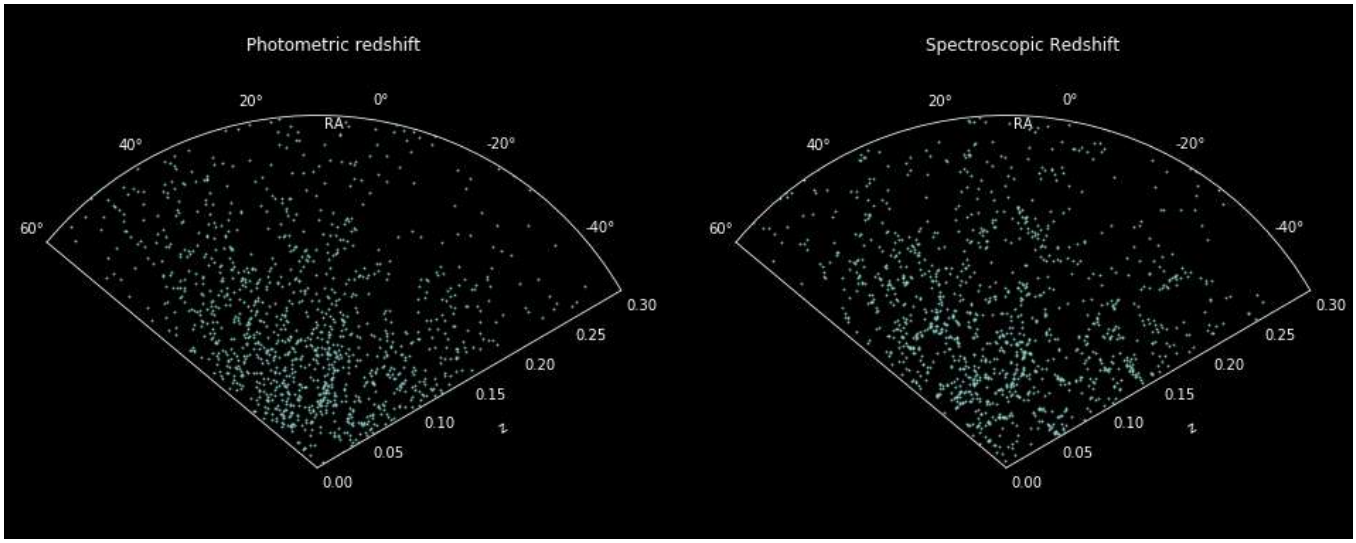

Figure 4.18: Large-scale structure recovered with spectroscopic and photometric redshifts for the region within $\delta > 0°$ and $\delta < +1°$.

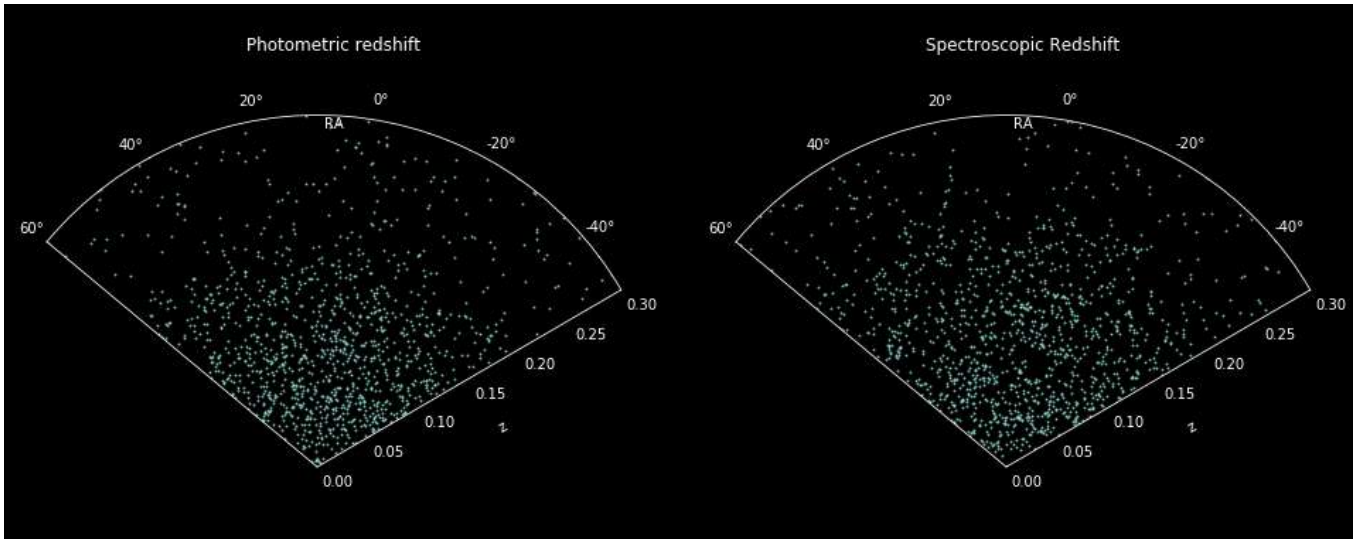

Figure 4.19: Large-scale structure recovered with spectroscopic and photometric redshifts for the region within $\delta > -1°$ and $\delta < 0°$.

confirm the wall-like structures predicted by the combined PDF when observing the $z \sim 0.1$ and $z \sim 0.3$ strips in the large-scale structure.

Fig. 4.20 shows the large scale structure coloured with the precision of our determinations. As expected, the lower the redshift, the more accurate are the photometric redshift determinations.

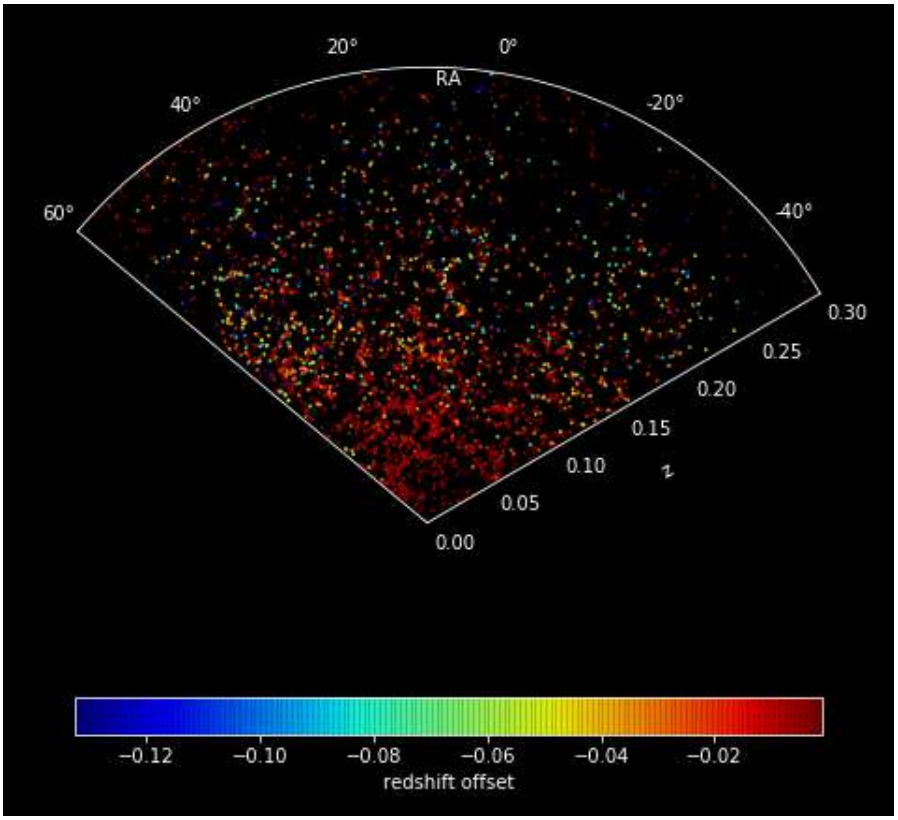

Figure 4.20: The offsets between spectroscopic and photometric redshifts in the large-scale structure.

4.6.1 Distribution of S0s

Given the general theme of this thesis, in the final part of this Chapter we will focus on the identification of candidate S0 galaxies in S-PLUS. With the accurate photometric redshifts and spectral types retrieved with LePhare, we identified all objects classified as S0 galaxies and show their distribution in the local universe as traced by the locations of all spectroscopically known objects in the same region (grey points).(Fig. 4.21).

These S0s were identified on the basis of the COSMOS SEDs. However, once separated in spectral types, we ran LePHARE again using BC03 templates to retrieve the physical properties of these sources, such as their stellar mass, age and SFR. The identified lenticular galaxies are highlighted over the large-scale structure in Fig. 4.21, where they are coloured according to the SFR ($M_{\odot}/yr$).

From this distribution, we can already make some very interesting qualitative conclusions. Those S0s that are clustered usually show lower levels of star-formation, while the more isolated ones tend to have higher rates. We can also see that S0s are more frequently found in clustered regions and are almost never isolated. This could indicate that these

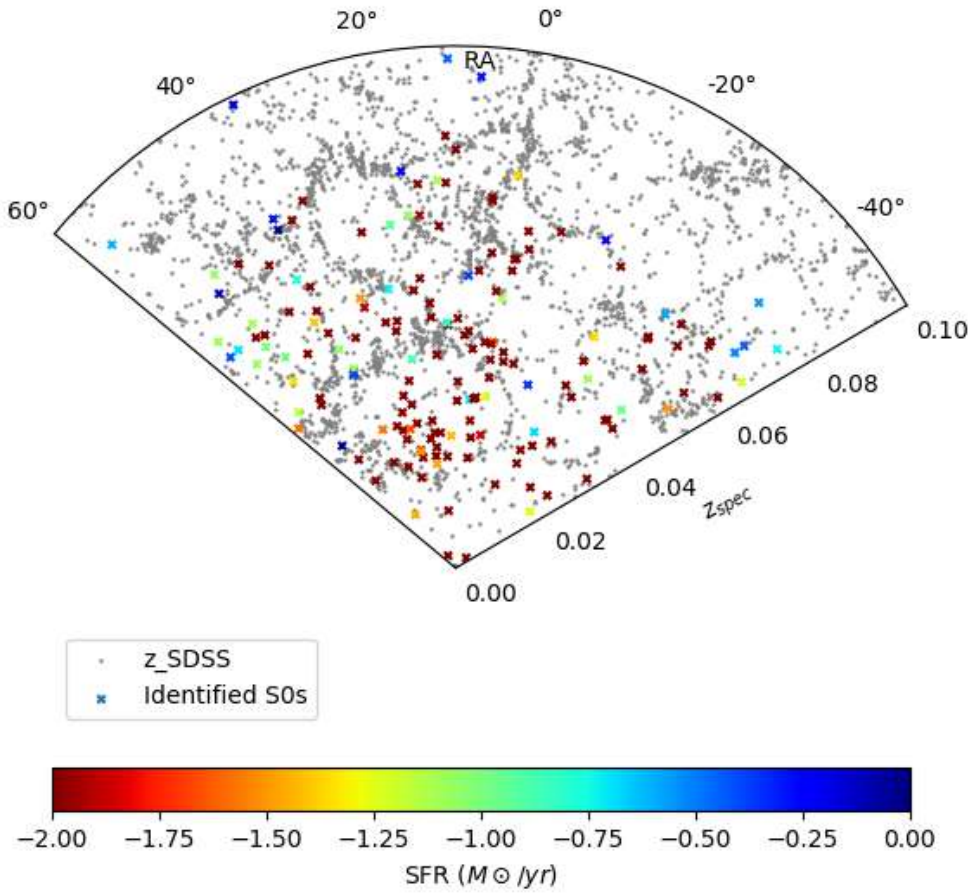

Figure 4.21: Distribution of S0 galaxies in the local universe. In this plot we show the large scale structure retrieved using spectroscopic redshifts in the back (gray) and those identified -via spectral type- S0 galaxies coloured by the specific star formation rate (SFR) obtained using BC03 theoretical templates.

S0s favour formation scenarios related to high-density environments.

In total, we identified 521 S0 galaxies among the 17500 studied, representing about 3% of the total number of galaxies, indicating that the S-PLUS survey will be able to deliver statistical samples of S0 galaxies as the survey expands. We consider the 3% found here a lower limit, given that our selection of S0 galaxies here is based strictly on those galaxies that were best fitted with the single S0 template present in the COSMOS template library. A more thorough comparison of the colours, morphologies and magnitudes of all objects may lead to a wider selection of objects that are best described by the S0 morphological class.

From these identified S0s, we selected a subsample of galaxies with SFR $> 10^{-1}$ yr^{-1} and with SFR $< 10^{-1}$ yr^{-1} to visualize their differences. In Figs. 4.22 and 4.23, we show

the SDSS images of these galaxies.

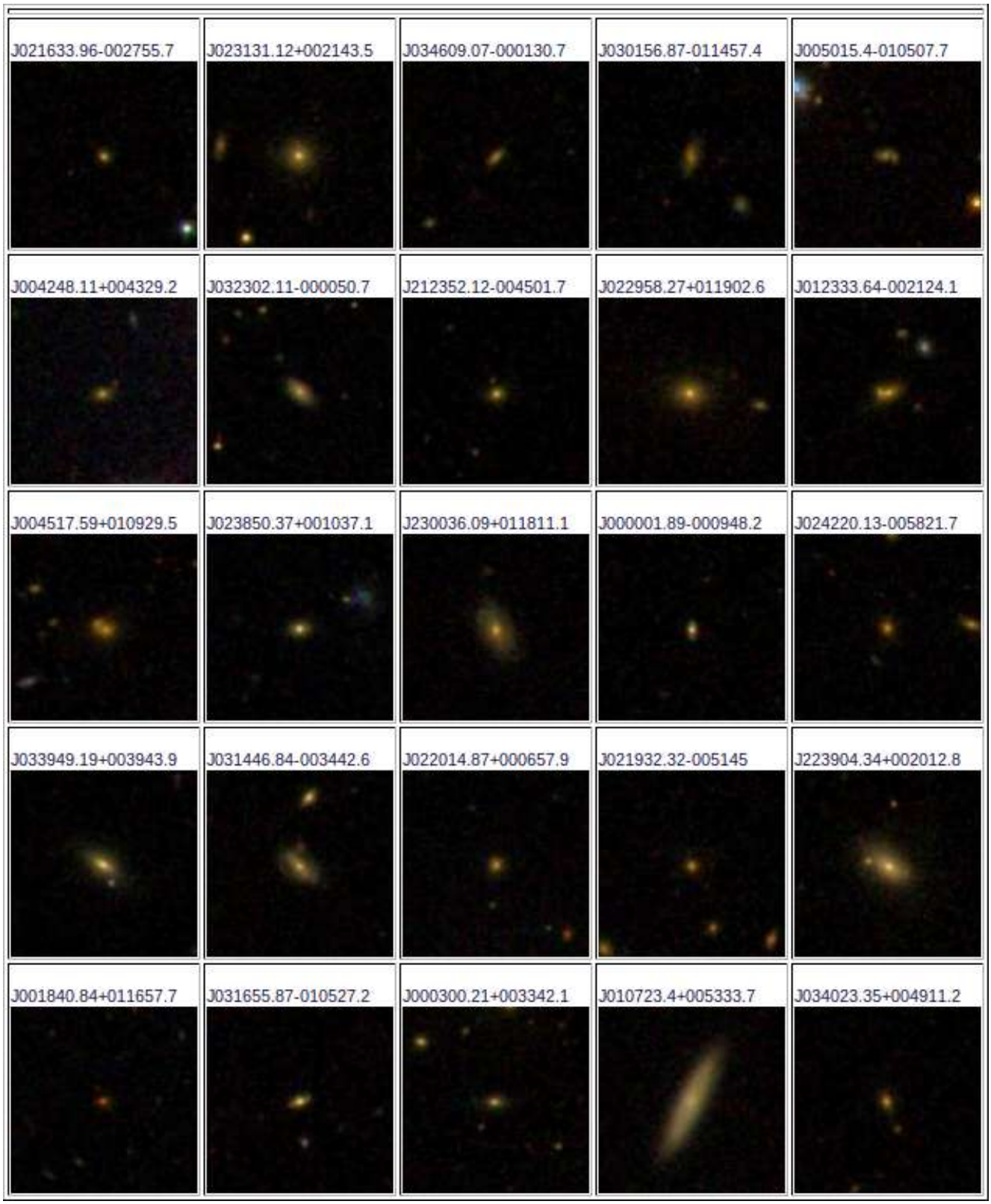

Figure 4.22: Candidate S0 galaxies identified with S-PLUS. Subsample of the candidates with star-formation rates higher than 10^{-1} yr^{-1}.

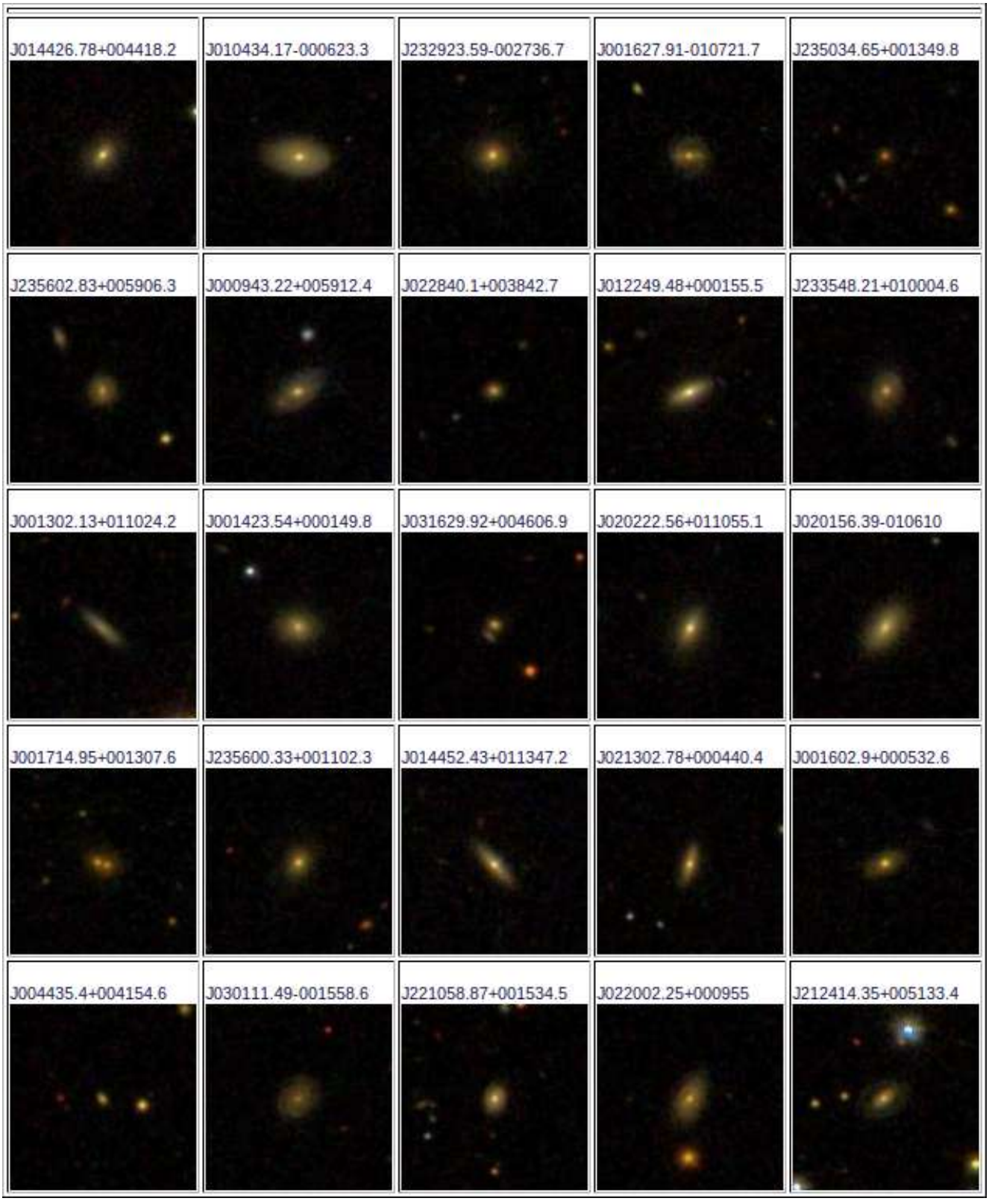

Figure 4.23: Candidate S0 galaxies identified with S-PLUS. Subsample of the candidates with star-formation rates lower than 10^{-1} yr^{-1}.

With this visual inspection of the galaxies with different SFR (see Figs. 4.22 and 4.23), we found that their morphologies are different. The ones with lower levels of SFR (Fig. 4.23) are qualitatively more similar to the morphological type of S0s, i.e. more disky and redder. On the other hand, the ones with higher SFR (Fig. 4.22) seem to include galaxies with spiral arms and that do not look like S0 galaxies. These galaxies can, however, be in process of fading and this explains their best-fit model to be of an S0. This is, nevertheless, in agreement with Fraser-McKelvie et al. (2018), that proposed that S0 galaxies are both dependent on mass and environment as drivers of their evolution.

4.7 Conclusions

For this work, we have used multi-wavelength data of the Southern Photometric Local Universe Survey to recover photometric redshifts, spectral types and physical properties of a sample of galaxies in the S-PLUS footprint. For 17500 galaxies with reliable spectroscopic redshifts and determinations of photometric redshifts from several methods, both template-fitting and deep learning, we have applied the template-fitting code LePHARE using the COSMOS and Bruzual and Charlot templates to fit the galaxies.

Evaluating the σ_{NMAD}, bias (μ) and outlier fraction (η) of our determinations, we conclude that our method is comparable with the Bayesian Photometric Redshift Estimator (BPZ), previously applied for the same sample of galaxies. Our method, however, has better determinations of spectral types and physical properties of the galaxies. The comparison with the deep learning techniques has shown that these data-driven methods are generally better than its template-fitting counterparts. However, they require a training sample and do not provide any physical property of the objects.

Using LePHARE, we achieve a precision of 1%, 2% and 3% in photo-z determinations for galaxies with $r < 17$, $r < 19$ and $r < 21.3$ mag. Moreover, using LePHARE, we found systematic offsets in the zero-points of $0.01 - 0.07$ in the different filters and fields of S-PLUS.

With these results, we recovered the cumulative distribution function of these galaxies and identified walls in the large-scale structure in the regions of $z \sim 0.1$ and $z \sim 0.3$, confirmed in the recovered large-scale structure.

Within all the objects studied, we have identified those best-fitted by the template

of lenticular galaxies and we have found their distribution across the local universe. It is important to reinforce that one template of lenticular galaxy may not representative of different formation scenarios, given that lenticulars formed in different ways may have different age and metallicity gradients.

We identified in the distribution of S0s that they mostly lie in clustered regions and are hardly isolated, indicating that we may be favouring formation scenarios in high-density environments using this specific template.

We visually inspected the images of two subsamples of galaxies with high and low SFR levels (see Figs. 4.23 and 4.22) and we found that their morphology is different, with the low SFR ones resembling S0-like galaxies, while the ones with higher rates show spiral arms and bluer components than it would be expected for S0s. We find that their morphologies are qualitatively different, with the low SFR ones resembling S0-like galaxies, while the ones with higher rates show spiral arms and bluer components and do not look like S0s. These spiral galaxies could, however, be in process of fading. This is in agreement with Fraser-McKelvie et al. (2018), that proposed that S0 galaxies are both dependent on mass and environment as drivers of their evolution.

We conclude this work with a great future ahead of us, now that we have tested and confirmed the accuracy and efficiency of our method, we will apply this to the whole sample of galaxies (and stars and quasars) of S-PLUS DR1 and DR2, and investigate the relation between S0 templates and morphology, in order to develop more templates for S0 galaxies.

Chapter 5

General Conclusions and Future Work

This master dissertation focused on studying in detail S0 galaxies in the local universe. Using three different roads, we studied: (1) an already formed isolated S0 galaxy, NGC 3115, using multi-wavelength data to recover its formation history and evolution; (2) a possible scenario to create S0 galaxies: the major merger NGC 1487, using VLT/MUSE data to understand the chemical composition and kinematics of the system; (3) the distribution of S0 galaxies in the local universe using S-PLUS data. We recover photometric redshifts and spectral types for thousands of galaxies in the nearby universe to identify the lenticular galaxies among them.

For the first part of this work, we focused on the closest lenticular galaxy to the Milky Way, NGC 3115. Using 11 images of this galaxy, going from the ultraviolet (FUV) to infrared (4.6 WISE) we performed multi-wavelength fitting with the code GALFITM to create the best-fitting model to this galaxy. This model is composed of three components: a bulge with a Sérsic profile with $n = 3.5$, a thick disc and a thin disc. This model was created imposing the results of the best model created for the three highest S/N images (g, r and i), since the parameters should not vary a lot from band-to-band after decomposing the galaxy into its components. We let only the magnitudes vary with 9 degrees of freedom for all components and the disc scale-length with 2 DoF (linear) for both the thick and thin discs.

The SED fitting of the components has shown that the bulge of this galaxy is the most massive component, as well as the bluest one. Comparing the SEDs obtained using AGN models and without them in CIGALE, we can actually measure the influence of the AGN emission in the SED of the bulge (and the galaxy as a whole). Firstly, focusing on the results of the bulge displayed in the first and sixth lines of Table 2.3, we see that the

difference in the SFR from the fitting with and without AGN emission is significantly large (around 10 solar masses a year). So, excluding the AGN emission, the colors observed in the bulge in the previous section would be less blue. Nonetheless, even excluding the AGN emission, we can see that the SFR of the bulge is still high and larger than the other components, showing that there may be a star formation event occurring in the center of the galaxy, together with the AGN activity. We also see that the mass of the galaxy is mainly in the bulge, where the super massive black hole lies. Going outwards to the thin disk, we see a strong decrease in the SFR, that grows again when reaching the thick disk, where the effect of minor mergers and accretion of companions would account for the larger rates of star formation.

Using the residuals of our model, we identified relics of spiral arms in this galaxy, before identified by Guérou et al. (2016) as well. Using an RGB image of the residuals, we see that these spiral arms are bluer than the discs surrounding them, indicating that they could be an attempt of the galaxy to reignite star formation. We also identified that the colour of these spiral arms are similar to the ones of the dwarf companion KK084 and this indicate that they may have been formed in the same episode. This will be further studied in the next months.

The residuals have also shown an end-on bar in the center of NGC 3115, that was confirmed using the simulations of our collaborator Victor DeBattista, where we compare the unsharp mask of NGC 3115 with two simulated galaxies containing the same components as NGC 3115, one with a bar and one without. The comparison clearly shows the same boxy bulge and flares in NGC 3115 center and in the galaxy with the bar, supporting the presence of this component in the lenticular galaxy.

Finally, we propose a scenario for the formation of NGC 3115 based on a initial gas-rich merger, followed by a sequence of accretions and AGN feedback, quenching the galaxy, until a recent encounter able of reigniting the star formation in the bulge and generating the spiral features observed.

The second part of this work was focused on the study of the major merger NGC 1487 to understand how and if these events can create lenticular galaxies. We use MUSE data of the system and perform spectral fitting using the fitting code FADO to understand the galaxies in a spaxel-by-spaxel manner.

Inhomogeneities in the metallicity gradients of the galaxies have been identified, spe-

cifically in the four bright regions APC1, APC2, APC3 and APC4 (see Fig. 3.4), in the sense that these have lower metallicities in their centers as compared to their outskirts. This suggests that the merger event induced infall of pristine gas into the center of the system. This inflow of fresh gas is most probably producing the high star formation rates in the same location. No sign of AGN activity has been detected - all the regions have been primarily ionized by star-formation.

The merging event seems to have caused the suppression of star formation in the northern region of the system and it has triggered high rates of star formation in APC3 and APC4, creating a ring-shaped center of star formation in the proximity of APC4.

The kinematic study has shown that there are flows happening in the galaxy, specifically, a rotational pattern was identified in the region of APC2 that will be further investigated with Fabry-Perot data in Torres-Flores et al. in prep.

The study of the age distribution of the system suggests that there are very young stellar populations in the center of this galaxy and in its tails, although the majority of the mass of the galaxy is accumulated in the old stellar populations present now in the outskirts of the galaxy.

This event seems likely to create S0-like galaxies in the scenario proposed by Tapia et al. (2017), where the major merger event would generate galaxies that would passively evolve to S0s. As discussed in the introduction, this type of process creates S0s with younger stellar populations in the center than in the outskirts of the galaxy, the same pattern observed in NGC 1487 from the maps of star formation and metallicity. We conclude that this galaxy could evolve to become an S0-like galaxy, if further left undisturbed for many Gyr.

Finally, the third part of this work focused on studying galaxies in the S-PLUS survey, retrieving photometric redshifts and spectral types of all galaxies and look for S0 galaxies.

Using the template fitting code LePHARE and the templates of COSMOS and Bruzual and Charlot 2003, we have retrieved photometric redshifts for 17500 galaxies. For this, we found a precision of 1%, 2% and 3% for galaxies with $r < 17$, $r < 19$ and $r < 22$ mag using the COSMOS templates and 2%, 3% and 5% using the BC03 templates. A great advantage of using the BC03 templates, however, is to retrieve physical properties of the galaxies from their best-fitting templates, such as age, stellar mass and SFR.

Using BC03, we were able to reconstruct the Red Sequence, Green Valley and Blue

Cloud, as well as find the distributions of SFR and divide the galaxies into starbursts and passive ones.

With the recovered photometric redshifts and their respective probability distribution functions, we have obtained the combined Probability Distribution Function of the survey and identified evidence for structures that represent walls and voids in the large-scale structure.

We have recreated maps of the local large-scale structure, confirming the walls and voids identified in the combined PDF, and compared our recovered structure with the structure obtained using the SDSS spectroscopic redshifts, showing the great potential of S-PLUS.

By using the spectral types recovered with LePHARE for all the galaxies, we selected the ones fitted with the lenticular template and studied their distribution in the local large-scale structure.

S0s mostly lie in clustered regions and are almost never isolated, indicating that formation scenarios that involve high-density environments may be favoured for objects selected using this specific template. With the visual inspection of images of two subsamples of the S0 candidates (see Figs. 4.23 and 4.22), one with galaxies with low SFR and one with higher SFR. We find that their morphologies are qualitatively different, with the low SFR ones resembling S0-like galaxies, while the ones with higher rates show spiral arms and bluer components and do not look like S0s. These spiral galaxies could, however, be in process of fading. This is in agreement with Fraser-McKelvie et al. (2018), that proposed that S0 galaxies are both dependent on mass and environment as drivers of their evolution.

We conclude this work listing a number of extremely interesting future steps that still remain open in our work:

1. What are the spiral-like features observed in NGC 3115 and how can the presence of these features influence the way we understand lenticular galaxies?

2. What is the true effect of the AGN in S0 galaxies formation and evolution? Is there really a double (or not centered) AGN in NGC 3115? How can this affect our understanding of this galaxy and lenticular galaxies in general?

3. Why interacting galaxies usually show inverted metallicity gradients? Is it gas from the outskirts of the galaxies or from the surrounding area that is responsible for this

inversion?

4. Is the rotating pattern in NGC 1487 really an attempt to recreate a disk? Run simulations and find in literature.

5. There is clearly a lack in templates of lenticular galaxies that are representative of different formation scenarios. How can we derive different templates? What are the main differences from scenario to scenario that can affect the templates?

6. With an SED template library representative of different formation scenarios of S0 galaxies, we will recover their real distribution in the universe with S-PLUS and perform statistical analysis with a great number of S0s.

7. Our method of estimation of photometric redshifts will be applied to all objects in the S-PLUS survey, resulting in Value Added Catalogs and a pipeline for the whole collaboration.

Bibliography

Aguero E. L., Paolantonio S., The Peculiar Galaxy NGC 1487, AJ, 1997, vol. 114, p. 102

Almeida I., Nemmen R., Wong K.-W., Wu Q., Irwin J. A., The multiwavelength spectrum of NGC 3115: hot accretion flow properties, MNRAS, 2018, vol. 475, p. 5398

Andredakis Y. C., Sanders R. H., Exponential bulges in late-type spirals : an improved description of the light distribution., MNRAS, 1994, vol. 267, p. 283

Arnold J. A., Romanowsky A. J., Brodie J. P., Chomiuk L., Spitler L. R., Strader J., Benson A. J., Forbes D. A., The Fossil Record of Two-phase Galaxy Assembly: Kinematics and Metallicities in the Nearest S0 Galaxy, ApJ, 2011, vol. 736, p. L26

Arnold J. A., Romanowsky A. J., Brodie J. P., Forbes D. A., Strader J., Spitler L. R., Foster C., Blom C., Kartha S. S., Pastorello N., Pota V., Usher C., Woodley K. A., The SLUGGS Survey: Wide-field Stellar Kinematics of Early-type Galaxies, ApJ, 2014, vol. 791, p. 80

Arnouts S., Cristiani S., Moscardini L., Matarrese S., Lucchin F., Fontana A., Giallongo E., Measuring and modelling the redshift evolution of clustering: the Hubble Deep Field North, MNRAS, 1999, vol. 310, p. 540

Arnouts S., Moscardini L., Vanzella E., Colombi S., Cristiani S., Fontana A., Giallongo E., Matarrese S., Saracco P., Measuring the redshift evolution of clustering: the Hubble Deep Field South, MNRAS, 2002, vol. 329, p. 355

Bacon R., Accardo M., Adjali L., Anwand H., Bauer S., Biswas I., Blaizot J., Boudon D., Brau-Nogue S., Brinchmann J., Caillier P., Capoani L., Carollo C. M., Contini T.,

Couderc P., , 2010 The MUSE second-generation VLT instrument. Society of Photo-Optical Instrumentation Engineers (SPIE) Conference Series p. 773508

Bacon R., Piqueras L., Conseil S., Richard J., Shepherd M., , 2016 MPDAF: MUSE Python Data Analysis Framework

Baldwin J. A., Phillips M. M., Terlevich R., Classification parameters for the emission-line spectra of extragalactic objects., PASP, 1981, vol. 93, p. 5

Barden M., Häußler B., Peng C. Y., McIntosh D. H., Guo Y., GALAPAGOS: from pixels to parameters, MNRAS, 2012, vol. 422, p. 449

Barro G., Faber S. M., Koo D. C., Dekel A., Fang J. J., Trump J. R., Pérez-González P. G., Pacifici C., Primack J. R., Somerville R. S., Yan H., Guo Y., Liu F., Ceverino D., Kocevski D. D., McGrath E., Structural and Star-forming Relations since $z \sim 3$: Connecting Compact Star-forming and Quiescent Galaxies, ApJ, 2017, vol. 840, p. 47

Bauer A., the American Astronomical Society, 2015 Explainer: seeing the universe through spectroscopic eyes

Bekki K., Unequal-Mass Galaxy Mergers and the Creation of Cluster S0 Galaxies, ApJ, 1998, vol. 502, p. L133

Bekki K., Couch W. J., Transformation from spirals into S0s with bulge growth in groups of galaxies, MNRAS, 2011, vol. 415, p. 1783

Belfiore F., Maiolino R., Maraston C., Emsellem E., Bershady M. A., Masters K. L., SDSS IV MaNGA - spatially resolved diagnostic diagrams: a proof that many galaxies are LIERs, MNRAS, 2016, vol. 461, p. 3111

Benítez N., Bayesian Photometric Redshift Estimation, ApJ, 2000, vol. 536, p. 571

Beraldo e Silva L., Debattista V. P., Khachaturyants T., Nidever D., Geometric properties of galactic discs with clumpy episodes, MNRAS, 2020, vol. 492, p. 4716

Bergvall N., Laurikainen E., Aalto S., Galaxy interactions - poor starburst triggers. III. A study of a complete sample of interacting galaxies, A&A, 2003, vol. 405, p. 31

Bernardi M., Shankar F., Hyde J. B., Mei S., Marulli F., Sheth R. K., Galaxy luminosities, stellar masses, sizes, velocity dispersions as a function of morphological type, MNRAS, 2010, vol. 404, p. 2087

Bianchi L., GALEX Team The Galaxy Evolution Explorer (GALEX): an All Sky Ultraviolet Survey, Mem. Soc. Astron. Italiana, 1999, vol. 70, p. 365

Borlaff A., Eliche-Moral M. C., Rodríguez-Pérez C., Querejeta M., Tapia T., Pérez-González P. G., Zamorano J., Gallego J., Beckman J., Formation of S0 galaxies through mergers. Antitruncated stellar discs resulting from major mergers, A&A, 2014, vol. 570, p. A103

Bournaud F., Jog C. J., Combes F., Galaxy mergers with various mass ratios: Properties of remnants, A&A, 2005, vol. 437, p. 69

Brocklehurst M., Calculations of level populations for the low levels of hydrogenic ions in gaseous nebulae., MNRAS, 1971, vol. 153, p. 471

Bruzual G., Charlot S., Stellar population synthesis at the resolution of 2003, MNRAS, 2003, vol. 344, p. 1000

Burgarella D., Buat V., Iglesias-Páramo J., Star formation and dust attenuation properties in galaxies from a statistical ultraviolet-to-far-infrared analysis, MNRAS, 2005, vol. 360, p. 1413

Calzetti D., Armus L., Bohlin R. C., Kinney A. L., Koornneef J., Storchi-Bergmann T., The Dust Content and Opacity of Actively Star-forming Galaxies, ApJ, 2000, vol. 533, p. 682

Cantiello M., Blakeslee J. P., Raimondo G., Chies-Santos A. L., Jennings Z. G., Norris M. A., Kuntschner H., Globular clusters of NGC3115 in the near-infrared, Astronomy Astrophysics, 2014, vol. 564, p. L3

Cappellari M., Copin Y., Adaptive spatial binning of integral-field spectroscopic data using Voronoi tessellations, MNRAS, 2003, vol. 342, p. 345

Cappellari M., Emsellem E., Parametric Recovery of Line-of-Sight Velocity Distributions from Absorption-Line Spectra of Galaxies via Penalized Likelihood, PASP, 2004, vol. 116, p. 138

Cappellari M., Emsellem E., Krajnović D., McDermid R. M., Serra P., Alatalo K., Blitz L., Bois M., The ATLAS^{3D} project - VII. A new look at the morphology of nearby galaxies: the kinematic morphology-density relation, MNRAS, 2011, vol. 416, p. 1680

Carollo C. M., The Centers of Early- to Intermediate-Type Spiral Galaxies: A Structural Analysis, ApJ, 1999, vol. 523, p. 566

Carollo C. M., Erroz-Ferrer S., den Brok M., Fagioli M., Onodera M., Tacchella S. M. C., The MAD View on the Outskirts of Disks. In Formation and Evolution of Galaxy Outskirts , vol. 321 of IAU Symposium, 2017, p. 163

Cenarro A. J., Moles M., Cristóbal-Hornillos D., Marín-Franch A., Ederoclite A., Varela J., López-Sanjuan C., Hernández-Monteagudo C., Angulo R. E., Vázquez Ramió H., et al. J-PLUS: The Javalambre Photometric Local Universe Survey, Astronomy Astrophysics, 2019, vol. 622, p. A176

Chien L.-H., Barnes J. E., Kewley L. J., Chambers K. C., Multiobject Spectroscopy of Young Star Clusters in NGC 4676, ApJ, 2007, vol. 660, p. L105

Christlein D., Zabludoff A. I., Can Early-Type Galaxies Evolve from the Fading of the Disks of Late-Type Galaxies?, ApJ, 2004, vol. 616, p. 192

Ciesla L., Elbaz D., Fensch J., The SFR-M$_*$ main sequence archetypal star-formation history and analytical models, A&A, 2017, vol. 608, p. A41

Ciesla L., Elbaz D., Schreiber C., Daddi E., Wang T., Identification of galaxies that experienced a recent major drop of star formation, A&A, 2018, vol. 615, p. A61

Ciotti L., Stellar systems following the R1/m luminosity law., A&A, 1991, vol. 249, p. 99

Clarke A. J., Debattista V. P., Nidever D. L., Loebman S. R., Simons R. C., Kassin S., Du M., Ness M., Fisher D. B., Quinn T. R., Wadsley J., Freeman K. C., Popescu C. C., The imprint of clump formation at high redshift - I. A disc α-abundance dichotomy, MNRAS, 2019, vol. 484, p. 3476

Clemens M. S., Panuzzo P., Rampazzo R., Vega O., Bressan A., Mid-infrared colour gradients and the colour-magnitude relation in Virgo early-type galaxies, MNRAS, 2011, vol. 412, p. 2063

Conroy C., van Dokkum P. G., Pixel color magnitude diagrams for semi-resolved stellar populations: the star-formation history of regions within the disk and bulge of M31, The Astrophysical Journal, 2016, vol. 827, p. 9

Cook B. A., Conroy C., Dokkum P. v., Speagle J. S., Measuring Star Formation Histories, Distances, and Metallicities with Pixel Color–Magnitude Diagrams. I. Model Definition and Mock Tests, The Astrophysical Journal, 2019, vol. 876, p. 78

Cortesi A., Merrifield M. R., Coccato L., Arnaboldi M., Gerhard O., Bamford S., Napolitano N. R., Romanowsky A. J., Douglas N. G., Kuijken K., Capaccioli M., Freeman K. C., Saha K., Chies-Santos A. L., Planetary Nebula Spectrograph survey of S0 galaxy kinematics - II. Clues to the origins of S0 galaxies, MNRAS, 2013, vol. 432, p. 1010

Cresci G., Mannucci F., Maiolino R., Marconi A., Gnerucci A., Magrini L., Gas accretion as the origin of chemical abundance gradients in distant galaxies, Nature, 2010, vol. 467, p. 811

Curtis H., The scale of the universe, National Research Council, 1921, vol. 2, p. 171

Dale D. A., Helou G., Magdis G. E., Armus L., Díaz-Santos T., Shi Y., A Two-parameter Model for the Infrared/Submillimeter/Radio Spectral Energy Distributions of Galaxies and Active Galactic Nuclei, ApJ, 2014, vol. 784, p. 83

Dawson K. S., Schlegel D. J., Ahn C. P., Anderson S. F., Aubourg É., Bailey S., Barkhouser R. H., Bautista J. E., Beifiori A. r., Berlind A. A., Bhardwaj V., Bizyaev D., Blake C. H., The Baryon Oscillation Spectroscopic Survey of SDSS-III, AJ, 2013, vol. 145, p. 10

Debattista V. P., Ness M., Gonzalez O. A., Freeman K., Zoccali M., Minniti D., Separation of stellar populations by an evolving bar: implications for the bulge of the Milky Way, MNRAS, 2017, vol. 469, p. 1587

den Brok M., Carollo C. M., Erroz-Ferrer S., Fagioli M., Brinchmann J., Emsellem E., Krajnović D., Marino R. A., Onodera M., Tacchella S., Weilbacher P. M., Woo J., The

MUSE Atlas of Disks (MAD): Ionized gas kinematic maps and an application to Diffuse Ionized Gas, arXiv e-prints, 2019, p. arXiv:1911.06070

Diaz J., Bekki K., Forbes D. A., Couch W. J., Drinkwater M. J., Deeley S., Formation of S0s via disc accretion around high-redshift compact ellipticals, MNRAS, 2018, vol. 477, p. 2030

Dolfi A., Forbes D. A., Couch W. J., Ferré-Mateu A., Bellstedt S., Bekki K., Diaz J., Romanowsky A. J., Brodie J. P., The assembly history of the nearest S0 galaxy NGC 3115 from its kinematics out to six half-light radii, Monthly Notices of the Royal Astronomical Society, 2020, vol. 495, p. 1321–1339

Dressler A., Galaxy morphology in rich clusters: implications for the formation and evolution of galaxies., ApJ, 1980, vol. 236, p. 351

Dressler A., Oemler Augustus J., Couch W. J., Smail I., Ellis R. S., Barger A., Butcher H., Poggianti B. M., Sharples R. M., Evolution since z = 0.5 of the Morphology-Density Relation for Clusters of Galaxies, ApJ, 1997, vol. 490, p. 577

Dupke R. A., Irwin J., Bonoli S., Cenarro J., Abramo R., Vilchez J., J-PAS: The Javalambre-Physics of the Accelerating Universe Astrophysical Survey. In American Astronomical Society Meeting Abstracts #233 , vol. 233 of American Astronomical Society Meeting Abstracts, 2019, p. 383.01

Durret F., Adami C., Laganá T. F., Environmental Effects on Galaxy Luminosity Functions in Clusters. In Tracing the Ancestry of Galaxies , vol. 277 of IAU Symposium, 2011, p. 9

Dutton A. A., Treu T., Brewer B. J., Marshall P. J., Auger M. W., Barnabé M., Koo D. C., Bolton A. S., Koopmans L. V. E., The SWELLS survey – V. A Salpeter stellar initial mass function in the bulges of massive spiral galaxies, Monthly Notices of the Royal Astronomical Society, 2012, vol. 428, p. 3183

Eliche-Moral M. C., Rodríguez-Pérez C., Borlaff A., Querejeta M., Tapia T., Formation of S0 galaxies through mergers. Morphological properties: tidal relics, lenses, ovals, and other inner components, A&A, 2018, vol. 617, p. A113

Erroz-Ferrer S., Carollo C. M., den Brok M., Onodera M., Brinchmann J., Marino R. A., Monreal-Ibero A., Schaye J., Woo J., Cibinel A., Debattista V. P., Inami H., Maseda M., Richard J., Tacchella S., Wisotzki L., The MUSE Atlas of Disks (MAD): resolving star formation rates and gas metallicities on <100 pc scales†, MNRAS, 2019, vol. 484, p. 5009

Finn R. A., Desai V., Rudnick G., Balogh M., Haynes M. P., Jablonka P., Koopmann R. A., Moustakas J., Peng C. Y., Poggianti B., Rines K., Zaritsky D., The Local Cluster Survey. I. Evidence of Outside-in Quenching in Dense Environments, ApJ, 2018, vol. 862, p. 149

Fitzpatrick E. L., Correcting for the Effects of Interstellar Extinction, PASP, 1999, vol. 111, p. 63

Fraser-McKelvie A., Aragón-Salamanca A., Merrifield M., Tabor M., Bernardi M., Drory N., Parikh T., Argudo-Fernández M., SDSS-IV MaNGA: the formation sequence of S0 galaxies, Monthly Notices of the Royal Astronomical Society, 2018, vol. 481, p. 5580

Fritz J., Franceschini A., Hatziminaoglou E., Revisiting the infrared spectra of active galactic nuclei with a new torus emission model, MNRAS, 2006, vol. 366, p. 767

Gallagher John S. I., Hunter D. A., Structure and Evolution of Irregular Galaxies, ARA&A, 1984, vol. 22, p. 37

Georgakakis A., Forbes D. A., Norris R. P., Cold gas and star formation in a merging galaxy sequence, MNRAS, 2000, vol. 318, p. 124

Gerhard O. E., Line-of-sight velocity profiles in spherical galaxies: breaking the degeneracy between anisotropy and mass., MNRAS, 1993, vol. 265, p. 213

Gomes J. M., Papaderos P., Fitting Analysis using Differential evolution Optimization (FADO):. Spectral population synthesis through genetic optimization under self-consistency boundary conditions, A&A, 2017, vol. 603, p. A63

Gonçalves T. S., Martin D. C., Menéndez-Delmestre K., Wyder T. K., Koekemoer A., Quenching Star Formation at Intermediate Redshifts: Downsizing of the Mass Flux Density in the Green Valley, ApJ, 2012, vol. 759, p. 67

Guérou A., Emsellem E., Krajnović D., McDermid R. M., Contini T., Weilbacher P. M., Exploring the mass assembly of the early-type disc galaxy NGC 3115 with MUSE, A&A, 2016, vol. 591, p. A143

Gunn J. E., Gott J. Richard I., On the Infall of Matter Into Clusters of Galaxies and Some Effects on Their Evolution, ApJ, 1972, vol. 176, p. 1

Hammer F., Flores H., Puech M., Yang Y. B., Athanassoula E., Rodrigues M., Delgado R., The Hubble sequence: just a vestige of merger events?, A&A, 2009, vol. 507, p. 1313

Häußler B., Bamford S. P., Vika M., Rojas A. L., Barden M., Kelvin L. S., Alpaslan M., Robotham A. S. G., Driver S. P., Baldry I. K., Brough S., Hopkins A. M., Liske J., Nichol R. C., Popescu C. C., Tuffs R. J., MegaMorph - multiwavelength measurement of galaxy structure: complete Sérsic profile information from modern surveys, MNRAS, 2013, vol. 430, p. 330

Hawkins E., Maddox S., Cole S., Lahav O., Madgwick D. S., Norberg P., Peacock J. A., Baldry I. K., Baugh C. M., Bland-Hawthorn J., et al. The 2dF Galaxy Redshift Survey: correlation functions, peculiar velocities and the matter density of the Universe, Monthly Notices of the Royal Astronomical Society, 2003, vol. 346, p. 78–96

Hubble E., «The Realm of the Nebulae», Ciel et Terre, 1936, vol. 53, p. 194

Ilbert O., Arnouts S., McCracken H. J., Bolzonella M., Bertin E., Le Fèvre O., Mellier Y., Zamorani G., Pellò R., Iovino A., Tresse L., Le Brun V., Bottini D., Garilli B., Maccagni D., Picat J. P., Accurate photometric redshifts for the CFHT legacy survey calibrated using the VIMOS VLT deep survey, A&A, 2006, vol. 457, p. 841

Izotov Y. I., Pilyugin L. S., Physics of galaxies with bursts of star formation.. In Main Astronomical Observatory - 50 years , 1994, p. 219

Jacob J. C., Katz D. S., Berriman G. B., Good J., Laity A. C., Deelman E., Kesselman C., Singh G., Su M.-H., Prince T. A., Williams R., , 2010 Montage: An Astronomical Image Mosaicking Toolkit

Jennings Z. G., Strader J., Romanowsky A. J., Brodie J. P., Arnold J. A., Lin D., Irwin J. A., Sivakoff G. R., Wong K.-W., THE SLUGGS SURVEY:HST/ACS MOSAIC IMA-

GING OF THE NGC 3115 GLOBULAR CLUSTER SYSTEM, The Astronomical Journal, 2014, vol. 148, p. 32

Johnston E. J., Aragón-Salamanca A., Merrifield M. R., The origin of S0s in clusters: evidence from the bulge and disc star formation histories, MNRAS, 2014, vol. 441, p. 333

Kauffmann G., Heckman T. M., Tremonti C., Brinchmann J., Charlot S., White S. D. M., Ridgway S. E., Brinkmann J., The host galaxies of active galactic nuclei, MNRAS, 2003, vol. 346, p. 1055

Kaviraj S., Kirkby L. A., Silk J., Sarzi M., The UV properties of E+A galaxies: constraints on feedback-driven quenching of star formation, MNRAS, 2007, vol. 382, p. 960

Kelvin L. S., Driver S. P., Robotham A. S. G., Hill D. T., Alpaslan M., Baldry I. K., Bamford S. P., Bland-Hawthorn J., Brough S., Graham A. W., Häussler B., Hopkins A. M., Galaxy And Mass Assembly (GAMA): Structural Investigation of Galaxies via Model Analysis, MNRAS, 2012, vol. 421, p. 1007

Kennicutt Robert C. J., Star Formation in Galaxies Along the Hubble Sequence, ARA&A, 1998, vol. 36, p. 189

Kewley L. J., Dopita M. A., Leitherer C., Davé R., Yuan T., Allen M., Groves B., Sutherland R., Theoretical Evolution of Optical Strong Lines across Cosmic Time, ApJ, 2013, vol. 774, p. 100

Kewley L. J., Dopita M. A., Sutherland R. S., Heisler C. A., Trevena J., Theoretical Modeling of Starburst Galaxies, ApJ, 2001, vol. 556, p. 121

Kewley L. J., Groves B., Kauffmann G., Heckman T., The host galaxies and classification of active galactic nuclei, MNRAS, 2006, vol. 372, p. 961

Kewley L. J., Rupke D., Jabran Zahid H., Geller M. J., Barton E. J., METALLICITY GRADIENTS AND GAS FLOWS IN GALAXY PAIRS, The Astrophysical Journal, 2010, vol. 721, p. L48–L52

Khachikian E. Y., Weedman D. W., An atlas of Seyfert galaxies., ApJ, 1974, vol. 192, p. 581

Kormendy J., Brightness distributions in compact and normal galaxies. I. Surface photometry of red compact galaxies., ApJ, 1977, vol. 214, p. 359

Kormendy J., Bender R., A Proposed Revision of the Hubble Sequence for Elliptical Galaxies, ApJ, 1996, vol. 464, p. L119

Kormendy J., Bender R., A Revised Parallel-sequence Morphological Classification of Galaxies: Structure and Formation of S0 and Spheroidal Galaxies, ApJS, 2012, vol. 198, p. 2

Kuntschner H., Ziegler B. L., Sharples R. M., Worthey G., Fricke K. J., VLT spectroscopy of NGC3115 globular clusters, Astronomy Astrophysics, 2002, vol. 395, p. 761

Lee H. J., Lee M. G., The Star Cluster System of the Merging Galaxy NGC 1487, Journal of Korean Astronomical Society, 2005, vol. 38, p. 345

Lee J. H., Oh S., Jeong H., Yi S. K., Kyeong J., Park B.-G., Pixel Color–Magnitude Diagram Analysis of the Brightest Cluster Galaxies in Dynamically Young and Old Clusters Abell 1139 and Abell 2589, The Astrophysical Journal, 2017, vol. 844, p. 81

Lee J. H., Pak M., Lee H.-R., Oh S., Color Dispersion as an Indicator of Stellar Population Complexity: Insights from the Pixel Color-Magnitude Diagrams of 32 Bright Galaxies in Abell 1139 and Abell 2589, The Astrophysical Journal, 2018, vol. 857, p. 102

Lisker T., Grebel E. K., Binggeli B., Virgo Cluster Early-Type Dwarf Galaxies with the Sloan Digital Sky Survey. Iv. The Color-Magnitude Relation, AJ, 2008, vol. 135, p. 380

Marino R. A., Rosales-Ortega F. F., Sánchez S. F., Gil de Paz A., Vílchez J., Miralles-Caballero D., Kehrig C., Pérez-Montero E., Stanishev V., Iglesias-Páramo J., et al. The O3N2 and N2 abundance indicators revisited: improved calibrations based on CALIFA andTe-based literature data, Astronomy Astrophysics, 2013, vol. 559, p. A114

McDonald I., Boyer M. L., van Loon J. T., Zijlstra A. A., Hora J. L., Babler B., Block M., Gordon K., Meade M., Meixner M., Misselt K., Robitaille T., Sewilo M., Shiao B., Whitney B., VizieR Online Data Catalog: Fundamental stellar parameters in 47 Tucanae (McDonald+, 2011), VizieR Online Data Catalog, 2011, p. J/ApJS/193/23

Mendes de Oliveira C., Ribeiro T., Schoenell W., Kanaan A., Overzier R. A., Molino A., Sampedro L., Coelho P., Barbosa C. E., Cortesi A., et al. The Southern Photometric Local Universe Survey (S-PLUS): improved SEDs, morphologies, and redshifts with 12 optical filters, Monthly Notices of the Royal Astronomical Society, 2019, vol. 489, p. 241

Miyazaki S., Komiyama Y., Sekiguchi M., Okamura S., Doi M., Furusawa H., Hamabe M., Imi K., Kimura M., Nakata F., et al. Subaru Prime Focus Camera - Suprime-Cam, Publications of the Astronomical Society of Japan, 2002, vol. 54, p. 833

Mo H. J., Mao S., White S. D. M., The formation of galactic discs, MNRAS, 1998, vol. 295, p. 319

Moffat A. F. J., A Theoretical Investigation of Focal Stellar Images in the Photographic Emulsion and Application to Photographic Photometry, A&A, 1969, vol. 3, p. 455

Molino A., Costa-Duarte M. V., Sampedro L., Herpich F. R., Sodré L. J., Mendes de Oliveira C., Schoenell W., Barbosa C. E., Queiroz C., Lima E. V. R., Azanha L., Muñoz-Elgueta N., Ribeiro T., Kanaan A., Assessing the photometric redshift precision of the S-PLUS survey: the Stripe-82 as a test-case, arXiv e-prints, 2019, p. arXiv:1907.06315

Nogueira-Cavalcante J. P., Gonçalves T. S., Menéndez-Delmestre K., Sheth K., Star formation quenching in green valley galaxies at $0.5 \leq z \leq 1.0$ and constraints with galaxy morphologies, Monthly Notices of the Royal Astronomical Society, 2018, vol. 473, p. 1346–1358

Noll S., Burgarella D., Giovannoli E., Buat V., Marcillac D., Muñoz-Mateos J. C., Analysis of galaxy spectral energy distributions from far-UV to far-IR with CIGALE: studying a SINGS test sample, A&A, 2009, vol. 507, p. 1793

Osterbrock D. E., Active galactic nuclei, Annals of the New York Academy of Sciences, 1989, vol. 571, p. 99

Osterbrock D. E., Ferland G. J., Astrophysics of gaseous nebulae and active galactic nuclei, 2006

Papaderos P., Gomes J. M., Vílchez J. M., Kehrig C., Lehnert M. D., Ziegler B., Sánchez S. F., Husemann B., Monreal-Ibero A., García-Benito R., Bland-Hawthorn J., Cortijo-

Ferrero C., Nebular emission and the Lyman continuum photon escape fraction in CALIFA early-type galaxies, A&A, 2013, vol. 555, p. L1

Park C., Choi Y.-Y., Morphology Segregation of Galaxies in Color-Color Gradient Space, ApJ, 2005, vol. 635, p. L29

Peng C. Y., Ho L. C., Impey C. D., Rix H.-W., Detailed Structural Decomposition of Galaxy Images, AJ, 2002, vol. 124, p. 266

Perez J., Michel-Dansac L., Tissera P. B., Chemical evolution during gas-rich galaxy interactions, MNRAS, 2011, vol. 417, p. 580

Pettini M., Pagel B. E. J., [OIII]/[NII] as an abundance indicator at high redshift, MNRAS, 2004, vol. 348, p. L59

Poci A., McDermid R. M., Zhu L., van de Ven G., Combining stellar populations with orbit-superposition dynamical modelling: the formation history of the lenticular galaxy NGC 3115, MNRAS, 2019a, vol. 487, p. 3776

Poci A., McDermid R. M., Zhu L., van de Ven G., Combining stellar populations with orbit-superposition dynamical modelling: the formation history of the lenticular galaxy NGC 3115, MNRAS, 2019b, vol. 487, p. 3776

Poggianti B. M., Bressan A., Franceschini A., Star Formation and Selective Dust Extinction in Luminous Starburst Galaxies, ApJ, 2001, vol. 550, p. 195

Polletta M., Tajer M., Maraschi L., Trinchieri G., Lonsdale C. J., Chiappetti L., Andreon S., Pierre M., Le Fèvre O., Zamorani G., Maccagni D., Spectral Energy Distributions of Hard X-Ray Selected Active Galactic Nuclei in the XMM-Newton Medium Deep Survey, ApJ, 2007, vol. 663, p. 81

Prevot M. L., Lequeux J., Maurice E., Prevot L., Rocca-Volmerange B., The typical interstellar extinction in the Small Magellanic Cloud., A&A, 1984, vol. 132, p. 389

Querejeta M., Eliche-Moral M., Tapia T., Borlaff A., van de Ven G., Lyubenova M., Martig M., Falcón-Barroso J., Méndez-Abreu J., Zamorano J., Gallego J., Creating S0s with Major Mergers: A 3D View, Galaxies, 2015, vol. 3, p. 202

Rupke D., Kewley L., Barnes J., , 2010 Redistribution of Metals in Interacting Galaxies. ASPCS p. 355

Saha K., Cortesi A., Forming Lenticular Galaxies via Violent Disk Instability, ApJ, 2018, vol. 862, p. L12

Salim S., Green Valley Galaxies, Serbian Astronomical Journal, 2014, vol. 189, p. 1

Salpeter E. E., , 2005 Introduction to IMF@50. p. 3

Salvato M., Ilbert O., Hoyle B., , 2018 The many flavours of photometric redshifts

Sánchez Almeida J., Elmegreen B. G., Muñoz-Tuñón C., Elmegreen D. M., Pérez-Montero E., Amorín R., Filho M. E., Ascasibar Y., Papaderos P., Vílchez J. M., Localized Starbursts in Dwarf Galaxies Produced by the Impact of Low-metallicity Cosmic Gas Clouds, ApJ, 2015, vol. 810, p. L15

Sánchez Almeida J., Morales-Luis A. B., Muñoz-Tuñón C., Elmegreen D. M., Elmegreen B. G., Méndez-Abreu J., Metallicity Inhomogeneities in Local Star-forming Galaxies as a Sign of Recent Metal-poor Gas Accretion, ApJ, 2014, vol. 783, p. 45

Schindler S., Diaferio A., Metal Enrichment Processes, Space Sci. Rev., 2008, vol. 134, p. 363

Schlafly E. F., Finkbeiner D. P., Measuring Reddening with Sloan Digital Sky Survey Stellar Spectra and Recalibrating SFD, ApJ, 2011, vol. 737, p. 103

Schlegel D. J., Finkbeiner D. P., Davis M., Maps of Dust Infrared Emission for Use in Estimation of Reddening and Cosmic Microwave Background Radiation Foregrounds, ApJ, 1998, vol. 500, p. 525

Schmidt M., The Rate of Star Formation. II. The Rate of Formation of Stars of Different Mass., ApJ, 1963, vol. 137, p. 758

Scoville N., Aussel H., Brusa M., Capak P., Carollo C. M., Elvis M., Giavalisco M., Guzzo L., Hasinger G., Impey C., Kneib J. P., LeFevre O., Lilly S. J., Mobasher B., Renzini A., The Cosmic Evolution Survey (COSMOS): Overview, ApJS, 2007, vol. 172, p. 1

Searle L., Evidence for Composition Gradients across the Disks of Spiral Galaxies, ApJ, 1971, vol. 168, p. 327

Seaton M. J., Extinction of NGC 7027., MNRAS, 1979, vol. 187, p. 785

Sérsic J. L., Photometry of southern galaxies. IX:NGC 1313, Boletin de la Asociacion Argentina de Astronomia La Plata Argentina, 1963, vol. 6, p. 99

Silva L., Danese L., Granato G. L., Bressan A., Franceschini A., Models of Galaxy Spectral Evolution from the UV to the Sub-Millimeter, 1998, vol. 146, p. 334

Simard L., Mendel J. T., Patton D. R., Ellison S. L., McConnachie A. W., A Catalog of Bulge+disk Decompositions and Updated Photometry for 1.12 Million Galaxies in the Sloan Digital Sky Survey, ApJS, 2011, vol. 196, p. 11

Skrutskie M. F., Cutri R. M., Stiening R., Weinberg M. D., Schneider S., Carpenter J. M., Beichman C., Capps R., Chester T., Elias J., Huchra J., Liebert J., Lonsdale C., Monet D. G., Price S., Seitzer P., Jarrett T., The Two Micron All Sky Survey (2MASS), AJ, 2006, vol. 131, p. 1163

Stasińska G., Cid Fernandes R., Mateus A., Sodré L., Asari N. V., Semi-empirical analysis of Sloan Digital Sky Survey galaxies - III. How to distinguish AGN hosts, MNRAS, 2006, vol. 371, p. 972

Stasińska G., Vale Asari N., Cid Fernandes R., Gomes J. M., Schlickmann M., Mateus A., Schoenell W., Sodré L. J., Seagal Collaboration Can retired galaxies mimic active galaxies? Clues from the Sloan Digital Sky Survey, MNRAS, 2008, vol. 391, p. L29

Strateva I., Ivezić Ž., Knapp G. R., Narayanan V. K., Strauss M. A., Gunn J. E., Lupton R. H., Schlegel D., Bahcall N. A., Brinkmann J., Brunner R. J., Budavári T., Csabai I., Color Separation of Galaxy Types in the Sloan Digital Sky Survey Imaging Data, AJ, 2001, vol. 122, p. 1861

Szalay A. S., The Sloan Digital Sky Survey., Comput. Sci. Eng, 1999, vol. 1, p. 54

Tapia T., Eliche-Moral M. C., Aceves H., Rodríguez-Pérez C., Borlaff A., Querejeta M., Formation of S0 galaxies through mergers. Evolution in the Tully-Fisher relation since $z \sim 1$, A&A, 2017, vol. 604, p. A105

Toomre A., On the gravitational stability of a disk of stars., ApJ, 1964, vol. 139, p. 1217

Torres-Flores S., Mendes de Oliveira C., Amram P., Alfaro-Cuello M., Carrasco E. R., de Mello D. F., Witnessing Gas Mixing in the Metal Distribution of the Hickson Compact Group HCG 31, ApJ, 2015, vol. 798, p. L24

Torres-Flores S., Scarano S., Mendes de Oliveira C., de Mello D. F., Amram P., Plana H., Star-forming regions and the metallicity gradients in the tidal tails: the case of NGC 92, MNRAS, 2014, vol. 438, p. 1894

Tully R. B., Fisher J. R., Reprint of 1977A&A....54..661T. A new method of determining distance to galaxies., A&A, 1977, vol. 500, p. 105

Usher C., Brodie J. P., Forbes D. A., Romanowsky A. J., Strader J., Pfeffer J., Bastian N., The SLUGGS survey: measuring globular cluster ages using both photometry and spectroscopy, MNRAS, 2019, vol. 490, p. 491

Valdes F., Gruendl R., DES Project, 2014 The DECam Community Pipeline. p. 379

van de Sande J., Kriek M., Franx M., Bezanson R., van Dokkum P. G., The relation between dynamical mass-to-light ratio and color for massive quiescent galaxies out to $z \sim 2$ and comparison with stellar population synthesis models, The Astrophysical Journal, 2015, vol. 799, p. 125

van den Bergh S., Lenticular Galaxies and their Environments, ApJ, 2009, vol. 702, p. 1502

Vazdekis A., Koleva M., Ricciardelli E., Röck B., Falcón-Barroso J., UV-extended E-MILES stellar population models: young components in massive early-type galaxies, Monthly Notices of the Royal Astronomical Society, 2016, vol. 463, p. 3409–3436

Vazdekis A., Sánchez-Blázquez P., Falcón-Barroso J., Cenarro A. J., Beasley M. A., Cardiel N., Gorgas J., Peletier R. F., Evolutionary stellar population synthesis with MILES - I. The base models and a new line index system, MNRAS, 2010, vol. 404, p. 1639

Veilleux S., Osterbrock D. E., Spectral Classification of Emission-Line Galaxies. In NASA Conference Publication , vol. 2466 of NASA Conference Publication, 1987, p. 737

Vika M., Bamford S. P., Häußler B., Rojas A. L., MegaMorph - multiwavelength measurement of galaxy structure: physically meaningful bulge-disc decomposition of galaxies near and far, MNRAS, 2014, vol. 444, p. 3603

Vika M., Bamford S. P., Häußler B., Rojas A. L., Borch A., Nichol R. C., MegaMorph - multiwavelength measurement of galaxy structure. Sérsic profile fits to galaxies near and far, MNRAS, 2013, vol. 435, p. 623

Vika M., Vulcani B., Bamford S. P., Häußler B., Rojas A. L., MegaMorph: classifying galaxy morphology using multi-wavelength Sérsic profile fits, A&A, 2015, vol. 577, p. A97

Vinicius-Lima E., Photometric redshifts for S-PLUS using machine learning techniques, Universidade de São Paulo, 2019, Master Dissertation

Vulcani B., Bamford S. P., Häußler B., Vika M., Rojas A., Agius N. K., Baldry I., Bauer A. E., Brown M. J. I., Driver S., Graham A. W., Kelvin L. S., Liske J., Loveday J., Popescu C. C., Robotham A. S. G., Tuffs R. J., Galaxy And Mass Assembly (GAMA): the wavelength-dependent sizes and profiles of galaxies revealed by MegaMorph, MNRAS, 2014, vol. 441, p. 1340

Werk J. K., Putman M. E., Meurer G. R., Santiago-Figueroa N., Metal Transport to the Gaseous Outskirts of Galaxies, ApJ, 2011, vol. 735, p. 71

White S. D. M., Frenk C. S., Galaxy Formation through Hierarchical Clustering, ApJ, 1991, vol. 379, p. 52

Wilman D. J., Oemler A. J., Mulchaey J. S., McGee S. L., Balogh M. L., Bower R. G., Morphological Composition of z ~0.4 Groups: The Site of S0 Formation, ApJ, 2009, vol. 692, p. 298

Wong K.-W., Irwin J. A., Yukita M., Million E. T., Mathews W. G., Bregman J. N., Resolving the Bondi Accretion Flow toward the Supermassive Black Hole of NGC 3115 with Chandra, ApJ, 2011, vol. 736, p. L23

Wright E. L., Eisenhardt P. R. M., Mainzer A. K., Ressler M. E., Cutri R. M., Jarrett T., Kirkpatrick J. D., Padgett D., McMillan R. S., Skrutskie M., et al. The wide-field

infrared survey explorer (WISE): mission description and initial on-orbit performance, The Astronomical Journal, 2010, vol. 140, p. 1868–1881

Wyder T. K., Martin D. C., Schiminovich D., Seibert M., Budavári T., Treyer M. A., Barlow T. A., Forster K., Friedman P. G., Morrissey P., Neff S. G., Small T., The UV-Optical Galaxy Color-Magnitude Diagram. I. Basic Properties, ApJS, 2007, vol. 173, p. 293

Yıldız M. K., Peletier R. F., Duc P. A., Serra P., Cold gas and dust: Hunting spiral-like structures in early-type galaxies, A&A, 2020, vol. 636, p. A8

Appendix

Appendix A

The Model of NGC 3115

A.1 Degrees of freedom

The degrees of freedom (previously defined in Section 2.2.1 and represented by m_i, hereafter DoF) of GALFITM dictate how each parameter will vary within the wavelengths. Knowing that each parameter can vary with a different degree of freedom, going from fixed (DoF = 0) to completely free (DoF = number of images), and the more components a galaxy is fitted with, the more free parameters we introduce to this fitting (for example, axis ratio of the bulge, of the thick disc and thin disc are three different parameters that can have different DoF). Thus, we need to find the best combination of degrees of freedom that each parameter varies with to maximize the fit performance. To do so, we compared using solely visual inspection with the efficiency of finding the best combination using the Bayesian Information Criteria (BIC) and the Akaike Information Criteria (AIC).

For the BIC and AIC analysis, a set of 32 thousand models was created using different combinations of degrees of freedom for the parameters. The best model found using the BIC and AIC analysis consists of three components: a bulge, a thick disc and a thin disc and it has the following degrees of freedom:

- Sérsic index varying with 4 DoF.
- Effective Radius varying with 3 DoF.
- Disc scale-length varying with 3 DoF.
- Position Angle varying with 1 DoF for all components.
- Axis Ratio varying with 1 DoF for all components.

As explained in Section 2.4, we have modeled NGC 3115 with two different approaches using GALFITM. The first one is described in this Appendix, while the second is presented in Section 2.2.1. To model a galaxy with multi-wavelength data, we need to define the best structural parameters to start the fit, i.e. the number of components and with how many degrees of freedom each parameters will vary. However, how can we know which combination of degrees of freedom of the parameters maximizes the fit performance?

The proposed method to find the best number of degrees of freedom for each parameter of these galaxies and its components is iterative. We created thousands of models, each one with a different combination of degrees of freedom of the parameters to see which one of them showed better agreement with the input images, i.e. the one with the better residuals.

To find the morphology of galaxies, we used another iterative model. First, we created models with only one component. The results were used as initial conditions for a model with two components, and this was done subsequently until the best model was achieved.

For the analysis of the images and residuals, we used the Bayesian Information Criteria (BIC) and the Akaike Information Criteria (AIC), both described below.

A.1.1 BIC

The Bayesian Information Criteria is defined as the statistics that maximize the probability of identifying the "true" model among all of them. The value of the BIC criteria for a given model is described by:

$$BIC = \chi^2 + k\,ln(n), \tag{A.1}$$

with k being the number of degrees of freedom, and n the number of pixels of the image. The model with the lowest BIC is considered the best one.

A.1.2 AIC

The Akaike Information Criteria assumes that a "real" model that describe the data exists, but is unknown. The intention of the method is to find the model that minimize the Kullback-Leibler (K-L) divergence. The value of K-L for a model f with parameters θ, compared to the "true" model is represented by g and defined as:

$$I(g,\, f\theta) \,=\, \int g(y)\, ln\left(\frac{g(y)}{f(y)|\theta}\right) dy. \tag{A.2}$$

This divergence is related to the information that we lose when using an approximated model and not the real one.

AIC is then defined by:

$$AIC \,=\, 2k \,+\, \chi^2 \tag{A.3}$$

And in the same way as BIC, the model with the lowest value of AIC is considered the best.

A.1.3 Residual/Input

The image "Residual/Input" servs as a *delta (*Δ*)* function to analyse the results. We can describe this statistics as:

$$\Delta = \frac{I \,-\, M}{I}, \tag{A.4}$$

where I is the input and M is the model.

Therefore, if:

- $\Delta = 0$, then $I = M$ and the fit is exactly as the expected.
- $\Delta \,>\, 1$, then $M \,<\, 0$, which means that the model is underfitting the input.
- $\Delta \,<\, 1$, then $M \,>\, 1$, and that means that the model is overfitting the input.

This analysis is done for each one of the pixels in the image that are then averaged to achieve the final result for the whole image.

This result will tell us how good is our model, given that only BIC and AIC are not enough to analyse the results, because although they provide a good balance between the goodness of the χ^2 with a great number of degrees of freedom, it may happen that the best result has too much freedom and does not reflect real physical conditions of the galaxy.

In the same iterative way, when we add more components, the statistic methods described above are used to define the best combination for each component.

Figs. A.1 and A.2 show the distribution of the BIC and AIC values found for all of our models, already using three component: a bulge, a thick and a thin disc.

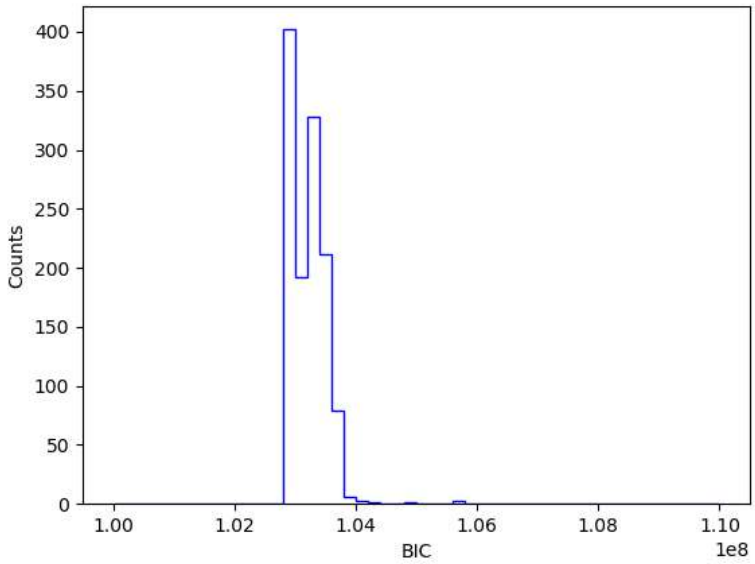

Figure A.1: Distribution of BIC for every model generated using a different combination of degrees of freedom for each parameter of the components that define NGC 3115.

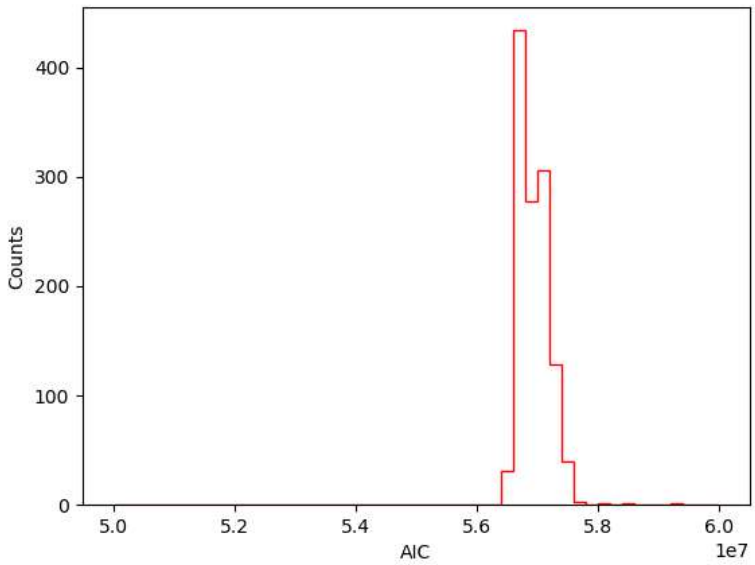

Figure A.2: Distribution of AIC for every model generated using a different combination of degrees of freedom for each parameter of the components that define NGC 3115.

In Fig. A.3 we show the variation of BIC in relation to AIC, and is from this relation that we retrieve the model the minimizes both statistics simultaneously.

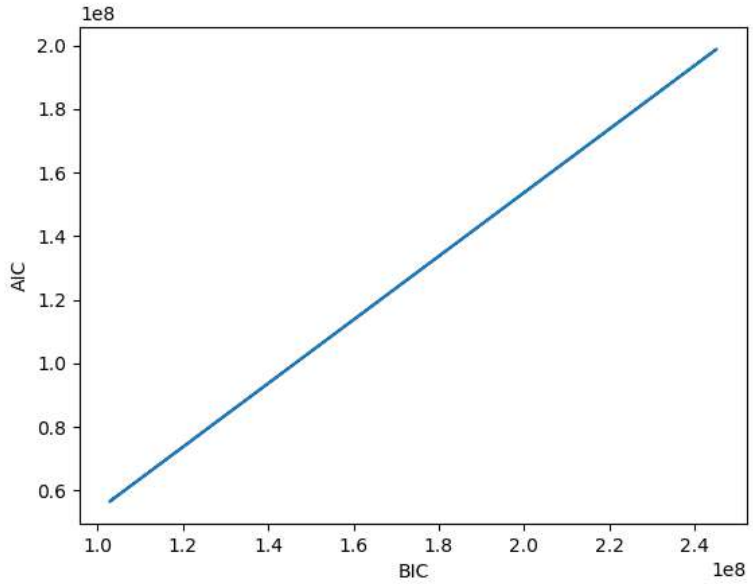

Figure A.3: Variation of BIC and AIC for every model created using different combinations of degrees of freedom for the parameters. This is the result for the model with three components: a bulge, thick and thin discs.

The best model found using the BIC and AIC analysis consists of three components: a bulge, a thick disc and a thin disc and has the following degrees of freedom:

- Sérsic index varying with 4 DoF.
- Effective Radius varying with 3 DoF.
- Disc scale-length varying with 3 DoF.
- Position Angle varying with 1 DoF for all components.
- Axis Ratio varying with 1 DoF for all components.

The best fitting model that minimizes BIC and AIC and varies with the previously shown DoF is shown in Fig. A.4.

Fig. A.5 is the result of the "Residual/Input" analysis for the model shown in Fig. A.4.

Averaging the retrieved values of "Residual/Input" analysis for the model shown in Fig. A.4, using each pixels in all bands, we find a "Residual/Input" mean value of 1.3 [1]. This

[1] We do not use the FUV and NUV bands in this average, because of their relatively low quality.

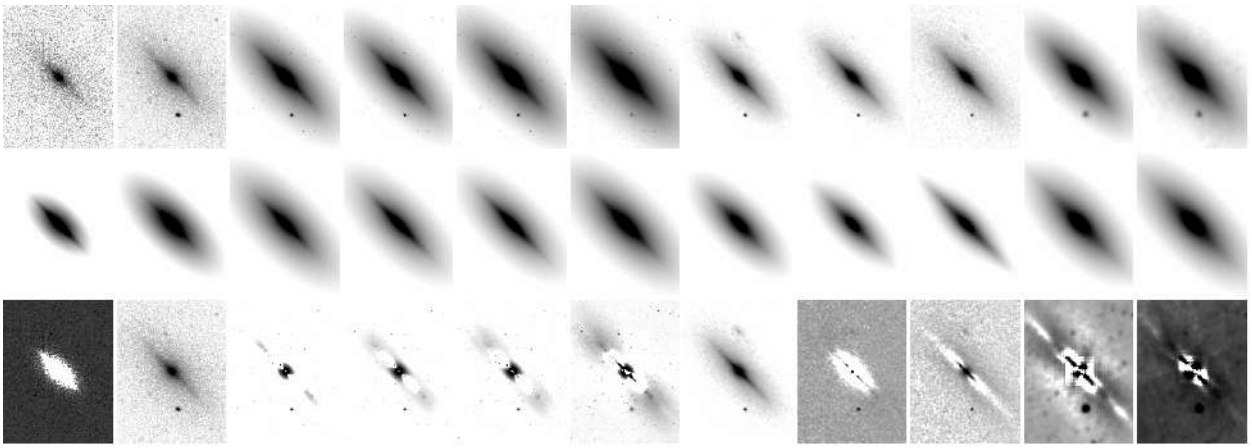

Figure A.4: Model created for the galaxy NGC 3115 with three components: a bulge, thick and thin disc. This is the best mdel found for this galaxy using our iterative approach, and the degrees of freedom of the parameters can vary: (1) Sérsic index varying with 4 DoF, (2) Effective Radius varying with 3 DoF, (3) Disc scale-length varying with 3 DoF, (4)Position Angle varying with 1 DoF for all components, (5) Axis Ratio varying with 1 DoF for all components. In this figure, the first line represents the input images, the second stand for the model and the third is the residual, while each column stand for different wavlengths.

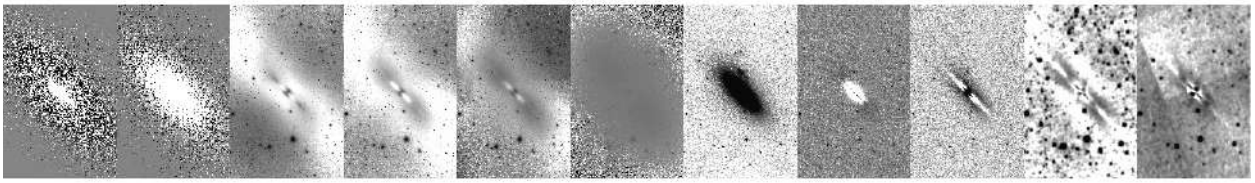

Figure A.5: Result of the analysis "Residual/Input", in which the residual of the model is divided by the input image in each wavelength. Each pixel of this image reveals if there was overfitting, underfitting or if the fit was as expected. The average value of these images evaluates the goodness of the fit. The closer to zero, the best.

shows that, in average, this is not a good fit, and there are sub-structures in the galaxy that we are not being able to fit using this combination of components and DoF.

Also, we can see from the model shown in Fig. A.4 that some bands are not even being fitted when defining the degrees of freedom as we did in this iterative manner. Using these models, we cannot understand the areas of influence of each component and neither their colours, so we decided to follow a more conservative method and evaluate the goodness of the models using only visual inspection, as described in Chapter 2. These models were, however, important for us to confirm that the galaxy is best fitted with 3 components: a bulge, a thick disc and a thin disc.

However, this best model was found to be worse than the one created using a more conservative approach, i.e. fitting the bands with higher S/N (g,r,i) together, before adding the other bands, to find the best parameters that describe this galaxy, and then forcing these parameters into all bands.

Appendix B

GALFIT versus GALFITM

In order to compare the efficiency of GALFITM and GALFIT, i.e. the difference between performing multi-band fitting and the fit of each image individually, we show in Fig. B.1 the variation of the effective radius, Sérsic index and disc scale-length for a single Sérsic model and bulge-disc decomposition of NGC 3115 using the two methods.

From these plots we can see that the fit with GALFITM has a more smooth and robust variation when compared to the individual fit with GALFIT. This is expected when imposing the form of variation of parameters across bands, as we did for the Subaru data, but it is important to reinforce that this is not always true. When we use broad bands, it is reasonable to think that the parameters vary smoothly among neighboring bands, with narrow bands, however, we could have an emission line inside the band, in which case there may be a bump and the superposition would not be possible.

It is worth noticing that GALFIT does not have as many points as GALFITM in these distributions. This is due to the fact that some bands are so faint, for example FUV and NUV, that they are impossible to fit individually, while GALFITM makes it possible by adding other bands and forcing them all to vary together. Moreover, these plots were made only for the single Sérsic and bulge-disc models, because the model with more components was only able to fit in 4 bands out of the eleven with GALFIT, due to the lack of resolution of the others.

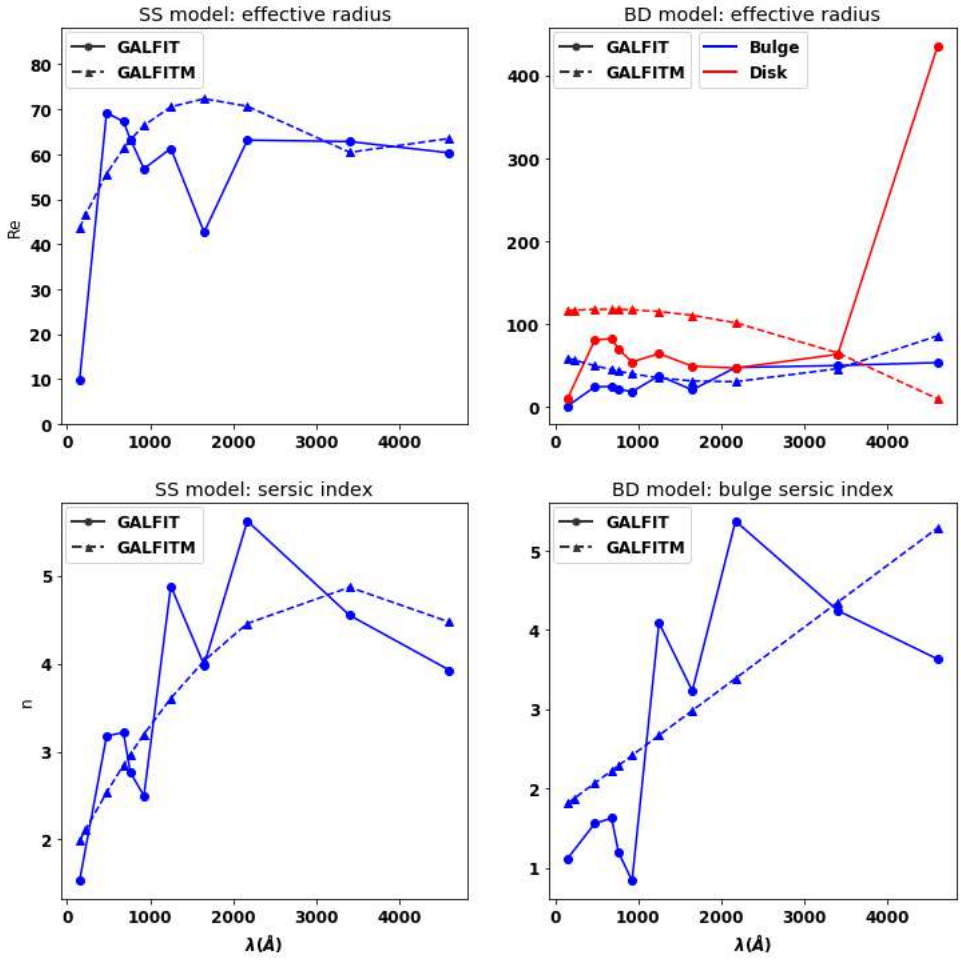

Figure B.1: Panels show the difference between GALFIT (filled) and GALFITM (dashed) for: *Upper left*, effective radius of single sersic model. *Lower left*, sersic index of single sersic model. *Upper right*, effective radius of bulge in blue and disc-scale length in red for the bulge-disc decomposition of NGC 3115. *Lower right*, sersic index of the bulge for the bulge-disc decomposition.